Statistics of Force Networks in Granular Media

J.H. Snoeijer

Statistics of Force Networks
in Granular Media

J. H. Snoeijer

Statistics of Force Networks in Granular Media

J. H. Snoeijer

Statistics of Force Networks
in Granular Media

PROEFSCHRIFT

DOOR

Jacobus Hendrikus Snoeijer

GEBOREN TE KAMPEN IN 1975

Contents

Physics of static granular media

1.1 Introduction

Granular media are systems consisting of a large number of interacting macroscopic particles. This definition embraces many systems in nature ranging from a pile of sand or bricks, to the icy rocks in the rings of Saturn. Even though the interactions between two individual particles can be relatively simple, the *collective behavior* of these particles is surprisingly rich and in most cases it is still poorly understood [1, 2, 3, 4]. The reason for this is the lack of a proper statistical description for these many body systems. In particular, one can not rely on thermodynamics since typical energies for granular dynamics are orders of magnitude larger than $k_B T$. In fact, the very definition of granular matter is that the particles are so large that thermal fluctuations are irrelevant; in practice this requires grains to be larger than roughly 10 microns (for a detailed classification see [5]).

In this introductory chapter we would like to give the reader a feel for the fascinating behavior of granular materials by highlighting some of the many remarkable experiments, and by addressing some basic theoretical aspects. Let us start the discussion with an experiment of grains flowing down a granular heap, very much like avalanches on a sand dune. The three images shown in Fig. 1.1 are side views of such a 'surface flow' between two glass plates, where particles are constantly inserted from the left side (not in the picture) [6]. The three photographs correspond to

the same experiment, but with different exposure time of the camera. On the time scale of a second, there is only a thin flowing layer at the top, while the rest of the pile appears to be immobile (Fig. 1.1a). However, the images obtained with longer exposures clearly show that the particle motion extends to much larger depths (Figs. 1.1bc); in fact there is a well-defined velocity profile even in the creeping part far below the free surface. There is thus an intricate interplay between 'static' and flowing parts of the material, of which there is no detailed understanding.

(a)   1 sec   (b)   1 min   (c)   1 hour
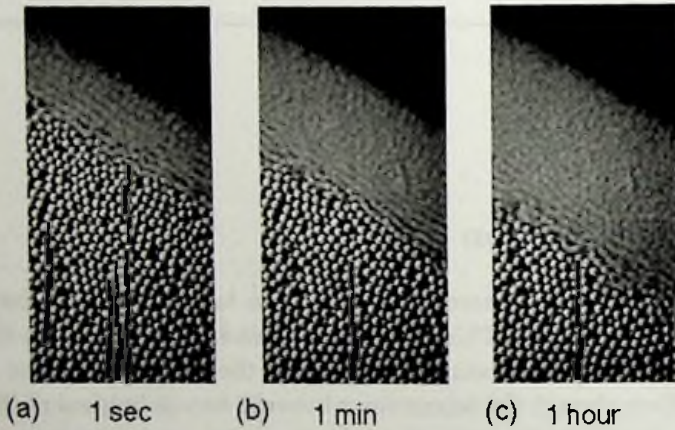
Figure 1.1: A steady surface flow on a pile of 1 mm alumina spheres. There is no well-defined interface separating static and flowing parts; on long time scales there is particle motion at arbitrary depth. Figure taken from Komatsu *et al.* [6].

In this thesis we focus on the behavior of *static* granular materials, for which particles are packed into one of the many possible metastable configurations. In particular we are interested in the forces between the particles: Fig. 1.2 is taken from an experiment with photoelastic beads, revealing that these forces organize themselves into tenuous *force networks*. These are complicated spatial structures emerging on length scales of several particle diameters. The central topic of this thesis is to theoretically investigate the physics of these force networks and to characterize their statistics.

Force networks such as shown in Fig. 1.2 are responsable for many surprising static and dynamic properties of dense granular media; in the

remainder of this chapter we discuss some further experimental examples to illustrate this. Particular attention will be paid to quantitative force measurements using carbon paper at the boundary of a container filled with grains. These experiments have provided a benchmark for the statistical analysis of forces in granular media and will play an important role throughout this thesis. After that we elaborate on theoretical aspects of dense granular matter, and we will formulate a number of general questions, some of which will be addressed in this thesis. But before we come to the intricate many body physics, we first address the interaction between individual particles.
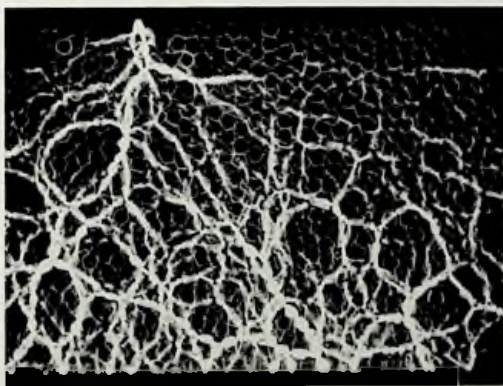
Figure 1.2: A two dimensional packing of photoelelastic particles, viewed between crossed polarizers. Photoelastic materials under anisotropic stress have the property to rotate the polarization of the light passing through them. So the bright lines are regions of large (anisotropic) forces, which together constitute a complicated force network. Courtesy of R. P. Behringer.

1.2 Particle interactions

In this study we restrict ourselves to electrically neutral, non-magnetic particles in vacuum or air. This implies that there are no forces between particles unless they are in contact. The grains interact with the surroundings via boundaries, and of course there is gravity. When two particles are in contact, there will be a normal force F_N plus a tangential *friction* force F_T. For 'dry' granular matter, normal forces are purely repulsive.

Here we encounter a first problem: Coulomb's law of friction[1] states that $|F_T| < \mu F_N$, where μ is the coefficient of friction. So, even if all particle positions and normal forces are known, the friction forces are undetermined; they depend on the detailed history of the microscopic contacts between particles [8]. On the scale of the grain size, friction will thus be a source of fluctuations and disorder (see Sec. 1.4.1). However, it will turn out that there are still large nontrivial force fluctuations without tangential forces. We therefore consider frictionless particles to be a good starting point for the study of force networks.

Finally, let us mention that the interactions between grains are *dissipative*. When two particles collide or slide along each other (in the presence of friction), energy will be conveyed to microscopic degrees of freedom that do not couple to the granular dynamics. So unless there is an external driving force, all granular matter will end up in one of the many possible static configurations. Once we have a static packing the dissipation is not relevant anymore, so it will not play a role here.

1.3 Experiments on force networks

1.3.1 Statics and slow flow

The idea of using photoelastic particles to visualize forces inside granular media originates from the field of soil mechanics in the 1960's [9]. This technique further evolved in the 1990's, when physicists became interested in the micromechanical structure of granular assemblies. One of the main questions is how the 'mesoscopic' force networks such as shown in Fig. 1.2 affect the properties of (quasi-)static granular media. There is a beautiful experiment by Vanel *et al.* [10] that reveals the complexity of the system. Two conical sandpiles were created according to different deposition procedures: the first pile was constructed by dropping grains from a localized source (Fig. 1.3, upper panel), whereas the second pile was formed through a homogeneous 'rain' of particles (Fig. 1.3, lower panel). Surprisingly, the pressure profile under the first pile has a dip at the center $r/R = 0$ where the height is maximal; for the second pile the pressure maximum lies in the middle. It thus appears that the history of construction has been

---

[1]This empirical law dates back to scientists like Leonardo da Vinci, Leonhard Euler and Charles Augustin de Coulomb (e.g. see [5]). Nowadays, the microscopic origin of friction is still intensively studied [7].
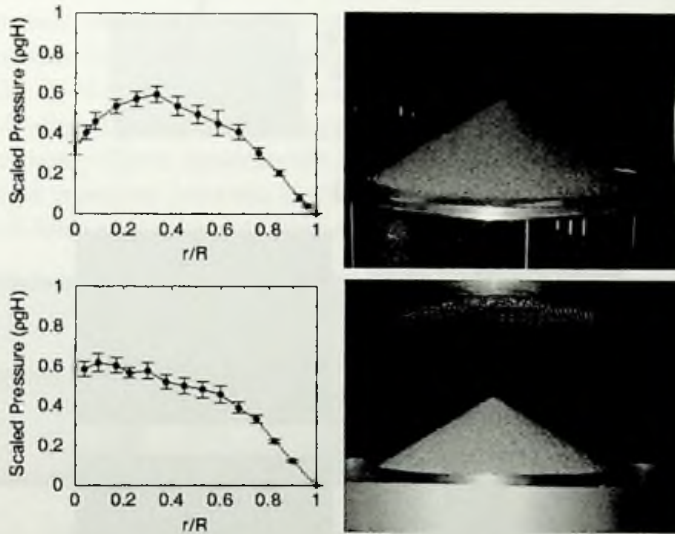
Figure 1.3: Two conical piles that are created from *(i)* a localized source, and *(ii)* a homogeneous 'rain' of particles, display a very different pressure profile underneath. Figure taken from Vanel *et al.* [10].

encoded into the force network, leading to different macroscopic stresses within these apparently equivalent sandpiles.

This history dependence is also observed in sheared granular systems. Fig. 1.4 shows the result of applying a small shear deformation to a packing of photoelastic particles [11]. Although this deformation hardly affected the texture of the packing, the force network has clearly become very anisotropic: the large forces are oriented at an angle of roughly 45°, which coincides with the principle axis of compression. In the same set of experiments, it was demonstrated that such microscopically encoded anisotropies indeed bias the response of the static material to an external load [11].

Furthermore, there is clear experimental evidence that packing effects are important for slow granular flows. Although granular matter has to expand in order to flow,[2] the particles remain densely packed at low shear

---

[2]This effect is called the principle of Reynolds's dilatancy [12].
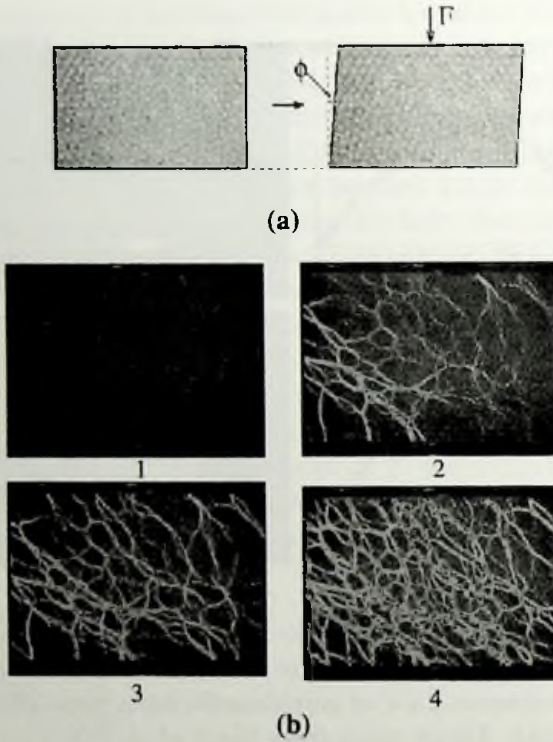
Figure 1.4: *(a)* Applying a shear deformation to a packing of photoelastic particles, by deforming a rectangular box with an angle ϕ. *(b)* The response of the force network for increasing ϕ; the force network aligns along the principle axis of compression. Figure taken from Geng *et al.* [11].

rates; think for example of the slowly creeping part below the free surface of an avalanche (Fig. 1.1). In granular flows, the velocity gradients tend to localize into *shear bands* of typically 10-50 particle diameters wide [13, 14, 15, 16, 17], which is very different from usual hydrodynamics. Fenistein and van Hecke [18] have visualized these shear bands using tracer particles at the top surface of a cylindrical container with a rotating outer wall, see the top views of Fig. 1.5. The first two images show the deformation of an initially straight line of black tracers: there were practically no velocity gradients during the experiment, except in a very localized shear band. The third image was taken after *reversing* the direction of the shear and reveals yet another memory effect: the tracers in the shear

zone do not return to their initial positions. Losert and Kwon also found that reversing the shear in a Taylor-Couette cell results into some short transient state [19], which they speculate to be due to the 'softness' perpendicular to the principle force axis. This principle axis is oriented at 45° like in Fig. 1.4 and has to rearrange after the direction of shear has been reversed. These experiments nicely illustrate that there is indeed an intricate interplay between static and flowing behavior, for which the physics of force networks may play a crucial role.
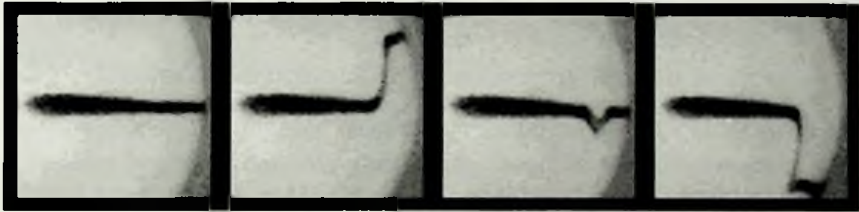
Figure 1.5: The behavior of slowly sheared granular matter in a cylindrical container, visualized by tracer particles on the top surface (black line). The material has been sheared according to the following procedure: *(i)* initial state (at rest), *(ii)* applying a counterclockwise rotation of the outer wall, *(iii)* reversing the direction of shear towards its original position and *(iv)* beyond. Taken from Fenistein and van Hecke [18].

1.3.2 The carbon paper experiment

After discussing these aspects of spatial structure, we now consider the statistical distribution of forces f, usually denoted as $P(f)$. This probability density function reflects the large force fluctuations that are clearly visible in Fig. 1.2, and forms a basic characteristic of the force network. However, it is very difficult to quantify the forces from the interference pattern on a single photoelastic particle. More accurate force measurements can be obtained at the *boundary* of a 3D system, where grains are in contact with a wall [20, 21, 22, 23]. This has mainly been done in the experimental group in Chicago, by deducing the *particle-wall* forces from imprints on carbon paper at the walls of a container [20, 21, 22]. For reasons that will become clear later, we will refer to these particle-wall forces as w and to their probability distribution as $\mathcal{P}(w)$. In a systematic series of experiments, the Chicago group typically obtained $\mathcal{P}(w)$ such as depic-

ted in Fig. 1.6: it decays exponentially for large particle-wall forces, but for small forces it 'flattens' to some finite value. One of their most striking results is that the distributions for almost perfectly crystalline packings (fcc or hcp) are qualitatively identical to those measured using amorphous packings. So even if the packing geometry is very regular, there are still large force fluctuations leading to a nontrivial exponential tail.
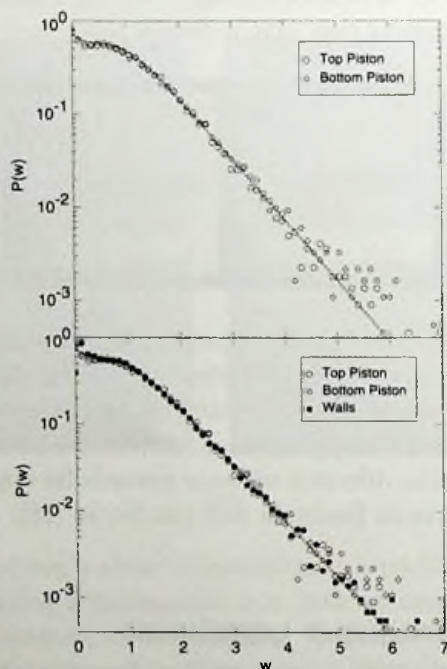
Figure 1.6: Typical particle-wall force distributions $\mathcal{P}(w)$ measured at the top, bottom and at the sidewalls of a container, using the carbon paper method. The distribution has a broad exponential tail, and has a plateau for small w. Data are normalized such that $\langle w \rangle = 1$. Figure taken from Mueth et al. [21]; in order to be consistent throughout this thesis we adjusted the notation to $\mathcal{P}(w)$.

These experiments have been the motivation for a wide variety of theoretical studies, including the work presented in this thesis. There is, however, an intrinsic problem with the experimental method: it probes the *particle-wall* forces at the boundary and not the *interparticle* forces in the bulk of a granular system. So, in order to acquire information

about bulk behavior, it is crucial to understand how the distribution of bulk forces $P(f)$, relates to the measured particle-wall force distribution $\mathcal{P}(w)$. This problem constitutes one of the main questions addressed in this thesis. It will lead us to formulate a framework relating the statistics of force networks to the local packing geometry. In Chapter 2 we further discuss some recent experimental results on highly deformed packings of soft (rubber) particles, for which we propose a tentative interpretation.

1.4   Theoretical aspects

1.4.1   Underdetermination on different length scales

microscopics – The physics of static granular matter involves problems on various length scales. We mentioned that the forces between two individual particles depend on the history of the contact, which is reflected by the inequality in Coulomb's law of friction. This causes fundamental problems already on the level of a single grain, as is illustrated by a nice example by Halsey and Ertas [24]. For the disk in a (2D) wedge sketched in Fig. 1.7, there are four unknowns, i.e. two normal and two tangential contact forces. However, there are only three equations that describe mechanical stability: force equilibrium in two directions and torque balance. Hence, even such a simple system can not be solved without knowing the microscopic details of the contacts, or by making additional assumptions.
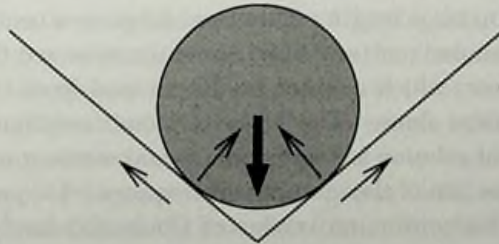
Figure 1.7: A disk in a wedge under gravity (fat arrow): the three equations of mechanical equilibrium are not sufficient to determine the four unknown contact forces.

mesoscopics – This problem of underdetermination persists for assemblies of grains, even in the absence of friction. For a d dimensional packing

of frictionless spheres, there will be d equations per particle for $z/2$ unknowns, where z is the average coordination number. For example, a perfectly ordered fcc packing has $12/2 - 3 = 3$ undetermined forces per particle, leaving ample room for force fluctuations. Another extreme limit is that of a so-called *isostatic* packing, in which the coordination number precisely equals $2d$ so that all forces are uniquely determined [25, 26]. In this case, force fluctuations can only arise due to packing disorder. The actual coordination number of a packing depends on parameters like polydispersity, friction coefficient, particle stiffness, applied pressure etc. [27, 28, 29]; isostaticity is only found in the limit of infinitely hard polydisperse frictionless spheres. The importance of the number of contacts will be further worked out in Chapters 2 and 6.

On a mesoscopic level, static granular matter is thus described by a packing geometry, specifying positions and directions of the interparticle forces, and the force balance equations. A successful approach to this problem has been to ignore the microscopic contact mechanics and treat the undetermined degrees of freedom as stochastic variables. This has been initiated by Liu *et al.* [20, 30], who proposed a stochastic lattice model to study force fluctuations in bead packs. This so-called q-model is the only analytically accessible model that gives an explicit prediction for the force distribution. It will therefore play an important role in this thesis. We define the q-model in Sec. 1.4.4, and the model will be studied in detail in Chapters 3 and 4. At the end of this thesis, in Chapter 6, we present a new strategy to deal with the undetermined degrees of freedom.

macroscopics – On large length scales, one can go to a continuum description of static granular matter. Now, the unknowns are the components of the stress tensor, which can not be determined from the equations of mechanical stability alone. The Mohr-Coulomb continuum theory [31] uses an additional relation between the normal stress σ and shear stress τ: on any cross-section of the material one requires $|\tau| < \mu\sigma$, otherwise the material fails. This continuum version of Coulomb's law[3] is most clearly manifested by the slopes of sand dunes, whose angles can not exceed a maximum value $\arctan\mu$.

The equations can also be closed by 'constitutive equations', which usually are relations between stresses and strains (deformations) or strain

---

[3]The phenomenological friction coefficient μ depends not only on material properties of the grains, but also on the packing geometry; e.g. for a thin layer of grains, μ depends on the height of the layer [32].

rates. Finding constitutive equations is a fundamental problem for any complex material. A particular complication of granular matter is that it is not clear whether the strain tensor is a well-defined quantity — see e.g. [3, 34]. Claudin *et al.* therefore proceed along the lines of Mohr-Coulomb theory, using constitutive relations between the components of the stress tensor [33, 34]. One important consequence of their approach is that the stress fields are described by *hyperbolic* (wave-like) equations, for which the stresses propagate along linear stress paths. This approach is in conflict with theories based on elasticity, which lead to *elliptic* equations for the stress fields [3, 35, 36, 37]; in the latter case, the stress propagation is not dramatically different from a conventional solid. There is presently much ongoing experimental and numerical work to resolve this issue.

1.4.2 Jamming and force chains

After the discussion of the previous paragraphs, it is clear that we are far from deriving coarse grained continuum equations from the mechanics of individual grains. A tentative idea to bridge this gap via the mesoscopic physics of force networks, has been proposed in the context of *jamming* [38]: the dynamic transition occurring in a wide variety of 'glassy' systems may be related to the emergence of a percolating force network [39, 40].

This idea is supported by simulations of supercooled liquids, foams and granular media, in which the distribution of forces $P(f)$ has been observed to undergo a 'universal' change at the jamming transition [39, 41]. The data of Fig. 1.8 were obtained from molecular dynamics simulations of particles with a Lennard-Jones repulsive interaction, i.e. without the attractive tail, for quenches above and below the glass transition temperature [39]. As the system becomes glassy, the plateau for small forces changes to a small peak around the average value. Intriguingly, one observes the very same behavior in simulations of foams and granular media.

It is perhaps good to point out that the force distribution $P(f)$ is just a different representation of the pair distribution function $g(r)$ [39], which is a more conventional object in the study of the glass transition. For any force resulting from a pair potential $V(r)$, we can write

$$P(f) \quad \propto \quad \int_0^\infty dr\, r^2 g(r)\, \delta\left(f + V'(r)\right)$$
$$\propto \quad r^2 g(r)\, /\, |V''(r)| , \tag{1.4.1}$$

where r must be expressed in terms of f. Although it is known that $g(r)$

undergoes little change at the glass transition [42], for steep potentials $P(f)$ is much more sensitive than $g(r)$ for configurational changes at small length scales. This is because with such potentials one can access the whole force range by only minute changes of the interparticle distances.
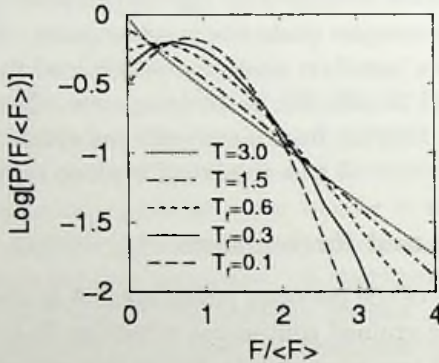
Figure 1.8: The distribution of interparticle forces $P(f)$ in a supercooled liquid of Lennard-Jones-like particles. Below the glass transition $T < T_g = 1.1$, the force distribution develops a maximum around its average value. Figure taken from O'Hern *et al.* [39].

An intuitive concept associated with this idea is the notion of *force chains*, which are lines of large forces percolating through the material. This has motivated Bouchaud *et al.* [43, 44] to propose a model for static granular media based on splitting and merging of these force chains. Despite the fact that force chains have become a widely accepted concept in the community, *there is still no sharp definition of a force chain.* Of course, mechanical equilibrium requires large forces to propagate more or less linearly on the scale of a few grains. But whether this leads to the formation of a mechanical 'backbone' for the material, or to some irrelevant short-range correlation remains an important open question. In fact, simulations by Goldenberg and Goldhirsch [37] indicate that the stress tensor, which is a coarse grained average over the microscopic forces, bears little or no resemblance of force chains even for coarse graining on the scale of a single particle.

1.4.3   Fundamental questions

Let us now summarize the basic questions that were encountered in the previous discussions on both experimental and theoretical aspects of static granular media.

force distributions – The first questions concern the probability distribution of forces, which characterizes the large fluctuations of force networks. Experiments [20, 21, 22, 23], numerical simulations [27, 45, 46, 47, 48, 49, 50] and theory [20, 30] all find that this distribution decays exponentially, albeit with varying exponents. The small force behavior is less well settled: the q-model seems to predict a vanishing probability density for small forces, whereas experiments and simulations clearly show that this remains non-zero. This small force behavior is relevant since it may indicate arching [33] or jamming, as has been discussed in the previous section.

   This problem of small forces will be addressed in detail in this thesis alongside two related experimental problems. The first is how the probability distribution measured at the boundary relates to the force distributions in the bulk. The second question is whether a highly compressed granular assembly crosses over to a 'usual' elastic solid with Gaussian fluctuations instead of an exponentially decaying $P(f)$ [27].

propagation of stress and fluctuations – Another fundamental topic concerns the equations for stress propagation, to which we alluded in Sec. 1.4.1. Many experiments [11, 51, 52, 53] and simulations [48, 54] have recently been devoted to clarify this issue, in particular by examining the response to a localized load applied on the top surface. Most studies report that the response function (or Green's function) scales linearly with depth, excluding the diffusion-like *parabolic* propagation predicted by the q-model. However, since the results strongly depend on both the geometry and the history of the packing, it remains difficult to distinguish whether the stress fields are described by hyperbolic or elliptic equations. For a detailed discussion, we refer to [34].

   In this thesis we propose an additional test to qualify the various theoretical models. At the top of a pile there are little force fluctuations, since the particles are of approximately the same weight. When going down below the top surface, how do the force fluctuations build up towards an exponentially decaying distribution? Like the Green's function experiments, this again concerns the relaxation from the top surface into

the bulk, but now of the force fluctuations instead of the (average) spatial response.

from statics to dynamics – Maybe the most difficult open problem is to understand how packing effects influence the rheology in situations of slow flow. There are models starting from conservation of mass, momentum and energy like in normal hydrodynamics [55, 56, 57, 58]. The problem is, as usual, to express the stresses as a function of the flow field and other parameters like volume fraction, granular temperature etc. In this chapter we have discussed several experiments displaying history dependence and the emergence of structures on a mesoscopic scale; these features obviously tend to complicate a hydrodynamic description.

A somewhat different approach to the problem of static-dynamic interaction is provided by the concept of jamming, in which one draws an analogy with the glass transition [38, 59, 60] (see Sec. 1.4.2). From the perspective of this thesis there are two important questions concerning this issue: what is the origin of the observed 'universal' transition of $P(f)$ at the jamming transition, and what is the physical relevance of the concept of force chains?

1.4.4   The q-model

Although the q-model involves some serious simplifications of the physics, it forms an extremely rich (analytical) starting point for the theoretical study of static granular media. The model is defined as follows. The grains are assumed to be positioned on a regular lattice. Let W_i be the total force in the downward direction on the ith bead in a layer; we refer to this total vertical force as the *weight* on a particle. This bead makes contact with a number of n_c beads in the layer below, which we indicate by the indices $i + \alpha$. The α's are 'displacement vectors' in the lower layer,[4] as shown in Fig. 1.9. Bead i transmits a fraction $q_{i,\alpha}$ of the weight W_i to the bead $i + \alpha$ underneath it. These fractions are taken stochastically from a distribution satisfying the constraint

$$\sum_\alpha q_{i,\alpha} = 1 \qquad \text{for all} \quad i , \qquad\qquad (1.4.2)$$

---

[4]This formulation using displacement vectors is not common in the literature, but it greatly simplifies the notation for three and higher dimensional packings.

which assures mechanical equilibrium in the vertical direction. So, we can write the weight W'_j on the jth bead in the next layer as

$$W'_j = 1 + \sum_\alpha q_{j-\alpha,\alpha} W_{j-\alpha} ,$$ (1.4.3)

where the so-called *injection term*, $mg = 1$, represents the mass of a single particle. Due to the stochastic character of the $q_{i,\alpha}$, the weights become distributed according to a weight distribution $\mathcal{P}(W)$ that, after proper rescaling, converges towards a stationary form at large depths.
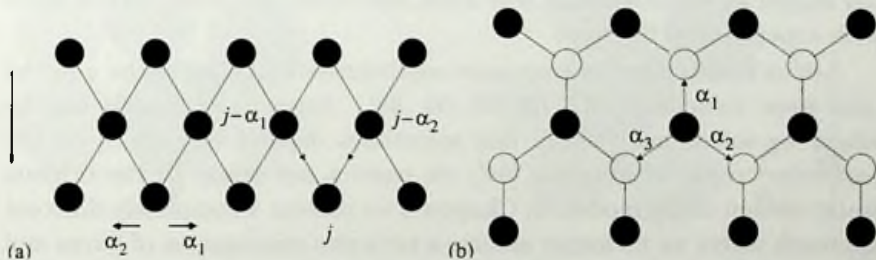
Figure 1.9: The displacement vectors α in the q-model for *(a)* the triangular packing (side view) and *(b)* the fcc packing (top view).

Thus in this *scalar* model, the complicated problem of two or three dimensional force equilibrium is projected onto the vertical direction; the undetermined fractions along the bonds are generated stochastically from a q-distribution satisfying the constraint of Eq. (1.4.2). As a generic case, one can take a uniform q-distribution, which assigns an equal probability to each set of q's obeying Eq. (1.4.2). With this uniform distribution, the weights become distributed according to a stationary distribution [30]

$$\mathcal{P}(w) = \frac{n_c^{n_c}}{(n_c - 1)!} w^{n_c-1} e^{-n_c w} ,$$ (1.4.4)

where w is the rescaled weight $W/\langle W \rangle$, and as already defined above n_c is the number of bonds 'arriving' at a site. A derivation of this result can be found in Sec. 3.3.

So indeed, the q-model provides a quantitative way to understand the exponential tail of the weight distribution.[5] However, this simple model

---

[5]This exponential tail is robust for all q-distributions as long as the whole interval of allowed q-values $[0, 1]$ is being explored. If there is some $q_{max} < 1$, the decay becomes faster, i.e. $\sim e^{-aw^\beta}$ with $\beta = \log(n_c)/\log(q_{max}n_c)$ [33].

can not be expected to capture all physics in detail. For example, the prediction $\mathcal{P}(0) = 0$ is not consistent with the experimental data of Fig. 1.6; in this thesis we demonstrate that this is due to the regular contact geometry that is assumed in the model. There is another important deficiency of the model, namely that the average response to a localized force on the top layer is diffusion-like (see Sec. 4.3), and does not scale linearly with depth. Claudin *et al.* [33] argue that this is because mechanical equilibrium in the horizontal direction(s) has been ignored, which artificially enhances a (narrow) downward propagation. One can thus gain substantial insight by understanding why some aspects do and others do not agree with experimental findings.

Let us finally mention that more sophisticated versions of the q-model have been formulated [61, 62, 63, 64, 65]. Since these models can no longer be solved analytically and sometimes depend very much on the particular 'rules' of iteration [64], we restrict our study to the original scalar version of the model. In Chapter 6 we present a completely different approach where we no longer assume a recursive propagation of forces and weights, but instead solve the 2D equations of mechanical equilibrium 'simultaneously'.

1.5 This thesis

After this general introduction on the physics of static granular matter, let us specifiy the topics that will be addressed in this thesis.

In Chapter 2 we investigate the relation between packing geometry and the statistics of force networks. Based on the results of molecular dynamics simulations, we develop a simple 'geometrical framework' that captures the essential physics of the problem. The crucial step in our approach is to make an explicit distinction between the distribution of interparticle forces $P(F)$ and the weight distribution $\mathcal{P}(W)$; the weight is defined as the sum of the vertical components of all downward pointing forces on a particle

$$W_j \equiv m_j g + \sum_{<i>} (\vec{F}_{ij})_z \; , \qquad (1.5.1)$$

so the sum runs over all interparticle forces $\vec{F}_{ij}$ pushing on particle j *from above*. From Fig. 1.10a, it is clear that the particle-wall forces probed by the carbon paper experiments are essentially equal to the weights. We

apply our framework to recent experimental data, and extract inform-
ation about $P(F)$ within the bulk from these boundary measurements.
For particles in the bulk, the definition of the weight provides a natural
connection to the q-model (see Fig. 1.10b). We make a detailed compari-
sion between this model and our simulations, and we solve the discrepancy
with experiments for small weights that has been discussed in the previous
section.
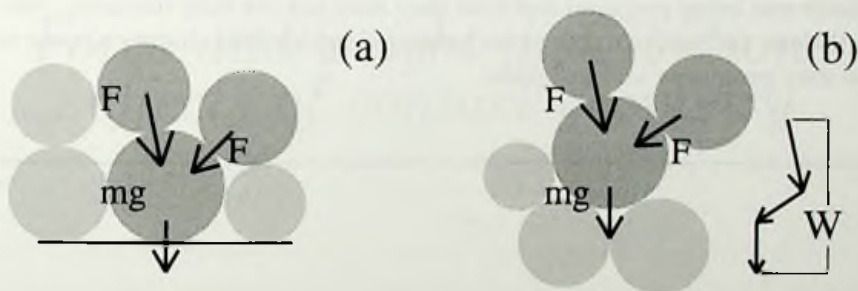
Figure 1.10: Definition of the weight W of *(a)* a bottom particle and *(b)*
a bulk particle. The force between a bottom particle and the bottom
support, which is measured in experiments, is equal to the weight of this
particle.

We then turn to a detailed analytical survey of the q-model. In
Chapter 3 we determine the entire class of exact solutions for which all
weight correlations dissappear at large depths. This forms a generaliza-
tion of the result of Eq. (1.4.4) that holds for the uniform q-distribution.
We furthermore demonstrate that in general the weights *do* become cor-
related, and we reveal the remarkable nature of these correlations. In
Chapter 4 we then study the relaxation of $\mathcal{P}(w)$ towards the stationary
state as a function of depth. Since this provides a fundamental test of top-
down relaxation of fluctuations in granular matter, we have confronted
these results with our molecular dynamics simulations (this comparison is
already given in Chapter 2 where we anticipate the q-model results).

The work presented in Chapter 5 is not directly related to granular
matter. It consists of an analytical study of the Asymmetric Random
Average Process (ARAP), which is a non-equilibrium model for one di-
mensional interacting particles moving on a continuous line. This model
can be mapped onto the q-model, and we have extended some of our pre-
vious results to this ARAP. Due to the different dynamics of the ARAP,

we encounter interesting new features that are not present in the q-model.

Finally, we present a new approach to the problem of force networks in Chapter 6, in which we exploit the undetermined degrees of freedom of mechanical equilibrium. Very much like in the microcanonical ensemble of classical statistical mechanics, we propose to integrate over these degrees of freedom assuming an a priori equal probability for all force configurations. We would like to stress that these ideas have emerged while this thesis was being prepared and that they have not yet fully matured. Nevertheless, the preliminary results presented in this final chapter appear to be very promising and insightful.

Force and weight distributions: effects of contact geometry

2.1   Introduction

In this chapter we will unravel the effect of the local contact geometry on the distributions of interparticle *force F* and effective particle *weight W*. The weight of a particle has been defined in the previous chapter as the sum of the vertical components of all downward pointing forces on a particle, i.e.

$$W_j \equiv m_j g + \sum_{<i>} (\vec{F}_{ij})_z \,. \tag{2.1.1}$$

From Fig. 1.10 it is clear that experiments measuring particle-wall forces can only access weight distributions $\mathcal{P}(W)$ and not interparticle force distributions $P(F)$. Using molecular dynamics simulations of frictionless spheres, we construct 2D packings such as shown in Fig. 2.1, for which we investigate how the force and weight distributions are related. Based on the results of these simulations, we develop a simple geometrical framework that captures this relation. It turns out that the *local packing geometry* plays a crucial role in the relation between $P(f)$ and $\mathcal{P}(w)$ (we define $f = F/\langle F \rangle$ and $w = W/\langle W \rangle$ as the appropriately rescaled forces and weights). Our central point is that while the distribution of f is robust, the distribution of w is profoundly influenced by the contact geometry, in particular by *the number of downward pointing contact forces*

n_c. Since the packing geometry near a boundary is rather special, we will find that $\mathcal{P}_{boundary}(w)$ is different from $\mathcal{P}_{bulk}(w)$. However, for many (but not all) experimentally relevant situations, the special packing geometry near a boundary makes $\mathcal{P}_{boundary}(w)$ rather close, but not equal, to the bulk $P(f)$. This fortunate but non-trivial coincidence can be understood easily within our framework. We will, however, also provide examples where $\mathcal{P}_{boundary}(w)$ and bulk $P(f)$ are significantly different. In particular we apply our framework to recent experimental data on highly deformed packings of soft rubber particles, where indeed $\mathcal{P}_{boundary}(w)$ is very different from $P(f)$.

Additional motivation for studying the relation between forces, weights and geometry comes from the q-model, which has been defined in Sec. 1.4.4. Once the distinction between forces and weights has been made, one notices that the q-model is a lattice model in which *weights* are randomly redistributed over a *fixed* number of supporting grains. The q-model displays weight distributions that are qualitatively different from experimentally observed weight distributions. We will show that this is due to the fixed connectedness of the q-model. Realistic $\mathcal{P}(w)$ can be obtained if we allow for the connectivity to vary within the q-model, e.g. by introducing random connections.

Finally, we study the top-down relaxation in the simulations on Hertzian sphere packing and compare it to the top-down relaxation predicted by the q-model; a derivation of the results for the q-model will be presented in Chapter 4.

2.2   Statistics of interparticle forces

In this section we study the distribution of interparticle forces via simulations of 2D packings of frictionless spheres. After introducing our numerical method in Sec. 2.2.1, we discuss the similarities between $P(f)$ in the bulk and near the boundary in Sec. 2.2.2. We also study the angular distribution and the probability distribution of the z components of the contact forces in Sec. 2.2.3, and close with a brief summary of results.

2.2.1   Numerical method and parameters

Our 2D packings consist of frictionless, 3D particles under gravity. These are created from molecular dynamics simulations of spheres that interact
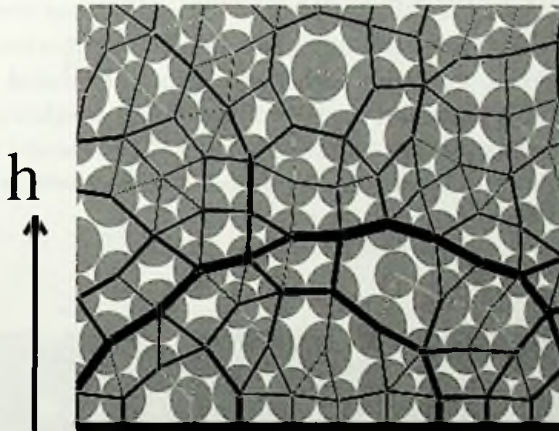
Figure 2.1: Detail of a typical packing in our simulations; the height h denotes the distance from the bottom. The force network is represented by the black lines whose thickness represent the force magnitude.

through so-called Hertzian forces, where $f \propto \delta^{3/2}$ (for 3D particles) and δ denotes the overlap distance [8]. The particles live in a container that is 24 particle diameters wide, with periodic boundary conditions in the horizontal direction. The bottom support is rigid and also has a friction-less Hertzian interaction with the particles. We contruct our stationary packings by letting the particles relax from a gas-like state by introducing a dissipative force that acts whenever the overlap distance is non-zero. In this paper we use two different polydispersities: the radii r are drawn from a flat distribution between either $0.49 < r < 0.51$ or $0.4 < r < 0.6$. The masses are proportional to the radii cubed. In the former case of almost monodisperse particles, the particles tend to crystallize into a tri-angular lattice (Sec. 2.4.1), whereas the more polydisperse particles lead to amorphous packings such as shown in Fig. 2.1. This allows us to study how the packing geometry affects the force network. The results shown in this paper are obtained with particles that deform 0.1% under their own weight. Simulations of harder particles (deformation 0.01%) gave similar results as those shown here.[1]

---

[1]There is a difference between the packings of 'soft' particles (deformation 0.1%) and 'hard' particles (deformation 0.01%). The average coordination number of the hard particles is smaller than that of the soft particles, leading to a significant number

The various data were obtained from 1100 realizations containing 1180 particles each. We study the force and weight distributions at various heights h. To do so, we divide each packing into horizontal slices of one particle diameter height, and rescale all forces and weights in each layer to the corresponding average (absolute) values. The rescaled interparticle forces and weights will be denoted by $\vec{f}$ and w respectively, with distributions $P(\vec{f})$ and $\mathcal{P}(w)$.

2.2.2   Absolute values of $\vec{f}$: $P(f)$

We first analyze the statistics of the absolute values $f = |\vec{f}|$, whose probability density function $P(f)$ is usually referred to as the distribution of (interparticle) forces; our main finding will be that $P(f)$ in bulk and near the boundary are very similar. In Fig. 2.2a we show $P(f)$ as measured in the bulk of the *amorphous* packings (particle radii between $0.4 < r < 0.6$). At different heights between $10 < h < 30$, $P(f)$ was not observed to change; the open circles represent an average over these various heights. Even very close to the bottom support, we find that $P(f)$ remains almost unchanged: the dotted dataset has been obtained from the forces between the bottom particles and the particles in the layer above. We refer to these forces as *layer-to-layer* forces near the bottom – see Fig. 2.2b. So, although the bottom wall locally alters the packing geometry, the shape of $P(f)$ is essentially unaffected.

As can be seen from the inset of Fig. 2.2, the probability density decays slightly faster than exponentially. This is consistent with simulations by Makse *et al.* [27] who found that $P(f)$ crosses over to a Gaussian for large particle deformations; we have used rather 'soft' particles in our simulations for which deformations are relatively large, i.e. up to 2%. We come back to the effect of deformation in experiments in Sec. 2.4.2. For small forces, $P(f)$ approaches a constant value. The small peak around $f = 0.7$ for bulk forces becomes a plateau for the layer-to-layer forces near the bottom; it is intriguing to note that this change is reminiscent of what is proposed as an identification of the jamming transition [39, 41].

---

of *rattlers*, i.e. particles that feel no force from above. Since the forces carrying these rattlers are of the order $mg \ll \langle F \rangle$, they show up as δ-peaks at zero force; besides these δ-peaks, $P(f)$ in both systems are virtually indistinguishable.
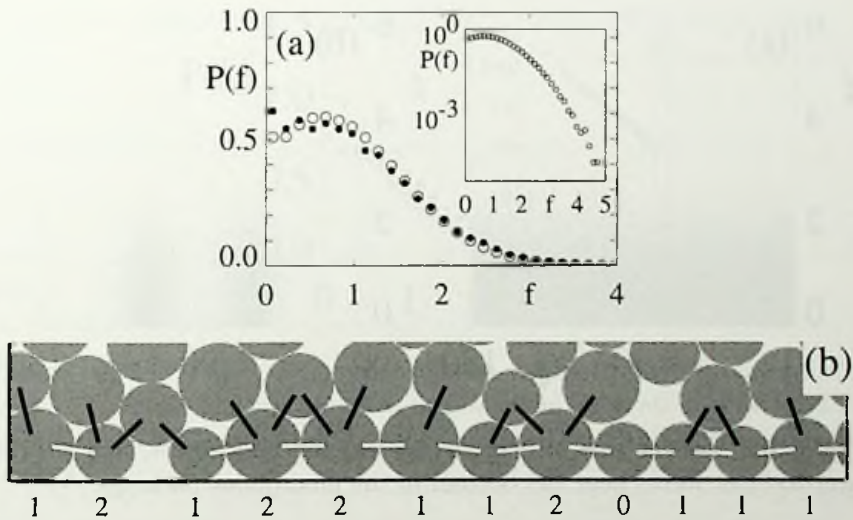
Figure 2.2: *(a) $P(f)$ for amorphous packing in the bulk (open circles) and for the layer-to-layer forces near the bottom (dots); the inset shows $P(f)$ for bulk forces on a log-lin scale. Note that the force distributions are very similar, except for a small difference for small f. (b) Detail of a typical packing near the bottom showing layer-to-layer forces (black lines) and the intralayer forces (white lines) near the bottom. It is clear that the layer-to-layer forces are dominant in determining the weights w of the bottom particles. The numbers show the values of n_c, the number of forces that contribute to these weights.*

2.2.3 Orientations of $\vec{f}$ and $P(f_z)$

After studying the absolute values of $\vec{f}_{ij}$, let us investigate the *orientations* of the interparticle forces. We therefore define φ_{ij} as the angle between $\vec{f}_{ij}$ and the horizontal axis. In Fig. 2.3a we show the scatterplot of (f_{ij}, φ_{ij}) in the bulk: the angles are uniformly distributed and independent of the absolute value of $\vec{f}$. So, the packings are highly disordered away from the bottom. Near the boundary, however, this isotropy is broken strongly. The presence of the bottom wall aligns the bottom particles and as a consequence their interparticle forces become almost purely horizontal, see Fig. 2.2b. It is clear that near the bottom the interparticle forces naturally divide up into these almost horizontal *intralayer* forces, and
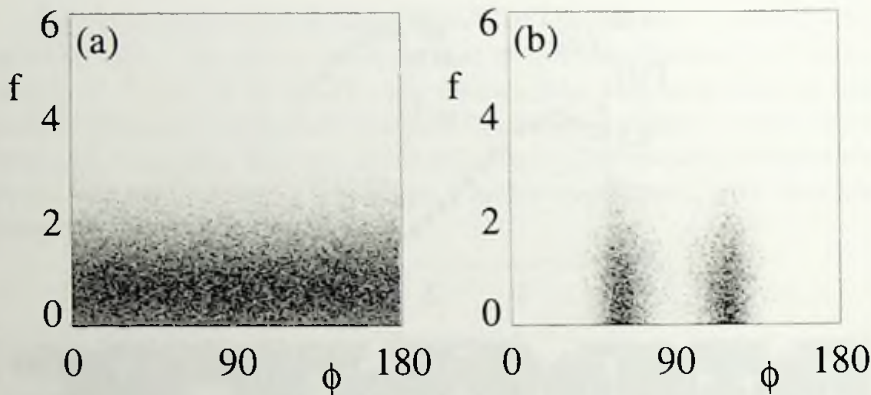
Figure 2.3: Scatter plot of (f_{ij}, φ_{ij}) for *(a)* the bulk forces, and *(b)* the layer-to-layer forces near the bottom in the amorphous packings.

layer-to-layer forces connecting bottom particles with those in the layer above. The orientations of these layer-to-layer forces are concentrated around $\pi/3$ and $2\pi/3$, as can be seen from Figs. 2.2b and 2.3b.

Since the particle *weights* are derived from the z-components of the forces, $f_z = \left(\vec{f}_{ij} \right)_z$, we now investigate the distribution $P(f_z)$. The bottom-induced orientational order discussed above is reflected in the statistics of the f_z. According to Fig. 2.4, there is a substantial difference between $P(f_z)$ in the bulk (open circles) and $P(f_z)$ for the layer-to-layer forces near the bottom (dots). This difference can be understood as follows. Assuming that the φ_{ij} are indeed uncorrelated to the f_{ij}, we can write

$$P(f_z) = \int_0^\pi d\varphi \, \Phi(\varphi) \int_0^\infty df \, P'(f) \, \delta \left(f_z - f \sin(\varphi) \right), \qquad (2.2.1)$$

where $\Phi(\varphi)$ is the angle distribution, and $P'(f)$ is the distribution of the absolute values $|\vec{f}|$ of Fig. 2.2. Note that $\langle f_z \rangle < 1$. For the layer-to-layer forces near the bottom, we have seen from the scatter plot that the values of $\sin(\varphi)$ are concentrated around $\frac{1}{2}\sqrt{3} \approx 0.866$. In the approximation that the distribution of $\sin(\varphi)$ is sharply peaked, the shape of $P(f_z)$ equals that of $P(f)$ (up to a scale factor). This is indeed confirmed by direct comparison of the dotted datasets of Figs. 2.2 and 2.4.

In the bulk, we have seen that the packing geometry is isotropic. A consequence of this isotropy is that the probability density function of
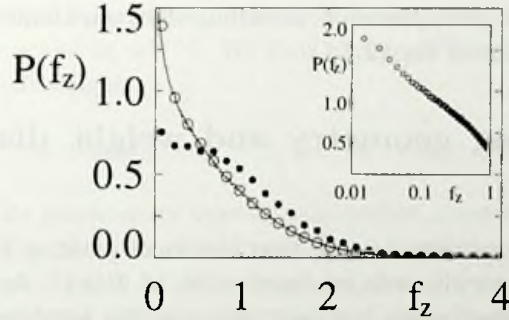
Figure 2.4: $P(f_z)$ in the bulk (open circles) and for the layer-to-layer forces (dots). The solid line was obtained by numerical integration of Eq. (2.2.2). Inset shows $P(f_z)$ versus $\log f_z$, confirming the logarithmic divergence for small f_z.

the horizontal components $P(f_x)$ is identical to $P(f_z)$ (not shown here). Again, one can use Eq. (2.2.1) to understand the shape of $P(f_z)$. Taking a uniform angle distribution $\Phi(\varphi) = 1/\pi$, we obtain (appendix 2.A)

$$P(f_z) = \frac{2}{\pi} \int_{f_z}^{\infty} df \, \frac{P'(f)}{\sqrt{f^2 - f_z^2}} \ . \tag{2.2.2}$$

Numerical integration of this equation with $P'(f)$ from Fig. 2.2 yields the solid line in Fig. 2.4, which closely corresponds to the $P(f_z)$ as measured in the bulk (open circles). In appendix 2.A, we show that the integral of Eq. (2.2.2) is weakly divergent for small f_z:

$$P(f_z) = -\frac{2}{\pi} P'(0) \, \ln(f_z) + \mathcal{O}(1) \ . \tag{2.2.3}$$

The inset of Fig. 2.4 shows that our data for $P(f_z)$ is indeed consistent with this logarithmic divergence.

2.2.4 $P(f)$: summary

Let us briefly summarize the results of this section. The geometrical constraint imposed by the bottom wall locally induces a packing geometry which is different from the bulk geometry. Although this is strongly reflected in the orientations of the $\vec{f}_{ij}$, the distribution of the absolute values $P(f)$ is very robust. The probabilities for the components of the $\vec{f}_{ij}$ can

be obtained with great precision, including the logarithmic divergence, by the transformation of Eq. (2.2.1).

2.3 Packing geometry and weight distributions $\mathcal{P}(w)$

In this section, we demonstrate that the local packing geometry has a dramatic effect on the weight distribution of $\mathcal{P}(w)$. As stated in the introduction, experiments can only measure the particle-wall forces at the boundary of a granular packing, and not the interparticle (bulk) forces that were discussed in the previous section. Since these particle-wall forces are essentially equal to the weights of the bottom particles, it is important to understand the relation between the weight distribution $\mathcal{P}(w)$ and the distribution of interparticle forces $P(\vec{f})$. In the first part of this section we develop a simple geometrical framework to understand this relation, based on phase space considerations. We then show that this explains, to a large extent, the weight distributions $\mathcal{P}(w)$ as measured in our simulations of Hertzian spheres. In particular, we observe substantial differences between weight distributions for different packing geometries.

2.3.1 Geometrical framework: decomposition of $\mathcal{P}(w)$ according to number of contacts n_c from above

If we interpret the definition of weights in Eq. (2.1.1) as a transformation of stochastic variables, it is possible to relate the corresponding probability density functions as

$$
\begin{aligned}
\mathcal{P}_{n_c}(w) \;=\; & \int_0^\infty d(\vec{f}_1)_z \cdots \int_0^\infty d(\vec{f}_{n_c})_z \\
& \times \; P\left((\vec{f}_1)_z, \cdots, (\vec{f}_{n_c})_z\right) \, \delta\left(w - \sum_{i=1}^{n_c} (\vec{f}_i)_z\right).
\end{aligned}
$$

(2.3.1)

Here, we have neglected the term mg, since $mg/\langle W \rangle \ll 1$ far below the top surface of the packing. The number of forces over which we integrate differs from grain to grain, and it turns out to be crucial to label the weight distribution in Eq. (2.3.1), $\mathcal{P}_{n_c}(w)$, according to this number n_c. This can be seen as follows. The δ-function constrains the integral on a

$(n_c - 1)$ dimensional hyperplane of the total phase space, and the 'area' of this hyperplane scales as w^{n_c-1}. We thus anticipate the following scaling behavior for small weights:

$$\mathcal{P}_{n_c}(w) \propto w^{n_c-1} \quad \text{for} \quad w \to 0 , \tag{2.3.2}$$

provided that the phase space density approaches a constant value when all $(\vec{f_i})_z \to 0$. The particles that do not feel a force from above, $n_c = 0$, give a δ-like contribution at $W = mg$; for deep layers this occurs for $w \ll 1$. In a disordered packing, the number of particles that exert a force from above can vary from grain to grain. The total weight distribution $\mathcal{P}(w)$, therefore, is a superposition of the $\mathcal{P}_{n_c}(w)$:

$$\mathcal{P}(w) = \sum_{n_c} \rho_{n_c} \, \mathcal{P}_{n_c}(w) , \tag{2.3.3}$$

where ρ_{n_c} is the fraction of particles with n_c contacts from above. This means that the small weight behavior of $\mathcal{P}(w)$ depends very much on the fractions ρ_{n_c} and thus on the local packing geometry, via Eqs. (2.3.2) and (2.3.3).

The steepness of the tail of the total weight distribution depends strongly on the ρ_{n_c} as well. To explain this, let us assume that all vertical forces f_z contributing to the weight are uncorrelated. We consider $P(f_z) \propto e^{-\alpha f_z}$ for large forces, with a certain $\langle f_z \rangle < 1$. It follows from Eq. (2.3.1) that the weight distribution takes over this same exponent, i.e. $\mathcal{P}_{n_c}(w) \propto e^{-\alpha w}$. However, the resulting $\mathcal{P}_{n_c}(w)$'s are not properly normalized: $\langle w \rangle_{n_c} = \langle f_z \rangle \, n_c$, since each of the f_z gives an average contribution $\langle f_z \rangle$. This yields a total average weight $\langle w \rangle = \langle f_z \rangle \sum_{n_c} \rho_{n_c} n_c = \langle f_z \rangle \langle n_c \rangle$, which has to be rescaled to unity in order to compare with experimental and theoretical results. The final weight distribution then has the following large weight behavior:

$$\mathcal{P}(w) \propto e^{-\gamma w} \quad \text{with} \quad \gamma = \alpha \langle f_z \rangle \langle n_c \rangle . \tag{2.3.4}$$

This simple calculation shows that, for a given value of α, the steepness of the tail of the experimentally measured weight distribution is very sensitive to the local packing geometry. This is a direct consequence of keeping $\langle w \rangle$ fixed to unity: a decrease of probability for small weights must lead to a steeper tail for large weights in order to leave the average weight unaltered. Note that this general argument is not restricted to uncorrelated

f_z or exponential tails. A generalization to other than exponential tails is given in Appendix 2.B.

So, we have advanced a simple picture, in which the shape of $\mathcal{P}(w)$ *depends strongly on the local packing geometry* via the fractions ρ_{n_c}. The small force behavior follows from Eq. (2.3.2) and (2.3.3), whereas Eq. (2.3.4) relates to a good approximation the exponential tails of $P(f_z)$ and $\mathcal{P}(w)$. The object one ultimately wishes to characterize is of course the force distribution $P(f)$. Since close to the boundary $P(f)$ and $P(f_z)$ are identical up to a scaling factor $\langle f_z \rangle$ (Sec. 2.2.3), the above equations allow to trace back the features of the force distribution from experimental measurements. Along this line, we analyze recent experimental data in Sec. 2.4.2.

2.3.2 $\mathcal{P}(w)$ in Hertzian sphere packings

We now discuss the weight distributions observed in the Hertzian sphere packings, and interpret the results within the framework developed above. Fig. 2.5a shows that in the amorphous packing $\mathcal{P}(w)$ in the bulk (open circles) is significantly different from $\mathcal{P}(w)$ of the bottom particles (dots). The probability for small weights is much larger at the bottom, and the decay for large weights is not as steep as for the bulk particles. Furthermore, the transition from bottom to bulk behavior is remarkably sharp: close to the bottom at heights between 2 and 3 (full curve), the weight distribution is already bulk-like. These results can be explained by a change in the local packing geometry, using the concepts developed in the preceding paragraphs. Consider the typical bottom configuration of Fig. 2.2b. The *intralayer forces* (white lines) are almost purely horizontal and hence do not contribute to the weights. This reduces the effective values of n_c, leading to the following fractions for the bottom particles: $\{\rho_0, \rho_1, \rho_2, \rho_3\} = \{0.08, 0.46, 0.44, 0.02\}$, where we did not count the intralayer forces for determining the values of n_c.[2] In the bulk, these fractions are different, namely $\{\rho_0, \rho_1, \rho_2, \rho_3\} = \{0.01, 0.11, 0.52, 0.36\}$, leading to a

---

[2]When determining the value of n_c, we explicitly exclude the intralayer bottom contacts; for the strongly polydisperse packings, these correspond to angles that deviate less than 13° from the horizontal. For our estimates of the bulk ρ_{n_c}'s we do not exclude any forces, i.e. the 'cutoff angle' is strictly 0°. Since the bulk is isotropic, a cutoff angle of 13° leads to a change of the order of 15%, far too little to explain the change of ρ_1 by a factor of more than 4. For simplicity we therefore have kept a 'cutoff angle' of 0° in the bulk.
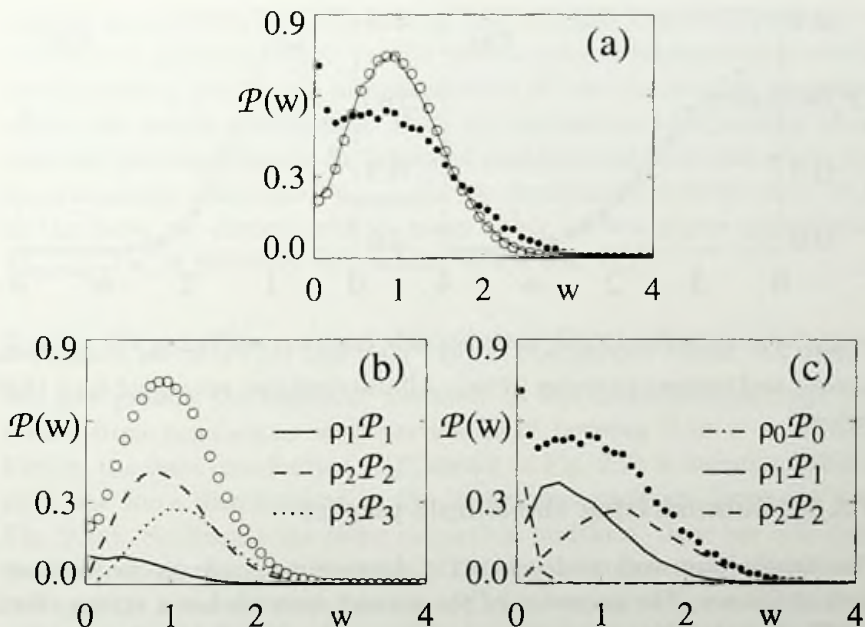
Figure 2.5: *(a)* $\mathcal{P}(w)$ in the bulk (open circles) and at the bottom (dots) in amorphous packings. At $2 < h < 3$, $\mathcal{P}(w)$ is already bulk-like (solid line). *(b,c)* Decomposition of $\mathcal{P}(w)$ according to Eq. (2.3.3) *(b)* in the bulk (open circles) and *(c)* at the bottom (dots). The measured bulk values for the fractions $\{\rho_0, \rho_1, \rho_2, \rho_3\}$ in Eq. (2.3.3) are $\{0.01, 0.11, 0.52, 0.36\}$, and the bottom values are $\{0.08, 0.46, 0.44, 0.02\}$; when determining n_c for bottom particles, we excluded the intralayer (almost horizontal) forces.

different $\mathcal{P}(w)$ via Eq. (2.3.3). Figs. 2.5b,c explicitly shows the decomposition into the $\mathcal{P}_{n_c}(w)$. Indeed, one observes the scaling behavior for small w proposed in Eq. (2.3.2). Moreover, the various $\mathcal{P}_{n_c}(w)$ are essentially the same at the bottom and in the bulk: a direct comparison is given in Fig. 2.6, where we rescaled the average values to unity. There is only a small difference in the $\mathcal{P}_1(w)$ due to the fact that bottom particles with $n_c = 1$ are typically smaller than average (Fig. 2.6a). For these particles, the intralayer forces will add a small contribution to the weights, enhancing $\mathcal{P}_1(w)$ for small w at the expense of $\mathcal{P}_1(0)$. The same argument holds for $\mathcal{P}_0(w)$, whose δ-like shape appears a bit broadened in Fig. 2.5c.
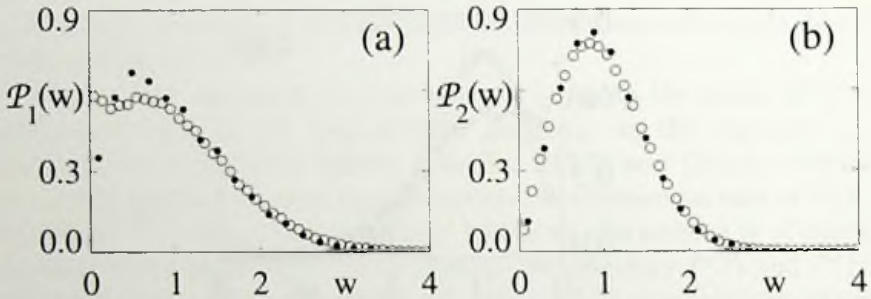
Figure 2.6: Direct comparison of (a) $P_1(w)$ and (b) $P_2(w)$ for bulk (open circles) and bottom particles (dots). All distributions are scaled such that $\langle w \rangle = 1$.

2.3.3 Summarizing the simple picture

Our simple framework as developed in the sections above can be summarized as follows: The geometry of the contact network has a strong effect on $P(w)$, but $P(f)$ is very robust. The weight distribution for particles with a given n_c, $P_{n_c}(w)$, is robust and behaves as $w^{n_c - 1}$ for small w. $P(w)$ can be decomposed as $P(w) = \sum_{n_c} \rho_{n_c} P_{n_c}(w)$, where ρ_{n_c} are the fractions of particles that have $n_c = 0, 1, 2, \ldots$ 'up' contacts. Differences of ρ_{n_c} between boundary particles and bulk particles explain the different $P(w)$'s for these cases. When ρ_0 and ρ_1 are large, the total weight distributions $P(w)$ exhibits a plateau at small weights and a slow decay at large weights; when ρ_2 and ρ_3 become large, $P(w)$ becomes sharply peaked. In this way, $P(w)$'s small weight behavior as well as its exponential decay rate for large weights reflect the packing geometry.

2.4 Manipulating the geometry: experimental relevance

So far we have focused on the role of the bottom boundary for disordered packings of frictionless particles. In this section we provide explicit examples of other types of packing geometries and their effect on $P(w)$. We first discuss our simulations of weakly polydisperse particles, which give rise to rather crystalline packings (see Fig. 2.7a). We then apply the geometrical framework derived in the previous section to experimental

(carbon paper) data by Erikson *et al.* [66] of highly deformed packings of soft rubber particles. Their results have a natural interpretation within our framework and form a nice illustration of how the number of contact affects the weight distribution. Both the simulations of crystalline packings and the experiments on deformed packings are examples where the experimentally accessible $\mathcal{P}_{boundary}(w)$ is significantly different from $P(f)$ in the bulk; we discuss why in many other carbon paper experiments $\mathcal{P}_{boundary}(w)$ is probably very similar to the real $P(f)$.

2.4.1 Crystalline versus disordered frictionless packings

We now present the results of the more or less crystalline packings, obtained from simulations with particle radii between $0.49 < r < 0.51$. Firstly, the force distribution $P(f)$ shown in Fig. 2.7b is indistinguishable from the force distributions in the amorphous packings (compare with Fig. 2.2a). So despite the order in particle positions, there are still large fluctuations in the force network. There is of course some disorder in the 'contact network' since not all particles are in contact with their six neighbors (Fig. 2.7a). It is nevertheless surprising that for this very different contact geometry, the force fluctuations are characterized by the same probability distribution as was observed for highly disordered packings. This strongly suggests that $P(f)$ is a very robust quantity and independent of the packing geometry.

The weight distribution $\mathcal{P}(w)$, on the other hand, is very sensitive for the geometry. In a perfect triangular packing all particles would have $n_c = 2$; in our simulations we find that $\rho_2 = 0.9$ and $\rho_1 = 0.1$ due to lattice imperfections. From our geometrical framework we expect that the shape of the weight distribution is dominated by $\mathcal{P}_2(w)$. Fig. 2.7c shows that this is indeed the case – e.g. compare with Fig. 2.6b.

2.4.2 Experiments on strongly deformed particles

We now demonstrate how the strategy to decompose the weight distributions according to n_c can be applied to experiments measuring $\mathcal{P}(w)$ at the boundary of a granular material. This is best illustrated by recent carbon paper experiments on soft rubber beads, in which the effect of particle deformations was investigated [66]. The raw data of these experiments, shown in Fig. 2.8, were kindly made available by the authors, allowing us to perform the analysis presented below.
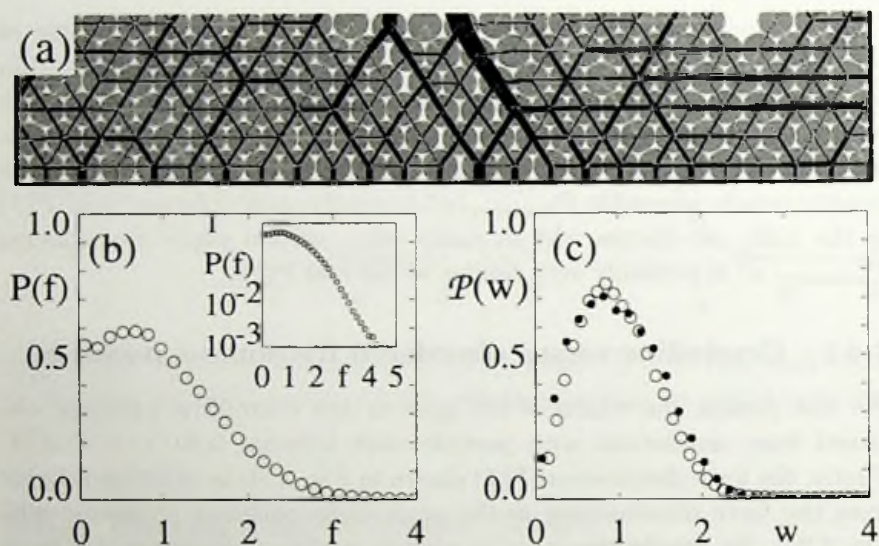
Figure 2.7: *(a)* Weakly polydisperse particles (radii between $0.49 < r < 0.51$) spontaneously crystallize into a hexagonal packing. *(b)* The corresponding $P(f)$ is indistinguishable from the force distributions in amorphous packings. *(c)* The weight distributions $\mathcal{P}(w)$ in the bulk (open circles) and at the bottom (dots) are dominated by particles with $n_c = 2$.

The experimental results of Fig. 2.8 display three trends as the compression is increased:

- The δ-like peak at $w = 0$ decreases,
- $\lim_{w \downarrow 0} \mathcal{P}(w)$ decreases,
- The exponential tail becomes steeper.

These behaviors emerge naturally when considering the role of the fractions ρ_{n_c}. The first trend arises from a decrease in ρ_0, since only particles with $n_c = 0$ give a δ-like contribution to $\mathcal{P}(w)$. The second trend comes from a decrease in ρ_1: from Eqs. (2.3.2) and (2.3.3) it is clear that $\lim_{w \downarrow 0} \mathcal{P}(w) = \rho_1 \mathcal{P}_1(w)$. The changes in $\mathcal{P}(w)$ can thus be understood from an increasing number of contacts, which is what one would expect for a compressed system [27]. The fractions ρ_2 and ρ_3 will increase at the expense of ρ_0 and ρ_1. Also third trend, the steepening of the exponential tail, is directly related to the increase in $\langle n_c \rangle$ via Eq. (2.3.4).
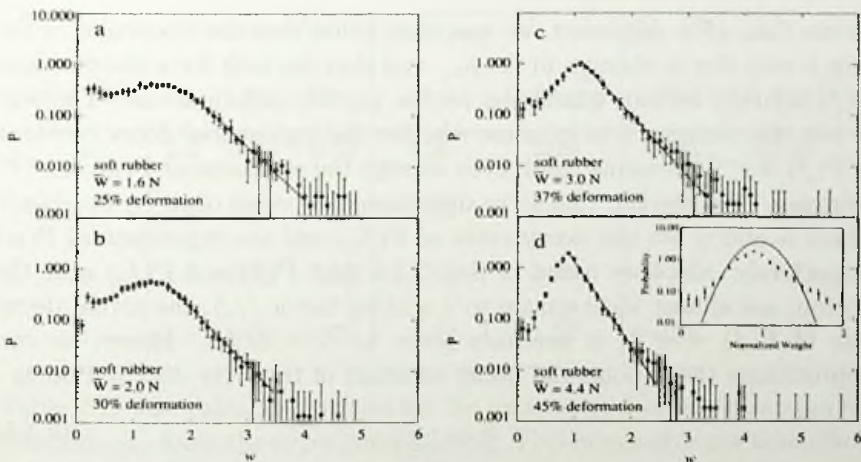
Figure 2.8: *(a)-(d)* The particle-wall force or weight distribution $\mathcal{P}(w)$ measured at the bottom boundary for increasing particle deformation. Both the δ-peak at $w = 0$ and $\lim_{w\downarrow0} \mathcal{P}(w)$ become smaller, and the exponential tail becomes steeper as the deformation increases. Taken from Erikson *et al.* [66]; in order to be consistent throughout this thesis, we adjusted the notation to $\mathcal{P}(w)$.

However, Eqs. (2.3.2)-(2.3.4) allow to further quantify this change in contact geometry from the experimental data. The value of $\rho_1\mathcal{P}_1(0)$ can be read off from the plots, after subtracting the δ-like data points, since $\rho_1\mathcal{P}_1(0) = \lim_{w\downarrow0}\mathcal{P}(w)$. The value of ρ_0 is obtained by the height of the δ-peak times the bin-width. Using the raw data of Fig. 2.8, we obtained the figures given in the first colomn of Table 2.1, where we took $\mathcal{P}_1(0) = 0.5$.[3] Unfortunately, the values of ρ_2 and ρ_3 can not be determined directly from the data.

An intriguing issue is that numerical simulations by Makse *et al.* [27] indicate that $P(f)$ crosses over to a Gaussian for large particle deformations. This contradicts the experimental data of Fig. 2.8, for which one observes an exponential tail even though particle deformations are up to

---

[3]To determine the precise value of $\mathcal{P}_1(0)$ is a very subtle problem. Since the total weight distribtution $\mathcal{P}(w)$ is normalized such that $\langle w \rangle = 1$, the average weight of particles with $n_c = 1$ will be smaller than unity. In principle, one can therefore not simply take the data of Fig. 2.6a to determine $\mathcal{P}_1(0)$, because these are scaled such that $\langle w \rangle = 1$; as an approximate guess we take $\mathcal{P}_1(0) = 0.5$.

no less than 45%. Moreover, we speculate below that the steepening of the tails is only due to changes in the ρ_{n_c}, and that the bulk force distributions $P(f)$ actually remain unaffected by the particle deformations. The way to test this scenario is to examine whether the exponential decay constant of $P(f) \propto e^{-\hat{\alpha}f}$ remains fixed, even though the steepness of $\mathcal{P}(w) \propto e^{-\gamma w}$ increases. We use Eq. (2.3.4) to determine the value of $\alpha\langle f_z \rangle = \gamma/\langle n_c \rangle$, where α and γ are the decay rates of $P(f_z)$ and the experimental $\mathcal{P}(w)$ respectively. Since we found in Sec. 2.2.3 that $P(f)$ and $P(f_z)$ near the bottom are almost identical up to a scaling factor $\langle f_z \rangle$, the actual decay rate of $P(f) \propto e^{-\hat{\alpha}f}$ is precisely given by $\hat{\alpha} = \alpha\langle f_z \rangle$. Hence, we can approximate the exponential decay constant of the force distribution as

$$\hat{\alpha} = \frac{\gamma}{\langle n_c \rangle} . \qquad (2.4.1)$$

To estimate the values of $\langle n_c \rangle$, we worked out two scenarios: we take either $\rho_2 = \rho_3$ or $\rho_3 = 0$. Together with the values of ρ_0, ρ_1 and γ, taken from the experimental data, this yields the values of $\hat{\alpha}$ listed in the second and third column of Table 2.1. Surprisingly, the root mean square deviation in $\hat{\alpha}$ is only 18%, which is not so much considering our rather crude estimates of the ρ_{n_c}, and the fact that Eq. (2.3.4) is only approximate.

Let us briefly recapitulate the discussion above. First, we have interpreted the data of Fig. 2.8 as a change in the packing geometry. To be more precise, the overall trends can be understood from the expected increase of the number of contacts due to compression. We demonstrated how one can determine the fractions ρ_0 and ρ_1 from the experimental data. Direct measurements of these fractions would be very welcome as a test of our framework, as well as to extract further information of the force distribution $P(f)$. Furthermore, our crude estimates in Table 2.1 give reason to believe that the force distribution $P(f)$ is actually not much affected by the compression. Finally, it seems that for most experimental results, where particle deformations are relatively small, ρ_0 and ρ_1 are substantial at the boundary, so that $\mathcal{P}_{boundary}(w)$ is similar to $P_{bulk}(f)$ (apart from a δ-peak at $w = 0$). The same argument probably holds for recent simulations by Silbert *et al.* [67].

2.5   Beyond the simple picture

In the picture that we have constructed above we characterize the packing geometry by the fractions ρ_{n_c}, and we found that the $\mathcal{P}_{n_c}(w)$ are very

Fig. 2.8	γ	ρ_0	ρ_1	$\rho_2 = \rho_3$		$\rho_3 = 0$	
				$\langle n_c \rangle$	$\hat{\alpha} = \frac{\gamma}{\langle n_c \rangle}$	$\langle n_c \rangle$	$\hat{\alpha} = \frac{\gamma}{\langle n_c \rangle}$
a.	2.4	0.23	0.58	1.05	2.29	0.96	2.51
b.	2.6	0.21	0.26	1.60	1.63	1.33	1.96
c.	2.8	0.14	0.18	1.88	1.49	1.54	1.81
d.	3.8	0.00	0.05	2.42	1.57	1.95	1.95

Table 2.1: The calculated values for the exponents $\hat{\alpha}$ after estimating the fractions ρ_{n_c} from the experimental data. The values of γ are taken from Table I of Ref. [66].

robust. This is of course a vast simplification, since we characterize the local environment of a particle by only one number, namely n_c. In this section we address the question why this crude approach works so remarkably well. For bottom particles the situation is particularly simple and insightful, since the geometry of the contacts is more or less fixed. There is one contact with the bottom, one or two almost horizontal intralayer contacts and n_c forces from above – see Fig. 2.2b. As we have shown in Fig. 2.3b, the angles of these forces display little scatter, so the local texture is more or less fixed once n_c is given. For bottom particles one can thus understand that n_c indeed provides a good description of the local packing geometry, which justifies the decompostion according to n_c. Although for particles in the bulk the situation is more complicated, there are similar arguments why $\mathcal{P}_{n_c}(w)$ is indeed a robust quantity, i.e. insensitive for packing geometry. These will be discussed in Sec. 2.5.1. We then address the up-down symmetry of the system. Our framework only involves the number of contacts from above, n_c, and not the number of contacts from below, $n_{\text{below}} = n_b$. For bottom particles n_c is the obvious parameter, but in the bulk of an amorphous packing, where the angle distribution is isotropic, there is no reason why n_c should be more important than n_b. In Sec. 2.5.2 we therefore investigate weight distributions for particles with a given combination $\{n_c, n_b\}$, which we denote by $\mathcal{P}_{n_c n_b}(w)$. Special attention will be paid to particles that have $n_c \neq n_b$ in Sec. 2.5.3.

2.5.1   Why is $\mathcal{P}_{n_c}(w)$ for bulk particles robust?

It is not a priori clear why $\mathcal{P}_{n_c}(w)$ is rather insensitive for the packing geometry, since the definition of $\mathcal{P}_{n_c}(w)$ in Eq. (2.3.1) involves the joint distribution of the $(\vec{f}_i)_z$ that push on a particle from above, i.e. $P\left((\vec{f}_1)_z, \cdots, (\vec{f}_{n_c})_z\right)$. This joint distribution has an explicit geometry dependence since the projections in the z-direction involve the distribution of contact angles φ_i. Even if we assume that the force *magnitude* is uncorrelated to its *orientation*, i.e.

$$P\left(\vec{f}_1, \cdots, \vec{f}_{n_c}\right) = P\left(f_1, \cdots, f_{n_c}\right) \Phi(\varphi_1, \cdots, \varphi_{n_c}) , \qquad (2.5.1)$$

we obtain the distribution of vertical components $P\left((\vec{f}_1)_z, \cdots, (\vec{f}_{n_c})_z\right)$ by integration over the joint angle distribution $\Phi(\varphi_1, \cdots, \varphi_{n_c})$. Therefore, the $\mathcal{P}_{n_c}(w)$ have an explicit geometry dependence.

We already saw that this angle distribution is more or less fixed for bottom particles. For the polydispersities used in this study, the bulk angles have also limited room for fluctuations once n_c has been specified. For example if $n_c = 3$, one typically finds one angle close to $\pi/2$ and two relatively small angles, see Fig. 2.9a; this is because the three particles should all touch the upper half of the bead supporting them. Particles with $n_c = 2$ also have such an 'excluded-volume'-like constraint (Fig. 2.9b), albeit less strong than for $n_c = 3$. Particles with $n_c = 1$ have an enhanced probability for angles around $\pi/2$, because such contacts make the presence of a second contact from above less probable (Fig. 2.9c). So, the shape of $\mathcal{P}_{n_c}(w)$ is limited by the geometric constraints on the angle distributions $\Phi(\varphi_1, \cdots, \varphi_{n_c})$. This justifies the picture that the geometry dependence of $\mathcal{P}(w)$ is mainly due to the ρ_{n_c}, and that the $\mathcal{P}_{n_c}(w)$ can be considered invariant.

Note that the abovementioned constraints on the angle distributions imply that the averages $\langle w \rangle_{n_c}$ are not simply proportional to n_c. Comparing for example $n_c = 1$ and $n_c = 3$, we see that the two 'extra' forces for $n_c = 3$ have a relatively small vertical component; the average weight will thus grow less than linearly with n_c. We should therefore correct Eq. (2.3.4) for the steepness of the tails by replacing $\langle n_c \rangle$ with $\sum_{n_c} \rho_{n_c} \langle w \rangle_{n_c}$. Making a correction of this type would further refine our analysis of the experiment with rubber beads discussed in Sec. 2.4.2.
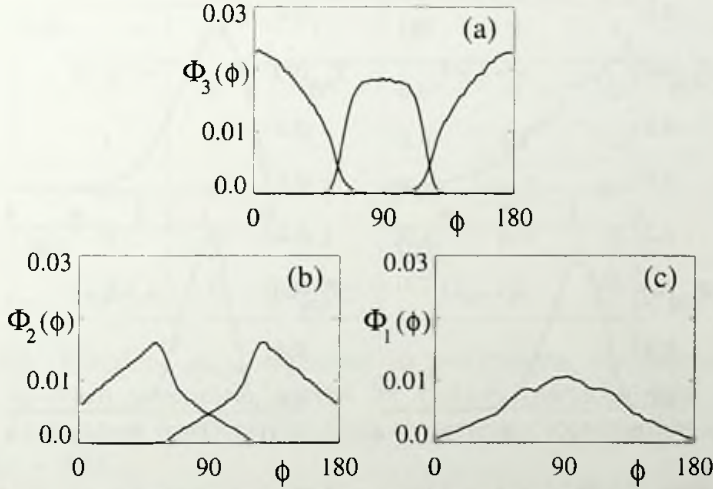
Figure 2.9: *(a)* For particles with $n_c = 3$, we plot the probability densities for the angles $\Phi_3(\varphi_1)$, $\Phi_3(\varphi_2)$ and $\Phi_3(\varphi_3)$, where the three angles have been sorted such that $\varphi_1 < \varphi_2 < \varphi_3$; *(b)* The probability densities $\Phi_2(\varphi_1)$ and $\Phi_2(\varphi_2)$ for particles with $n_c = 2$; *(c)* The probability density $\Phi_1(\varphi_1)$ for particles with $n_c = 1$.

2.5.2 Gravity and up-down symmetry

In our analysis of $\mathcal{P}(w)$ we have explicitly broken the up-down symmetry, since it only involved the number of contacts from above. At the bottom, this is an obvious choice. Away from the boundary, however, the amorphous packings have an isotropic angle distribution even though the packings were created under gravity. Moreover, we have neglected the term mg in Eq. (2.1.1), which makes the sum of forces from below equal to the sum of forces from above. So in principle one could also decompose $\mathcal{P}(w)$ according to the number of contacts from below n_b. We therefore investigate $\mathcal{P}_{n_c n_b}(w)$; this can be regarded as a 'component' of $\mathcal{P}_{n_c}(w)$, since $\rho_{n_c}\mathcal{P}_{n_c}(w) = \sum_{n_b} \rho_{n_c n_b}\mathcal{P}_{n_c n_b}(w)$.

Fig. 2.10b shows that $\mathcal{P}_{13}(w)$, $\mathcal{P}_{22}(w)$ and $\mathcal{P}_{31}(w)$ are almost identical. The same holds for $\mathcal{P}_{23}(w)$ and $\mathcal{P}_{32}(w)$ (Fig. 2.10c), so the total coordination number $n_c + n_b$ appears to be a more fundamental quantity than just n_c or n_b. Fig. 2.10d furthermore shows that the quadratic scaling of $\mathcal{P}_{33}(w)$ is somewhat more pronounced than for $\mathcal{P}_{23}(w)$ and $\mathcal{P}_{32}(w)$;
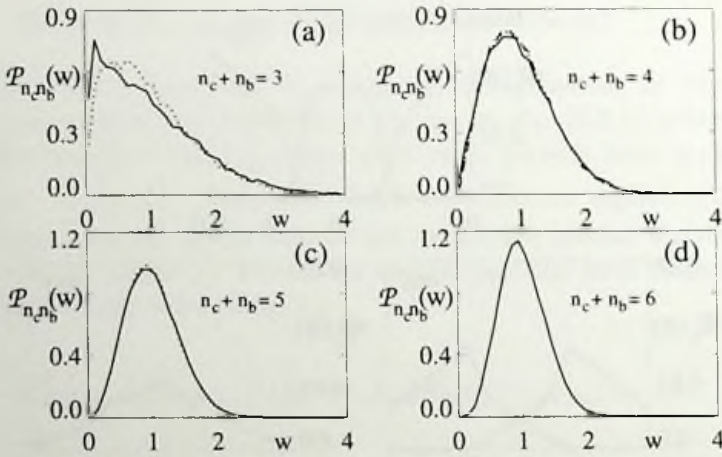
Figure 2.10: *(a)* $\mathcal{P}_{12}(w)$ (solid line) and $\mathcal{P}_{21}(w)$ (dotted line); *(b)* $\mathcal{P}_{13}(w)$, $\mathcal{P}_{22}(w)$ and $\mathcal{P}_{31}(w)$; *(c)* $\mathcal{P}_{23}(w)$ and $\mathcal{P}_{32}(w)$; *(d)* $\mathcal{P}_{33}(w)$.

it seems that the presence of 2 contacts from one side inhibits the pure quadratic scaling.

The presence of gravity is noticed, however, for $\mathcal{P}_{12}(w)$ and $\mathcal{P}_{21}(w)$ which do show some differences (Fig. 2.10a). These particles have only 3 contacts and were less restricted during the formation of the static force network by the 'cage' surrounding them. This allowed gravity to influence their final movements more than for particles with $n_c + n_b > 3$. Obviously, this effect is even stronger for particles with only 2 contacts, which typically have $\{n_c, n_b\} = \{0, 2\}$.

To further investigate the up-down symmetry, we list the fractions $\rho_{n_c n_b}$ of particles with a certain n_c and n_b in Table 2.2. For all particles with 3 or more contacts these fractions are almost perfectly symmetric. From this we conclude that in the amorphous packings, the up-down asymmetry due to gravity is only noticed by particles that have 2 or 3 contacts.

2.5.3   Particles with $n_c \neq n_b$

We have seen that for particles with $\{n_c, n_b\} = \{3, 1\}$ or vice versa, the small weight behavior is $\sim w^1$, which is different from the scaling predicted by Eq. (2.3.2). This breakdown of our simple picture can be understood as follows. A particle that has 4 contacts can either have $\{n_c, n_b\} =$

$n_c \setminus n_b$	0	1	2	3	4
0	0	0	0.6	0	0
1	0	0.3	5.6	4.7	0.2
2	0	4.7	26.1	20.5	0.7
3	0	5.1	21.6	8.9	0
4	0	0.3	0.7	0	0

Table 2.2: Fractions $\rho_{n_c n_b}$ expressed in percentages; the numbers are almost up-down symmetric, except for rattlers (particles with 2 contacts). From these fractions one finds the average coordination number $\langle n_c + n_b \rangle = 4.51$.

$\{3,1\}$, $\{n_c, n_b\} = \{2,2\}$ or $\{n_c, n_b\} = \{1,3\}$ depending on the precise orientations of the forces with respect to gravity. However, if we were to define the weights by projecting the $\vec{F}_{ij}$ at a small angle with respect to gravity, a particle with 4 contacts can easily change from $\{n_c, n_b\} = \{3,1\}$ to $\{2,2\}$ or even to $\{1,3\}$. However, we have seen that there is no 'preferred' projection direction, since gravity has only very little effect on our packings. Hence, it is not surprising that the $\mathcal{P}_{n_b n_c}(w)$ depend on $n_c + n_b$ and not on n_c or n_b individually.

But what determines the precise scaling for small weights? Consider a particle i with $n_c = 3$ and $n_b = 1$. The three forces pushing it from above, $\vec{F}_{i1}$, $\vec{F}_{i2}$ and $\vec{F}_{i3}$, are not independent: force equilibrium in the direction perpendicular to $\vec{F}_{i4}$ (the force pushing from below) requires $\left(\vec{F}_{i1} + \vec{F}_{i2} + \vec{F}_{i3} \right) \cdot \vec{n} = 0$, where $\vec{F}_{i4} \cdot \vec{n} = 0$. This reduces the number of independent forces from above to only 2, since the third is determined by mechanical equilibrium. As a consequence, the scaling behavior for small w will be $\mathcal{P}_{31}(w) \propto w$.

For particles with $n_c = 3$ and $n_b = 2$, the 5 forces are also coupled through mechanical equilibrium. In this case, however, one can not distil a relation between the forces from above only, such as we did for particles with $\{n_c, n_b\} = \{3,1\}$. So one still expects that $\mathcal{P}_{32}(w) \propto w^2$, as is observed in Fig. 2.10c. Nevertheless, this illustrates that two dimensional mechanical equilibrium *does* introduce correlations between all

forces pushing from above. This limits the validity of our arguments used in Sec. 2.3, for bulk particles. At the bottom our analysis is still valid: horizontal equilibrium can be accomplished by the forces between neighboring bottom particles (see Fig. 2.2b), so the forces from above can really be considered as independent.

2.5.4   Summary

In this section we have tried to address limitations of our simple geometrical framework. We have shown that the observation that $\mathcal{P}_{n_c}(w)$ is insensitive to the packing geometry originates from excluded-volume-like correlations between the angles at which forces press upon a bead (Fig. 2.9). This is the subtle underlying reason why our simple picture, where we characterize the local packing geometry by only one number n_c, is good enough to interpret experimental and numerical data. We have furthermore studied the effect of gravity by decomposing the weight distribution according to the number of particles from below (n_b) as well. We found that gravity breaks the up-down symmetry only mildly in our simulations; the distributions $\mathcal{P}_{n_c n_b}(w)$ depend on the coordination number $n_c + n_b$ rather than on n_c or n_b independently (Fig. 2.10). This further refines the analysis of the relation between packing geometry and force network statistics in the bulk of a packing; at the boundary, it is sufficient to consider only the number of contacts from above (n_c).

2.6   Weight and force distributions in the q-model: the role of connectivity.

In this section, we investigate to what extent the results obtained for the Hertzian sphere packings can be understood within the context of the q-model and generalizations thereof. Let us briefly recapitulate the definition of the model (see also Sec. 1.4.4). The particles are positioned on a regular lattice, and the particle weights are stochastically transmitted to the neighbors in the layer below. The weight on a particle i splits up into n_c fractions $q_{i,\alpha}$, and the total weight exerted on a particle j in the layer below then becomes

$$W_j = mg + \sum_\alpha q_{j-\alpha,\alpha} W_{j-\alpha} \; , \qquad (2.6.1)$$

where the term mg can be neglected at great depth. The fractions $q_{i,\alpha}$ obey the constraint

$$\sum_\alpha q_{i,\alpha} = 1 , \qquad (2.6.2)$$

which assures mechanical equilibrium in the vertical direction.

The most important result of the q-model is that for a uniform q-distribution, the weights become distributed as [30]

$$\mathcal{P}_{n_c}(w) = c \, w^{n_c - 1} \, e^{-n_c w} , \qquad (2.6.3)$$

where n_c is fixed for a given lattice, and c is a normalization constant. Note that these solutions have the same qualitative behavior as those found in our molecular dynamics simulations: for small weights $\mathcal{P}_{n_c}(w) \propto w^{n_c - 1}$, and the probability for large weights decays exponentially.

The q-model is thus an effective minimal model for the weights W. It is clear that the product of q and W has a natural interpretion as the vertical component of $\vec{F}_{ij}$. Since these interparticle forces are more fundamental than the weights, we investigate the statistics of the quantity qW in Sec. 2.6.1; this will shed new light on the small force behavior in the q-model. In the light of our finding that the contact geometry, and in particular n_c plays a crucial role, the standard q-model is clearly limited since it fixes n_c. In Sec. 2.6.2 we therefore extend the q-model to have randomness in its *connectivity* (i.e. to allow for a range of n_c's), and find that, as expected, the $\mathcal{P}(w)$ can be manipulated by changes in the connectivity.

2.6.1 Distribution of interparticle forces: $P(qw)$

A direct comparison of Eqs. (2.1.1) and (2.6.1) shows that the product qw has a natural interpretation as the vertical component of $\vec{f}_{ij}$. Since the interparticle forces are more important than the weights, it is interesting to investigate the statistical properties of the bond quantity qw. To obtain the distribution $P(qw)$, let us start with the transformation from $P(qw)$ to $\mathcal{P}_{n_c}(w)$:

$$\mathcal{P}_{n_c}(w) = \int_0^\infty d(qw)_1 P\left((qw)_1\right) \cdots \int_0^\infty d(qw)_{n_c} P\left((qw)_{n_c}\right)$$

$$\times \delta\left(w - \sum_{i=1}^{n_c} (qw)_i\right) . \qquad (2.6.4)$$

Here we assumed that the $(qw)_i$ are uncorrelated, which we show to be valid for the uniform q-distribution in Sec. 3.3. For the corresponding Laplace transforms, denoted by $\tilde{P}(s)$ and $\tilde{\mathcal{P}}_{n_c}(s)$ respectively, this relation becomes

$$\tilde{\mathcal{P}}_{n_c}(s) = \left(\tilde{P}(s)\right)^{n_c} , \qquad (2.6.5)$$

leading to the following solution:

$$\tilde{P}(s) = \frac{1}{1+s} \quad \Rightarrow \quad P(qw) = e^{-qw} . \qquad (2.6.6)$$

We thus find (for the uniform q-distribution) that $P(qw)$ is a pure exponential, independent of the number of contacts n_c. Again, this is very similar to the results for our Hertzian sphere packings: the distribution of 'interparticle forces' $P(qw)$ is finite for small forces, whereas the distribution of weights depends on n_c as given by Eq. (2.3.2). Moreover, this resolves the discrepancy for small forces mentioned in the preceding chapter: the q-model predicts a vanishing probability density for small weights, *but not* for small forces.

The question that arises is: how generic are these results, which have been derived for the uniform q-distribution? This can be answered by relating the properties of $P(qw)$ to those of the q-distribution $\eta(q)$. It is easy to show that the behavior for small qw and q respectively are identical:

$$\eta(q \to 0) \propto q^{\alpha} \quad \Rightarrow \quad P(qw \to 0) \propto (qw)^{\alpha} . \qquad (2.6.7)$$

So, as long as we take a finite probability density for $q = 0$, the qualitative behavior of $P(qw)$ and $\mathcal{P}_{n_c}(w)$ will be robust.

2.6.2   Including geometry effects

From Sec. 2.3, it is clear that the weight distribution $\mathcal{P}(w)$ in Hertzian sphere packings is very sensitive for the local packing geometry. Since the q-model is defined on a regular lattice, with fixed connectivity, it can not capture the behavior of $\mathcal{P}(w)$ in disordered packings with fluctuating n_c. This extra degree of disorder can be included, for example, by 'cutting' some of the bonds of the regular lattice. We illustrate this with the 2-dimensional square lattice depicted in Fig. 2.11a. For each site, the weight is transmitted downwards through either 2 or 3 bonds with probabilities p and $1 - p$ respectively; in the former case we randomly cut one of the available bonds and generate the two remaining q_{ij} according to a uniform
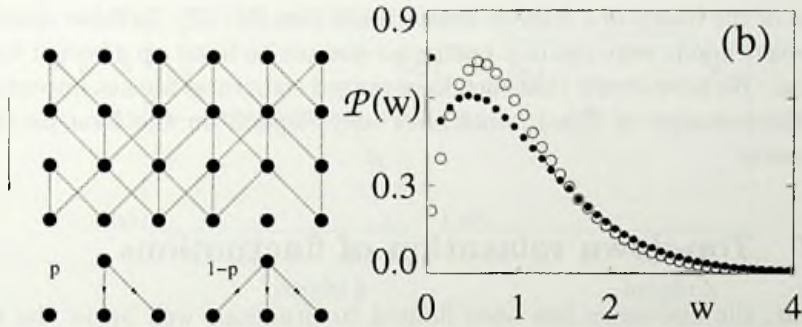
Figure 2.11: The q-model with a random connectivity: *(a)* with a probability p we cut one of the three bonds; *(b)* bottom effect in the q-model with random connectivity. In the bulk $p = 0.3$ (open circles) and at the bottom $p = 0.9$ (dots); this corresponds to $\{\rho_0, \rho_1, \rho_2, \rho_3\} = \{0.00, 0.03, 0.24, 0.73\}$ and $\{0.03, 0.19, 0.44, 0.34\}$ respectively.

distribution satisfying Eq. (2.6.2). This generates particles with $n_c = 0, 1, 2$ and 3, since all bonds *arriving* at a site have a probability of $p/3$ to be missing. For simplicity, we introduced the disorder in n_c by means of one parameter p only; as a consequence, we can only obtain a limited set of $\{\rho_{n_c}\}$.

With this model, we have tried to mimic the bulk-bottom behavior of $\mathcal{P}(w)$ that was observed in the amorphous packings (Fig. 2.5a). In the bulk layers we took out bonds with probability $p = 0.3$, and for the bottom layer we took $p = 0.9$; the result is shown in Fig. 2.11b. Indeed, the change in the fractions ρ_{n_c} is sufficient to reproduce a transition of $\mathcal{P}(w)$ reminiscent of what has been observed in our Hertzian sphere packings (compare with Fig. 2.5a).

2.6.3   Conclusions q-model

Although the q-model does not describe the spatial structure of the force-network, it remains a valuable theoretical framework for the *statistics* of force fluctuations. While in the standard case the disorder in the system is represented by the stochastic fractions $q_{i,\alpha}$ only, we have shown that when also the connectedness is chosen to be random, the model displays most features of realistic packings.

Let us conclude this section by mentioning that the idea to leave out

some of the bonds of a regular lattice is not new [61, 62]. In these studies, however, bonds were cut in a particular manner to build up directed force chains. We have shown that such long-ranged structures are not important for the behavior of $\mathcal{P}(w)$, since they only depend on the *local* packing geometry.

2.7   Top-down relaxation of fluctuations

So far, the discussion has been limited to situations well below the top surface of the packings. The data of the Hertzian sphere simulations were taken at least 15 layers below the top surface and the results of the q-model (presented in the previous section) all correspond to the limit of large depths. In this section we investigate the top-down relaxation of the force and weight distributions. At the top surface of the Hertzian sphere packings, there are only weight fluctuations due to grain polydispersity. The question we address is how fast the force and weight fluctuations build up towards a bulk distribution, as a function of depth.

These results can then be compared to the relaxation in the q-model. Interpreting the downward direction as time, this corresponds to transient behavior towards the 'stationary' solutions given in Eqs. (2.6.3) and (2.6.6). This top-down relaxation of fluctuations forms an additional test to qualify various theoretical models, very much like the Green's function measuring the response to a localized load on the top-surface. In our case, we start from spatially (nearly) homogeneous conditions in the top layer and see how fluctuations build up.

2.7.1   Top-down relaxation in Hertzian sphere packings

A good way to quantify changes in $\mathcal{P}(w)$ and $P(f)$ is to study their second moments $\langle w^2 \rangle$ and $\langle f^2 \rangle$. For a distribution of zero width these second moments are unity,[4] and they increase as the fluctuations become larger. In Fig. 2.12 we show the second moments as a function of the height h, which is defined as the distance from the bottom boundary. Since the packings are strongly disordered, the precise location of the top surface will be slightly different for each realization; it turns out to be located around $h = 46$.

---

[4]These second moments have been normalized by the first moments as $\langle w^2 \rangle = \langle W^2 \rangle / \langle W \rangle^2$ and $\langle f^2 \rangle = \langle F^2 \rangle / \langle F \rangle^2$ respectively.
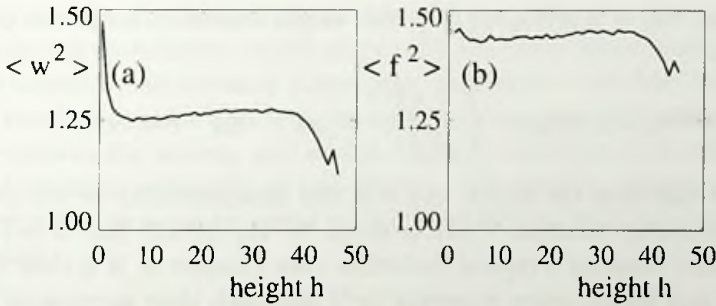
Figure 2.12: The second moments *(a)* $\langle w^2 \rangle$ and *(b)* $\langle f^2 \rangle$ as a function of height h in simulations of Hertzian sphere packings; the top surface is located around $h = 46$. Both for the forces and the weights one finds a fast top-down relaxation of the moments.

Let us first consider the broadening of the weight distribution shown in Fig. 2.12a. As already mentioned above, the weight fluctuations at the top surface are entirely due to polydispersity of the grains. Using a flat distribution between $0.4 < r < 0.6$ this corresponds to $\langle w^2 \rangle \approx 1.11$, which is consistent with our simulation data. The second moment approaches its bulk value already at a depth of approximately 10 particle diameters. The figure also shows the sharp transition of $\mathcal{P}(w)$ at the bottom boundary. The second moments of $P(f)$ are shown in Fig. 2.12b. One again observes a relaxation over approximately 10 layers, towards a bulk value; $P(f)$ does not change significantly near the bottom boundary. Note that both the force and weight distributions become slightly narrower as the depth increases. This may be attributed to an increase in particle deformations [27].

We thus find that the typical length scale for force and weight fluctuations to saturate is approximately 10 particle diameters. This provides another important criterion to distinguish between different theoretical models.

2.7.2 Comparison with relaxation in the q-model

In Chapter 4 we will solve the problem of top-down relaxation in the q-model in great detail. We now briefly summarize these results in order to make a comparison with the relaxation in the Hertzian sphere packings presented in the preceding paragraphs. Without the so-called *injection*

term, i.e. $mg = 0$ in Eq. (2.6.1), the weight distributions in the q-model relax as

$$\mathcal{P}^{(t)}(w) \simeq \mathcal{P}(w) + \left(\frac{1}{\sqrt{t}}\right)^{d-1} \mathcal{F}(w) \qquad \text{for} \quad t \to \infty , \qquad (2.7.1)$$

where t indicates the depth and d is the dimensionality of the packing. The stationary solution $\mathcal{P}(w)$ is given by Eq. (2.6.3) and $\mathcal{F}(w)$ is the (invariant) shape of a typical deviation – see Chapter 4. It is clear that all second and higher order moments $\langle w^k \rangle$ approach their asymptotic values according to the same power-law. We furthermore show in Chapter 4 that including the injection term mg alters the relaxation process as follows:

$$\mathcal{P}^{(t)}(w) - \mathcal{P}(w) \quad \propto \quad \mathcal{F}(w) \begin{cases} \dfrac{1}{\sqrt{t}} & , d = 2 \\[2ex] \dfrac{\log(t)}{t} & , d = 3 \\[2ex] \dfrac{1}{t} & , d \geq 4 . \end{cases} \qquad (2.7.2)$$

Note that since the downward q-values are statistically independent from the weights, the 'force' fluctuations simply follow from $\langle (qw)^2 \rangle = \langle q^2 \rangle \langle w^2 \rangle$, and thus display the same relaxation as the weights fluctuations.

The q-model thus predicts a power-law relaxation with a logarithmic correction for 3D packings, Eq. (2.7.2). However, we find no evidence for such a slow relaxation in our simulations of Hertzian spheres, which indicate that a bulk distribution is reached after approximately 10 layers of particles (Fig. 2.12). In the 2D q-model with injection, for example, the second moment after 10 layers still differs around 20% from its asymptotic value. Let us provide two possible explanations why the q-model fails to describe this relaxation process. A first problem of the model is that it assumes some fixed q-distribution $\eta(q)$: we have seen that the q's can in principle be derived from the forces as $q = \left(\vec{F}_{ij} \right)_z / W_i$, so a relaxation in $P(f)$ and $\mathcal{P}(w)$ should result into a relaxation of $\eta(q)$ itself. This clearly shows the difficulty of encoding the force behavior into a stochastic variable q in a self-consistent manner.

Another problem of the model is that it assumes a top-down propagation of forces. The up-down symmetry is therefore broken explicitly in the q-model; we find no evidence for this symmetry breaking in our Hertzian

sphere packings. In principle, force networks are defined by the equations of mechanical equilibrium, which generically are underdetermined and can not be solved by an iterative (top-down) procedure – see Sec. 1.4.1. Instead, one has to solve this set of coupled equations 'simultaneously' for all particles in the system, and except for the (small) mg term, there is a natural up-down symmetry in this system. The absence of this up-down symmetry in the q-model could of course strongly affect the top-down relaxation.

2.8 Discussion

In this chapter we have shown that it is crucial to distinguish between forces and weights, in order to understand the statistics of force networks. We have found in our simulations that the force distribution $P(f)$ is very robust, in the sense that its shape does not depend on details of packing geometry. Even for very regular geometries $P(f)$ has a wide exponential tail. The weight distribution $\mathcal{P}(w)$, on the other hand, is very sensitive for the local packing geometry. It turns out that a decomposition according to the number of contacts that press on a particle from above, n_c, is sufficient to understand this geometry dependence. Reinterpreting experiments on strongly deformed rubber particles within our framework, we have argued that $P(f)$ may actually be unaffected by these very large particle deformations.

The work presented in this chapter provokes a number of questions. First, we observe that most of our simulation results, like the shapes of $P(f_z)$ and $\mathcal{P}(w)$, can be understood in terms of *local* packing geometry only. This suggests that long-range correlations are not dominant, at least not for the 'one point' force, weight and angle probability distributions. We therefore question whether the transition of $P(f)$ observed at the jamming transition (Sec. 1.4.2) can reflect a long-range structural change of the force network. In particular, we expect that the role of 'force chains' can only be understood from two or more point correlation functions, and not from $P(f)$ only. We briefly come back to this issue at the end of Chapter 6.

A related problem is that the q-model fails to describe problems that involve spatial structure of the force network. The model is able to capture many features of force and weight statistics, as we have seen in Sec. 2.6. However, the model does not produce the top-down relaxation of $\mathcal{P}(w)$

that is observed in the more realistic Hertzian packings. Alongside with
the incorrect prediction of the response function, this indicates that spa-
tial dependence is not correctly incorporated within the q-model. This is
probably due to the fact that it is a *scalar* model in which one imposes
mechanical equilibrium in one direction only. Additionally, the recursive
nature of the q-model does not acknowledge the structure of the equa-
tions describing mechanical equilibrium. As we discussed in Chapter 1,
these equations are typically underdetermined and cannot be solved in a
recursive manner. We therefore propose a different theoretical approach
in Chapter 6, in which we start from the equations of mechanical stability
and exploit the undetermined degrees of freedom.

Another important issue for future study is clearly the role of friction
and dimensionality. Our numerical study has been done in two dimensions
with frictionless spheres; however, recent studies indicate [27] that the
coordination number for 3D packings with friction is similar to those of
2D frictionless packings. Qualitatively, the picture we have advanced is
therefore expected to capture the realistic case of three dimensions with
friction, because our phase space arguments are independent of dimension.

2.A   Logarithmic divergence of $P(f_z)$

In Sec. 2.2.3, we encounter the following integral:

$$
\begin{aligned}
P(f_z) &= \int_0^\pi d\varphi \, \frac{1}{\pi} \int_0^\infty df \, P'(f) \, \delta \left(f_z - f \sin(\varphi) \right) \\
&= \int_0^\infty df \, P'(f) \int_0^{\pi/2} d\varphi \, \frac{2}{\pi} \frac{1}{f} \delta \left(\frac{f_z}{f} - \sin(\varphi) \right) \\
&= \frac{2}{\pi} \int_{f_z}^\infty df \, \frac{1}{\sqrt{f^2 - f_z^2}} P'(f) \, .
\end{aligned}
\tag{2.A.1}
$$

The function $P'(f)$ represents the probability density function of $f = |\vec{f}|$,
which we can assume to be regular on the entire interval (see Fig. 2.2).
The behavior for small f_z is not trivial, since the integrand diverges at
the lower bound of the integration interval. For each non-zero f_z this does

not lead to a singularity, since

$$
\begin{aligned}
P(f_z) &= \frac{2}{\pi} \int_{f_z}^{\infty} \frac{df}{f_z} \frac{P'(f)}{\sqrt{(f/f_z)^2 - 1}} \\
&= \frac{2}{\pi} \int_1^{\infty} du \frac{P'(uf_z)}{\sqrt{u^2 - 1}} .
\end{aligned} \tag{2.A.2}
$$

The integral over $1/\sqrt{u^2 - 1}$ is convergent for $u \to 1$ and the function $P'(uf_z)$ falls of fast enough as $(uf_z) \to \infty$. For $f_z = 0$, however, the integral diverges as $u \to \infty$. To obtain the asymptotic behavior we rewrite the integral as

$$
\frac{2}{\pi} \int_1^{\infty} du \frac{P'(uf_z)}{u}
$$
$$
+ \frac{2}{\pi} \int_1^{\infty} du P'(uf_z) \left(\frac{1}{\sqrt{u^2 - 1}} - \frac{1}{u} \right) . \tag{2.A.3}
$$

The second term is convergent since the term between brackets behaves as $1/u^3$ in the limit $u \to \infty$. We thus find that

$$
\begin{aligned}
P(f_z \to 0) &\simeq \frac{2}{\pi} \int_{f_z}^{\infty} df \frac{P'(f)}{f} + \mathcal{O}(1) \\
&\simeq -\frac{2}{\pi} P'(0) \ln(f_z) + \mathcal{O}(1) .
\end{aligned} \tag{2.A.4}
$$

2.B   Relation between tails of $P(f_z)$ and $\mathcal{P}_{n_c}(w)$

In this appendix we derive the large weight behavior of $\mathcal{P}_{n_c}(w)$ from the tail of $P(f_z)$, assuming that the various $\left(\vec{f}_i\right)_z$ in Eq. (2.3.1) are uncorrelated. We consider both faster and slower than exponential decays of the form

$$
P(f_z) \propto e^{-\alpha f_z^\beta} \quad \text{for} \quad f_z \to \infty . \tag{2.B.1}
$$

We show that, after rescaling $\langle w \rangle$ to unity, this leads to

$$
\mathcal{P}_{n_c}(w) \propto e^{-\gamma w^\beta} , \tag{2.B.2}
$$

with

$$
\gamma = \begin{cases} \alpha \langle f_z \rangle^\beta n_c &, \beta \geq 1 \\[2mm] \alpha \langle f_z \rangle^\beta n_c^\beta &, \beta \leq 1 . \end{cases} \tag{2.B.3}
$$

This means that the tail of the weight distribution is of the same nature as that of the forces, but with a different prefactor γ. The tails get steeper for increasing n_c, since the reduced probability for small w (due to a lack of phase space) must be compensated to keep $\langle w \rangle = 1$.

The above results are obtained as follows. Rescaling all forces in Eq. (2.3.1) as $x_i = (f_z)_i / w$, one obtains the probability for large weights

$$\mathcal{P}_{n_c}(w) \propto w^{n_c-1} \int_S dx_1 \cdots dx_{n_c} \, e^{-\alpha w^\beta \left(x_1^\beta + \cdots + x_{n_c}^\beta\right)} , \qquad (2.B.4)$$

where S denotes the hyperplane $1 - \sum_i x_i$.

For $\beta > 1$, the probability density on S has a maximum at $x_i = 1/n_c$, which becomes sharply peaked for increasing w. Physically, this means that the dominant contribution for large weights will come from all f_z being equal, namely w/n_c. Approximating the integrand by a Gaussian around its maximum value, we find that the 'width' decreases as a power of w only, namely $1/w^{(n_c-1)\beta/2}$. Hence the leading behavior for large w is given by the maximum value of the integrand, i.e. $e^{-\alpha w^\beta/(n_c)^{\beta-1}}$.

For $\beta < 1$, the probability density has a minimum at $x_i = 1/n_c$, and the dominant contribution now comes from $x_i = 1$ and $x_{j \neq i} = 0$. This means that typically only one of the forces accounts for the whole weight. The part of the integral around $x_i = 1$ can be approximated by

$$e^{-\alpha w^\beta} \int_{S_\epsilon} dx_1 \cdots dx_{n_c} e^{-\alpha w^\beta \sum_{j \neq i} x_j^\beta} , \qquad (2.B.5)$$

where S_ϵ denotes the part of S for which $1 - x_i \leq \epsilon$. This approximation becomes exact for $w \to \infty$ as long as $w^\beta \epsilon \ll 1$; we take $\epsilon = 1/w^{1-\delta}$ with $0 < \delta < 1 - \beta$. Working out the integration over S_ϵ, one finds

$$\frac{e^{-\alpha w^\beta}}{w^{n_c-1}} \left(\int_0^\infty dy \, e^{-\alpha y^\beta} \right)^{n_c-1} , \qquad (2.B.6)$$

as $w \to \infty$. The part of the integral outside the areas S_ϵ is smaller than $w^{n_c-1} e^{-\alpha w^\beta (1+w^\delta)}$ and can thus be neglected. So also for $\beta < 1$, the leading behavior for large w is simply given by the maximum value, i.e. $e^{-\alpha w^\beta}$.

As mentioned in Sec. 2.3, the $\mathcal{P}_{n_c}(w)$ obtained by Eq. (2.3.1) are not properly normalized, since $\langle w \rangle = \langle f_z \rangle n_c$. If we rescale the average weight to unity, we obtain the results of Eqs. (2.B.2) and (2.B.3).

Stationary solutions and correlations in the q-model

3.1 Introduction

The discussion of the q-model in the previous chapters[1] has been limited to the uniform q-distribution, which serves as a generic example. One peculiarity of the uniform q-distribution is that all weights become totally uncorrelated at infinite depth [30], i.e. the joint weight distribution is simply a product of the $\mathcal{P}(w_i)$ of Eq. (1.4.4). Although it might seem obvious that a uniform distribution leads to an uncorrelated stationary state, this is really not trivial. Due to the constraint of Eq. (1.4.2), there are correlations between the $q_{i,\alpha}$ leaving each site, which in general gives rise to weight correlations.

In this chapter, we investigate under which special circumstances weight correlations dissappear in the q-model; we demonstrate that this is only the case for a special class of q-distributions. For all other q-distributions correlations persist, and we reveal the remarkable nature of these correlations. It is perhaps good to point out that we treat the various $q_{i,\alpha}$ equally, since there is no preferred horizontal direction a priori. We therefore consider symmetric q-distributions in this chapter; asymmetric distributions will be addressed in the context of the Asymmetric Random Average Process in Chapter 5.

---

[1] The model has been defined in Sec. 1.4.4. For convenience in notation, we will from now on use the symbol z instead of n_c to indicate the number of q-values per site.

3.2   Mathematical formulation

In this section we translate the recursion for the weights, Eq. (1.4.3), into a recursion for the weight distributions. We first have to deal with the fact that the average weight increases linearly with depth due to the *injection term*, which respresents the weight of a single particle. Labelling the top layer by $t = 0$, one has $\langle W \rangle^{(t)} = t + 1$. As usual, we rescale all weights to the average value at a given layer. For the rescaled weights w'_j in layer t, Eq. (1.4.3) becomes

$$w'_j = \frac{1}{t+1} + \frac{t}{t+1} \sum_\alpha q_{j-\alpha,\alpha} w_{j-\alpha} , \qquad (3.2.1)$$

which in the limit of infinite depth $t \to \infty$ reduces to

$$w'_j = \sum_\alpha q_{j-\alpha,\alpha} w_{j-\alpha} . \qquad (3.2.2)$$

Since we are interested in the properties of *stationary* weight distributions in the q-model, we can simply use Eq. (3.2.2): the recursion relation itself becomes only stationary as $t \to \infty$. Hence, the injection term has no effect on the stationary distributions of the rescaled weights. The injection term *does* affect the relaxation towards the stationary state; this will be addressed in detail in Chapter 4.

In terms of the (joint) distributions, the recursion can be written as [30]

$$\mathcal{P}'(\vec{w}') = \int H(\vec{q}) \, d\vec{q} \int \mathcal{P}(\vec{w}) \, d\vec{w}$$

$$\times \prod_j \delta \left(w'_j - \sum_\alpha q_{j-\alpha,\alpha} \, w_{j-\alpha} \right) , \qquad (3.2.3)$$

where we have introduced a vector notation for the weights in one layer $\vec{w} = (w_1, \cdots, w_N)$, and for the integrations we use the abbreviations

$$\int d\vec{w} = \prod_i \int_0^\infty dw_i , \qquad (3.2.4)$$

$$\int d\vec{q} = \prod_i \int d\vec{q}_i = \prod_i \prod_\alpha \int_0^1 dq_{i,\alpha} . \qquad (3.2.5)$$

The q-distribution $H(\vec{q})$ can be any probability density constrained by Eq. (1.4.2). It is often convenient to work with the Laplace transform of Eq. (3.2.3). Defining the Laplace transform as

$$\tilde{\mathcal{P}}(\vec{s}) = \int d\vec{w} \exp(-\vec{s} \cdot \vec{w}) \, \mathcal{P}(\vec{w}) \,, \qquad (3.2.6)$$

the recursion simplifies to [30]

$$\tilde{\mathcal{P}}'(\vec{s}) = \int H(\vec{q}) d\vec{q} \, \tilde{\mathcal{P}}(\vec{s}(\vec{q})) \,, \qquad (3.2.7)$$

with

$$s_i(\vec{q}) = \sum_\alpha q_{i,\alpha} \, s_{i+\alpha} \,. \qquad (3.2.8)$$

So, we have obtained an integral equation that describes the evolution of the joint weight distribution in the q-model. The two representations Eq. (3.2.3) and (3.2.7) are equivalent, and they will both be used, depending on the mathematical aspects of the problem. The main difficulty of these equations is that the integrals do not factorize, and as a consequence, the variables develop intricate correlations upon iteration.

3.3 Exact stationary solutions

3.3.1 q-distributions leading to product measures

Stationary weight distributions $\mathcal{P}^*(\vec{w})$ or $\tilde{\mathcal{P}}^*(\vec{s})$ can be obtained by finding fixed points of Eq. (3.2.3) or (3.2.7). This problem is greatly simplified if the solution $\mathcal{P}^*(\vec{w})$ factorizes into a product of single-site weight distributions $\mathcal{P}^*(w_i)$, which corresponds to a totally uncorrelated solution. In Section 3.7 we will show that this can only be the case if there are no correlations between q-values at different sites, i.e.

$$H(\vec{q}) = \prod_i \eta(\vec{q}_i)\delta\left(1 - \sum_\alpha q_{i,\alpha}\right) \,. \qquad (3.3.1)$$

So for this section, the question is: which $\eta(\vec{q}_i)$ lead to uncorrelated fixed points?

To answer this question, let us assume that such a fixed point exists, i.e.

$$\mathcal{P}^*(\vec{w}) = \prod_i \mathcal{P}^*(w_i) \qquad \text{or} \qquad \tilde{\mathcal{P}}^*(\vec{s}) = \prod_i \tilde{\mathcal{P}}^*(s_i) \,. \qquad (3.3.2)$$

Inserting this Ansatz into the Laplace representation of the recursion relation, Eq. (3.2.7), yields

$$
\tilde{\mathcal{P}}^*(\vec{s}) \;=\;
$$
$$
\prod_i \int \eta(\vec{q}_i)\, \delta\left(1 - \sum_\alpha q_{i,\alpha}\right) d\vec{q}_i\; \tilde{\mathcal{P}}^*\left(\sum_\alpha q_{i,\alpha} s_{i+\alpha}\right)
$$
$$
=\; \prod_i \tilde{\psi}(s_{i+\alpha_1}, \cdots, s_{i+\alpha_z}) \,, \tag{3.3.3}
$$

where the function $\tilde{\psi}(s_{i+\alpha_1}, \cdots, s_{i+\alpha_z})$ is the outcome of the integral over the $\vec{q}_i$. The arguments represent the z (previously n_c) sites that are connected to site i in the layer above. Integrating out all weights except those at the z sites connected to i means putting all $s_j = 0$ except the set $\{s_{i+\alpha}\}$:

$$
\tilde{\mathcal{P}}^*(0, \cdots, 0,\, s_{i+\alpha_1}, \cdots,\, s_{i+\alpha_z},\, 0, \cdots, 0) =
$$
$$
\tilde{\psi}(s_{i+\alpha_1}, \cdots, s_{i+\alpha_z}) \prod_\alpha \tilde{\psi}(s_{i+\alpha}, 0, \cdots)^{z-1} \,. \tag{3.3.4}
$$

This projection of the total weight distribution can only factorize if $\tilde{\psi}(s_{i+\alpha_1}, \cdots, s_{i+\alpha_z})$ is a product function as well, i.e.

$$
\tilde{\psi}(s_{i+\alpha_1}, \cdots, s_{i+\alpha_z}) = \prod_\alpha \tilde{\psi}(s_{i+\alpha}) \,. \tag{3.3.5}
$$

This thus forms a necessary condition for the existence of a stationary product measure solution. It is also a sufficient condition since one can construct the single-site $\tilde{\mathcal{P}}^*(s_j)$ from $\tilde{\psi}(s_j) = \tilde{\psi}(s_j, 0, 0, \cdots)$ as

$$
\tilde{\mathcal{P}}^*(s_j) = \left[\tilde{\psi}(s_j)\right]^z \,, \tag{3.3.6}
$$

which follows from a further projection of Eq. (3.3.4). This leads to the following criterion for factorization:

Given a q-distribution $\eta(\vec{q})$, one can construct a product measure fixed point if, and only if, there is a function $\tilde{\psi}(s)$ that satisfies the following condition:

$$
\int \eta(\vec{q}) \delta\left(1 - \sum_\alpha q_\alpha\right) d\vec{q} \left[\tilde{\psi}\left(\sum_\alpha q_\alpha s_\alpha\right)\right]^z = \prod_\alpha \tilde{\psi}(s_\alpha) \,. \tag{3.3.7}
$$

Here, we could omit the site index i, since our formulation depends only on z (the number of q-values per site) and not on the details of the lattice.

A direct comparison of Eq. (3.3.6) with Eq. (2.6.5) shows that $\tilde{\psi}(s)$ is nothing but the Laplace transform of the distribution of the bond quantities qw, which may be interpreted as *interparticle forces* – see Chapter 2. This connection allows for a nice physical interpretation of Eq. (3.3.7): even though the $q_{i,\alpha}$ leaving site i are strongly correlated (they have to add up to unity), the corresponding forces $q_{i,\alpha}w_i$ can become statistically independent. It is only when this miracle happens that the weight distribution becomes a product state.

Let us continue by identifying the $\eta(\vec{q})$ that lead to product measure solutions. There is a mathematical relation that is extremely important for this purpose [68]:

$$\prod_{\alpha} \frac{1}{(1+s_\alpha)^r} = \frac{\Gamma(zr)}{[\Gamma(r)]^z} \int d\vec{q}\, \delta\left(1 - \sum_{\alpha} q_\alpha\right)$$
$$\times \prod_{\alpha}(q_\alpha)^{r-1} \frac{1}{(1+\sum_{\alpha} q_\alpha s_\alpha)^{zr}} \ .$$

$$(3.3.8)$$

It holds for any real $r > 0$. From this relation, it is immediately clear that for all q-distributions of the type

$$\eta(\vec{q}) = \frac{\Gamma(zr)}{[\Gamma(r)]^z} \prod_{\alpha}(q_\alpha)^{r-1} \ , \qquad r > 0 \qquad (3.3.9)$$

there is a $\tilde{\psi}(s)$ that obeys Eq. (3.3.7), namely

$$\tilde{\psi}(s) = \frac{1}{(1+s)^r} \ . \qquad (3.3.10)$$

The corresponding single-site weight distributions are

$$\tilde{\mathcal{P}}^*(s) = \frac{1}{(1+s/zr)^{zr}} \quad \text{or} \quad \mathcal{P}^*(w) = \frac{(zr)^{zr}}{\Gamma(zr)}\, w^{zr-1} e^{-zrw} \ . \qquad (3.3.11)$$

We rescaled the Laplace variable s, in order to put $\langle w \rangle = 1$. Coppersmith *et al.* already found these q-distributions for integer values of r, also based on Eq. (3.3.8) [30]. However, it holds for any real $r > 0$. This means that the set for which the stationary weight distribution factorizes

is substantially larger; it ranges from the infinitely sharp distribution ($r \to \infty$) to the so-called 'critical' distribution ($r \to 0$).[2] Note that one recovers the results for the uniform distribution, including the purely exponential $P(qw)$, by putting $r = 1$.

3.3.2   Other q-distributions

Although there is a huge variety of q-distributions that lead to uncorrelated weight distributions, in general one cannot find a $\tilde{\psi}(s)$ that obeys Eq. (3.3.7). We will prove this by making a Taylor expansion of $\tilde{\psi}(s)$

$$\tilde{\psi}(s) = \sum_{n=0}^{\infty} \psi_n \, s^n \, , \tag{3.3.12}$$

and then try to solve for the coefficients ψ_n by imposing Eq. (3.3.7). It turns out that the equations can only be solved under special conditions, which are precisely obeyed by the class of q-distributions given by Eq. (3.3.9).

Let us first focus on the left hand side (LHS) of Eq. (3.3.7). The Taylor expansion will give rise to terms of the type $(q_1 s_1)^{n_1} (q_2 s_2)^{n_2} \cdots (q_z s_z)^{n_z}$, which have to be integrated over all q_α. This leads to terms $s_1^{n_1} s_2^{n_2} ... s_z^{n_z}$ with prefactors given by the *moments* of $\eta(\vec{q})$

$$\overline{q_1^{n_1} q_2^{n_2} ... q_z^{n_z}} = \int \eta(\vec{q}) \delta \left(1 - \sum_\alpha q_\alpha \right) d\vec{q} \, q_1^{n_1} q_2^{n_2} ... q_z^{n_z} \, . \tag{3.3.13}$$

These moments are not independent, due to the constraint Eq. (1.4.2). In appendix 3.A, we show that the moments

$$\eta_n = \int \eta(\vec{q}) \delta \left(1 - \sum_\alpha q_\alpha \right) d\vec{q} \, q_1^n \, , \tag{3.3.14}$$

are in fact sufficient to characterize all relevant moments of Eq. (3.3.13). Besides the moments, there are of course additional prefactors consisting of combinations of the ψ_n; these are the quantities we try to find, for a given q-distribution $\eta(\vec{q})$.

---

[2] The critical distribution generates only $q = 0$ and 1, leading to algebraically decaying weight distributions [30, 69, 70]. The limit $r \to 0$ is a route towards the critical distribution because the q-values become increasingly concentrated around 0 and 1. The corresponding weight distributions approach $1/w$ with a cut-off for large weights.

The right hand side (RHS) of Eq. (3.3.7) also produces terms of the form $s_1^{n_1} s_2^{n_2} \cdots s_z^{n_z}$, with prefactors $\psi_{n_1} \psi_{n_2} \cdots \psi_{n_z}$. The remaining task is to equate the prefactors of the terms $s_1^{n_1} s_2^{n_2} \cdots s_z^{n_z}$ on both sides of the equation. This gives a set of equations, from which one can try to solve for the ψ_n.

The zeroth order equation is trivially obeyed for any ψ_0, as can be seen by putting all $s_\alpha = 0$. For convenience we fix $\psi_0 = 1$. The same happens at first order, since for each α, the LHS contains z terms $\psi_1 \overline{q_\alpha} s_\alpha = 1/z \, \psi_1 s_\alpha$, and the RHS is simply $\psi_1 s_\alpha$. The first non-trivial equation appears at second order. There are two equations, for s_α^2 and for $s_\alpha s_{\alpha'}$ where $\alpha \neq \alpha'$:

$$
\begin{cases}
\left(z\psi_2 + \dfrac{z(z-1)}{2}\psi_1^2 \right) \eta_2 = \psi_2 \\[4mm]
\left(z\psi_2 + \dfrac{z(z-1)}{2}\psi_1^2 \right) \dfrac{2(1 - z\eta_2)}{z(z-1)} = \psi_1^2 .
\end{cases}
\tag{3.3.15}
$$

Due to the constraint $\sum_\alpha q_{i,\alpha} = 1$, one can obtain an identity by multiplying the first equation by z, and adding it to the second equation multiplied by $z(z-1)/2$. Hence, the two equations are not independent and ψ_2 can be solved. The value of ψ_2 depends only on η_2, the second moment of the q-distribution.[3]

Working out the combinatorics of the higher orders, one finds the following general mathematical structure:

- At the nth order, there are as many equations as there are different partitions $\{n_1, n_2, \cdots, n_z\}$ that make $\sum_\alpha n_\alpha = n$. Permutations should not be considered as different because $\eta(\vec{q})$ is symmetric in its arguments.

- One of these equations is dependent, as one can obtain an identity by adding the equations, after multiplication by appropriate factors.

For $z = 2$, there are two third order equations, corresponding to the partitions $\{3, 0\}$ and $\{2, 1\}$, of which only one is independent. This means that ψ_3 can be solved as a function of η_2 (in appendix 3.A we show that η_3 depends on η_2, for $z = 2$). We run into problems at fourth order, where we have three partitions $\{4, 0\}$, $\{3, 1\}$ and $\{2, 2\}$, and hence two a

---

[3] The remaining equation for ψ_2 cannot be solved if $\eta_2 = 1/z$, i.e. for the critical q-distribution. As the corresponding weight distribution has diverging moments, one cannot even Taylor expand $\tilde{\mathcal{P}}^*(s)$ and $\tilde{\psi}(s)$.

priori independent equations for one coefficient ψ_4. It turns out that the remaining equations are only identical if there is a relation between η_4 and η_2, namely

$$\eta_4 = \frac{30\eta_2^2 - 11\eta_2 + 1}{16\eta_2 - 2} \, . \tag{3.3.16}$$

In appendix 3.A, it is shown that this relation is precisely obeyed by the class of q- distributions Eq. (3.3.9) for which $\tilde{\psi}(s)$ was already solved.

The fact that the expansion of $\tilde{\psi}(s) = [\tilde{\mathcal{P}}^*(s)]^{1/z}$ only fails at fourth order implies that a mean field approximation, in which one explicitly assumes a product state, does give the exact results up to the third moment of $\mathcal{P}^*(w)$. This is precisely the reason why the mean field solution $\mathcal{P}^{\mathrm{mf}}(w)$ differs only marginally from the real solution. To be more precise, the deviation $\mathcal{P}^{\mathrm{mf}}(w) - \mathcal{P}^*(w)$ should change sign 4 times, since it does not affect all moments lower than $\langle w^4 \rangle$. A careful inspection of the numerical results in [30] for a q-distribution in which $q = 0.1$ or $q = 0.9$ shows that these small 'wiggles' are indeed present. To magnify this effect, we show our simulation data in Fig. 3.1.
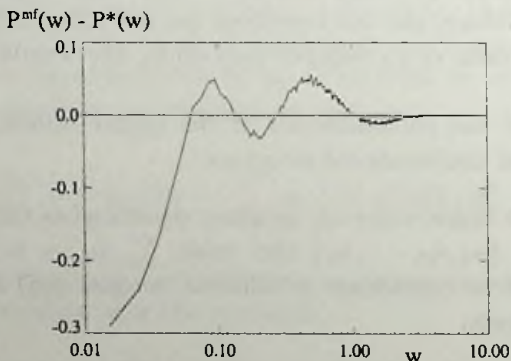
Figure 3.1: Numerical simulation of a q-distribution with $q = 0.1$ or $q = 0.9$. The small deviation $\mathcal{P}^{\mathrm{mf}}(w) - \mathcal{P}^*(w)$ changes sign 4 times.

For $z = 3$, the problems already appear at third order. Since we have the partitions $\{3, 0, 0\}$, $\{2, 1, 0\}$ and $\{1, 1, 1\}$, we encounter two independent equations for ψ_3. Again, it turns out that the equations can be solved if there is an additional relation between the q-moments:

$$\eta_3 = \frac{15\eta_2^2 - \eta_2}{9\eta_2 + 1} \, . \tag{3.3.17}$$

For $z > 3$, there are two independent third order equations as well, originating from $\{3,0,0,0,\cdots\}$, $\{2,1,0,0,\cdots\}$ and $\{1,1,1,0,\cdots\}$. This problem can always be overcome by assuming a particular relation between the moments η_3 and η_2, corresponding to the special q-distributions of Eq. (3.3.9). Since at higher orders the number of equations per coefficient ψ_n becomes increasingly high, there will most probably be no other q-distributions than those of Eq. (3.3.9) that obey Eq. (3.3.7), and thus have an uncorrelated weight distribution.

Let us conclude this section with two technical remarks. Firstly, the Ansatz of Eq. (3.3.2) is homogeneous in the site index i. The reason for this is that any intial spatial inhomogeneities are washed out by the relaxation process (see Chapter 4). The second remark concerns a calculation which has been performed for the Asymmetric Random Average Process (ARAP) by Zielen and Schadschneider [71]. This model can be mapped onto the q-model with a triangular packing. For the case $z = 2$ it has been shown that Eq. (3.A.8) is a *necessary* condition on the moments η_n for a product solution to exist. This nicely complements our calculations for $z = 2$, where we have shown Eq. (3.A.8) to be sufficient for all n, and to be necessary up to $n = 4$. We return to the ARAP in more detail in Chapter 5.

3.4 Master Equation for the moments of $\mathcal{P}(\vec{w})$

Now that we know that, in general, correlations do exist in the stationary weight distributions, it is interesting to study the nature of these correlations. In this section, we write the evolution of the moments as master equations. With this formalism we will, in the following sections, analyze the correlations by finding the stationary states of these master equations.

First, let us define the second moments of a distribution as

$$M_2(k) = \langle w_i w_{i+k} \rangle = \int d\vec{w} \, w_i w_{i+k} \, \mathcal{P}(\vec{w}) \, . \qquad (3.4.1)$$

We have reintroduced the site-index i, and k is a displacement-vector in a layer. As the system is translationally invariant, these second moments depend only on the displacement k. The recursion for these moments is obtained by combining Eq. (3.2.2) and Eq. (3.2.3) as

$$M_2'(k) = \sum_{\alpha,\alpha'} \left(\int H(\vec{q}) \, d\vec{q} \, q_{j,\alpha} \, q_{j+k+\alpha-\alpha',\alpha'} \right) M_2(k + \alpha - \alpha') \, . \qquad (3.4.2)$$

Using the overline notation for the q-averages as defined in Eq. (3.3.13), the recursion of Eq. (3.4.2) becomes

$$M_2'(k) = \sum_{\alpha, \alpha'} \overline{q_{j,\alpha} \, q_{j+k+\alpha-\alpha',\alpha'}} \, M_2(k + \alpha - \alpha') . \qquad (3.4.3)$$

This relation reveals from which points (in correlation-space) the moment $M_2'(k)$ receives a contribution during a recursion step. The reason why these second moments do not couple to the first moments or to higher moments is that the recursion for the weights, Eq. (3.2.2), is a linear equation.

Subtracting $M_2(k)$ from both sides of Eq. (3.4.3) leads to a master equation type formulation:

$$M_2'(k) - M_2(k) =$$
$$\sum_{\gamma} \Omega_\gamma(k - \gamma) \, M_2(k - \gamma) - \Omega_{-\gamma}(k) \, M_2(k) , \qquad (3.4.4)$$

where the terms on the right hand side can be interpreted as gain and loss terms respectively. The *transition rates* in this equation are defined as

$$\Omega_\gamma(k) = \overline{q_{i,\alpha} q_{i+k,\alpha'}} , \qquad (3.4.5)$$

with γ determined by the set α, α' as

$$\gamma = \alpha' - \alpha , \qquad (3.4.6)$$

and thus

$$\sum_{\gamma} = \sum_{\alpha, \alpha'} . \qquad (3.4.7)$$

Furthermore, to arrive at Eq. (3.4.4) we used the conservation property $\sum_\gamma \Omega_\gamma(k) = 1$, which originates from $\sum_\alpha q_{i,\alpha} = 1$.

In the current problem, where we consider second order moments, the transition rates are particularly simple. If $k \neq 0$, the q-averages are independent, and will always give the value $1/z^2$ (this only holds for q-distributions of the type Eq. (3.3.1)). If $k = 0$, one encounters second moments of $\eta(\vec{q})$, as in Eq. (3.3.13). This leads to the following transition rates:

$$k = 0 \quad \Rightarrow \quad \Omega_0(0) = \eta_2 \qquad \Omega_{\gamma \neq 0}(0) = \frac{1 - z\eta_2}{z(z - 1)},$$

$$k \neq 0 \quad \Rightarrow \quad \Omega_\gamma(k) = \frac{1}{z^2} . \qquad (3.4.8)$$

So, the moments evolve in an anomalous diffusion process, with differing transition-rates at the origin. A detailed discussion of the corresponding dynamics will be given in Chapter 4. Note that this diffusion takes place in a $d-1$ dimensional space, as α, and therefore also γ, is a displacement in a layer. In the remainder of this paper we use the bold notation $\boldsymbol{\gamma}$ whenever the displacement is really a vector.

The advantage of this somewhat formal representation is that we can take it over to higher order moments without further ado. The generalization of the master equation for the nth order moments $M_n(\mathbf{r})$ becomes:

$$M_n'(\mathbf{r}) - M_n(\mathbf{r}) =$$
$$\sum_{\gamma} \Omega_{\gamma}(\mathbf{r}-\boldsymbol{\gamma})\, M_n(\mathbf{r}-\boldsymbol{\gamma}) - \Omega_{-\gamma}(\mathbf{r})\, M_n(\mathbf{r}) \,, \qquad (3.4.9)$$

with the position indices $\mathbf{r} = (k_1, k_2, \cdots, k_{n-1})$, and the displacements $\boldsymbol{\gamma}$ defined as

$$\boldsymbol{\gamma} = (\alpha_1 - \alpha, \alpha_2 - \alpha, \cdots, \alpha_{n-1} - \alpha) \,. \qquad (3.4.10)$$

The dimensionality of the diffusion process has now become $(n-1)(d-1)$. The transition rates are defined as

$$\Omega_{\gamma}(\mathbf{r}) = \overline{q_{i,\alpha} q_{i+k_1,\alpha_1} \cdots q_{i+k_{n-1},\alpha_{n-1}}} \,. \qquad (3.4.11)$$

Analogous to the second moments, these transition rates are all $1/z^n$, as long as the indices of the position vector $\mathbf{r}$ are not equal to zero nor coincide. However, the differing rates make the problem complicated, because one has to deal with different transition rates at special points, lines, planes etc. in the space of diffusion.

3.5   Detailed balance

One can now study the correlations at infinite depth by finding stationary states of the master equation for the moments. As a first attempt to construct a stationary solution, i.e. $M_n'(\mathbf{r}) - M_n(\mathbf{r}) = 0$, one can try a detailed balance solution. Detailed balance means that there is no flow of 'probability' from one point to another. In that case, all terms of the sum on the right hand side of Eq. (3.4.9) vanish individually, i.e.

$$\Omega_{-\gamma}(\mathbf{r})\, M_n(\mathbf{r}) = \Omega_{\gamma}(\mathbf{r}-\boldsymbol{\gamma}) M_n(\mathbf{r}-\boldsymbol{\gamma}) \quad \text{for} \quad \text{all} \quad \mathbf{r}, \boldsymbol{\gamma} \,. \qquad (3.5.1)$$

This condition can also be formulated in terms of *elementary loops*, which are the smallest possible pathways from a point to itself. For all lattices in this study these elementary loops are triangles, as depicted schematically in Fig. 3.2; we denoted the three jump rates as (a, b, c) or (a', b', c') depending on the direction in which the loop is traversed. The three detailed balance conditions in this loop read

$$a\,A = a'B\,, \tag{3.5.2}$$
$$b\,B = b'C\,, \tag{3.5.3}$$
$$c\,C = c'A\,. \tag{3.5.4}$$

Taking the product of these three equations, one finds the property

$$abc = a'b'c' \tag{3.5.5}$$

as a necessary condition in *all* elementary loops in order to have a (global) detailed balance solution. It is easily shown that Eq. (3.5.5) is also a sufficient condition to have a nontrivial solution of the set of equations Eqs. (3.5.2)-(3.5.4). In the next section we show that correlations appear whenever these detailed balance conditions are not obeyed.

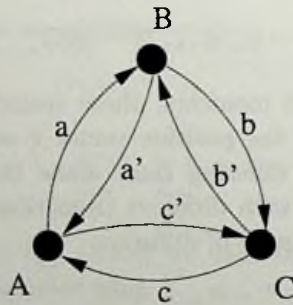

Figure 3.2: The transition rates (a, b, c) and (a', b', c') in an elementary loop $ABCA$.

3.6   Higher order correlations

In this section, we study the nature of the correlations for q-distributions of the type Eq. (3.3.1) that do not fall into the special class of Eq. (3.3.9). We first solve the stationary master equation for the second order moments,

for which we already know that there are no correlations (section 3.3). For the triangular packing ($z = 2$), correlations only show up at fourth order, and these fall off as $1/r^5$. For $z \geq 3$, there are third order correlations that also decay with a power law; for the fcc packing ($z = 3$) the decay is $1/r^4$. Finally, we provide a simple relation to calculate the various exponents.

3.6.1   Second order moments: no correlations

In order to get familiar with the structure of the master equations, we first consider the second order moments desribed by Eq. (3.4.4). As we show below, in this case it is possible to construct a simple detailed balance solution.

Away from the origin $k = 0$, all transition rates of Eq. (3.4.8) are identical. Therefore, the detailed balance condition Eq. (3.5.1) requires all $M_2(k \neq 0)$ to be identical. The value at the origin $M_2(0)$ has to obey a detailed balance condition for each $\gamma \neq 0$, but these equations are identical for all γ because the corresponding rates are the same. Putting $M_2(k \neq 0) = 1$, one obtains the following stationary solution:

$$\langle w_i w_{i+k} \rangle = \begin{cases} \dfrac{z-1}{z(1 - z\eta_2)} & , k = 0 \\ 1 & , k \neq 0 \,. \end{cases} \tag{3.6.1}$$

This solution precisely describes an asymptotic state without any second order correlations, as the average of the product $\langle w_i w_j \rangle$ equals the product of the averages for all $i \neq j$. This result was also derived by Lewandowska *et al.* [70], for the specific case of $z = 2$. However, any multiple of Eq. (3.6.1) also forms a stationary solution of the master equation; it will be shown in Chapter 4 that these solutions are physically irrelevant in the thermodynamic limit, where the lattice size $\to \infty$. Finally, we find that the second moment of the single-site distribution is solely determined by z and η_2. For critical q-distributions one has $\eta_2 = 1/z$, leading to a diverging second moment.

3.6.2   Third order moments

The diffusion of third order moments $\langle w_i w_{i+k} w_{i+l} \rangle$ takes place on a $2(d-1)$-dimensional lattice, since there are two free parameters k and l of dimension $d - 1$. On this lattice, there are three *special subspaces*, namely $k = 0$, $l = 0$, and $k = l$, for which the transition rates of Eq. (3.4.11) differ

from the *bulk*-value $1/z^3$. Moreover, the rates at the origin $k = l = 0$ differ from both the bulk-rates and the rates on the special subspaces.

Let us first consider the triangular packing ($z = 2$), for which the third order moments diffuse on a 2-dimensional lattice, with differing rates on three special lines. As these lines are all equivalent, it is natural to draw them at an angle of 120°, see Fig. 3.3. We then obtain a triangular lattice, with transitions to six nearest neighbors and two *self jumps*, which are 'transitions' to the same lattice site ($\gamma = 0$). The detailed balance condition between a special line and the bulk is naturally identical to the second order condition, implying the same ratio as in Eq. (3.6.1). As the transition rates at the origin are again identical for each $\gamma \neq 0$ (because of symmetry), one can construct the following detailed balance solution:

$$\langle w_i w_{i+k} w_{i+l} \rangle = \begin{cases} \dfrac{\eta_2}{(1 - 2\eta_2)^2} & \text{, origin} \\ \dfrac{1}{2(1 - 2\eta_2)} & \text{, lines} \\ 1 & \text{, bulk .} \end{cases} \qquad (3.6.2)$$

This means that there are also no third order correlations for $z = 2$: at the origin we encounter $\langle w^3 \rangle$, on the lines we have $\langle w_i^2 w_{i+k} \rangle = \langle w^2 \rangle \langle w \rangle$, and in the bulk $\langle w_i w_{i+k} w_{i+l} \rangle = \langle w \rangle^3$. It is easily checked that condition Eq. (3.5.5) is indeed satisfied in every elementary loop.

For the fcc packing ($z = 3$), the third order moments diffuse on a 4-dimensional lattice. Unlike the $z = 2$ packing, it is not possible to construct a detailed balance solution in this case. First, we write the displacement vectors as $\gamma = (\alpha' - \alpha, \alpha'' - \alpha) = (\gamma_1, \gamma_2)$, where the α's and γ's are 2-dimensional vectors (Fig. 1.9). One can jump away from the origin with two different rates, namely $\overline{q_1^2 q_2}$ and $\overline{q_1 q_2 q_3}$. These rates correspond to $\gamma_1 = \gamma_2$ (towards a special plane) and $\gamma_1 \neq \gamma_2$ (into the bulk) respectively. Checking the detailed balance condition in the elementary triangle *origin-plane-bulk-origin*, it turns out that Eq. (3.5.5) is only obeyed if η_3 and η_2 are related as in Eq. (3.3.17). Of course, this is precisely the case for the class of Eq. (3.3.9) for which we know that factorization occurs. In general, however, it is not possible to construct a detailed balance solution for the third order moments. In the next paragraph, we show that the absence of detailed balance indicates that there are weight-correlations, that decay with a power law; in this case the decay is $1/r^4$.
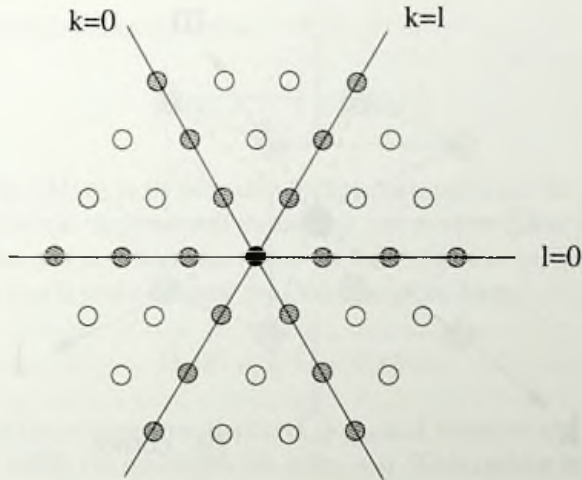
Figure 3.3: Triangular packing: third order moments diffuse on a triangular lattice.

3.6.3   Fourth order moments

The fourth order moments $\langle w_i w_{i+k} w_{i+l} w_{i+m} \rangle$ of the triangular packing diffuse on the bcc lattice depicted in Fig. 3.4. The three directions k, l, m precisely define a bcc primitive cell [72]. There are now differing rates at the origin as well as on lines and planes, for which one or more indices coincide or are equal to zero. The precise geometrical structure is explained in appendix 3.B. There are now two a priori different directions away from the origin, that is to *corners* $\langle w_i^3 w_{i+1} \rangle$ and to *body centers* $\langle w_i^2 w_{i+1}^2 \rangle$. Checking the loop condition Eq. (3.5.5) for the loop *origin-corner-body center-origin*, one finds that it is only satisfied when η_4 and η_2 are related as in Eq. (3.3.16).

The question that emerges is: What are the stationary solutions of the master equation, when the detailed balance condition is frustrated at the origin? To answer this question we first consider a simplified version of the bcc-problem, as a first order approximation. In this simple version, we assume that all jump rates are $1/z^4 = 1/16$, except at the origin where we distinguish between the two different directions. Although we neglect the differing rates on the special lines and planes, the loop condition is still frustrated in the elementary loop *origin-corner-body center-origin*. Using
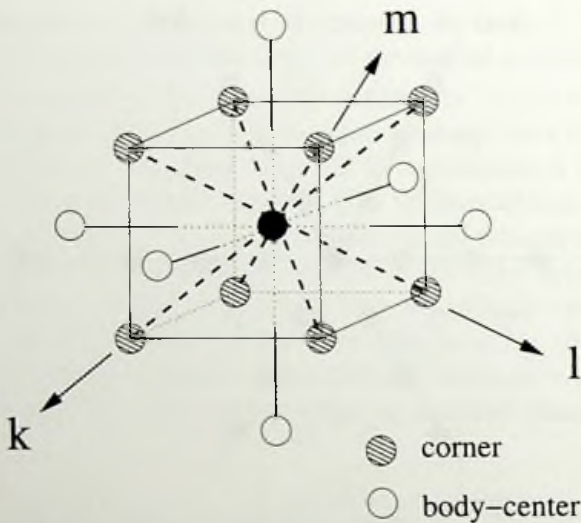
Figure 3.4: Triangular packing: fourth order moments diffuse on a bcc lattice.

$\sum_\gamma \Omega_\gamma(\mathbf{r}) = 1$, we write the stationary master equation as

$$M(\mathbf{r}) = \sum_\gamma \Omega_\gamma(\mathbf{r} - \gamma)M(\mathbf{r} - \gamma), \tag{3.6.3}$$

or

$$[1 - 2\Omega_0(\mathbf{r})]\,M(\mathbf{r}) = \sum_{\gamma \neq 0} \Omega_\gamma(\mathbf{r} - \gamma)M(\mathbf{r} - \gamma)\,. \tag{3.6.4}$$

This allows us to eliminate the two *self rates* Ω_0 by means of a simple transformation:

$$\begin{aligned}
\hat{M}(\mathbf{r}) &= [1 - 2\Omega_0(\mathbf{r})]\,M(\mathbf{r}), \\
\hat{\Omega}_\gamma(\mathbf{r}) &= \Omega_\gamma(\mathbf{r})/[1 - 2\Omega_0(\mathbf{r})]\,.
\end{aligned} \tag{3.6.5}$$

The sum over the new rates again adds up to unity and Eq. (3.6.4) becomes

$$\hat{M}(\mathbf{r}) = \sum_{\gamma \neq 0} \hat{\Omega}_\gamma(\mathbf{r} - \gamma)\hat{M}(\mathbf{r} - \gamma)\,. \tag{3.6.6}$$

Hence we can omit the self jumps by first solving the equation for the 'hatted' variables, and then transforming back to $M(\mathbf{r})$. As $M(\mathbf{r}) \to 1$ for

large r, it is convenient to write

$$\hat{M}(\mathbf{r}) = \frac{7}{8}\left[1 + \delta\hat{M}(\mathbf{r})\right] . \tag{3.6.7}$$

The quantity $\delta\hat{M}(\mathbf{r})$ is in fact the appropriate measure for correlations.[4] After eliminating the two self rates, all jump rates have become $1/14$, except at the origin where the rates to the 8 corners (c) can differ from the rates to the 6 body centers (b). We therefore have

$$\hat{\Omega}_\gamma(\mathbf{r}) = 1/14 + \delta(\mathbf{r})\varepsilon_\gamma . \tag{3.6.8}$$

The rates to the corners are denoted by ε_c and those to the body centers by ε_b. They fulfill the condition $8\varepsilon_c + 6\varepsilon_b = 0$. This results in the following equation:

$$\delta\hat{M}(\mathbf{r}) - \frac{1}{14}\sum_{\gamma\neq 0}\delta\hat{M}(\mathbf{r}-\gamma) = \frac{8}{7}\hat{M}(0)\sum_{\gamma\neq 0}\varepsilon_\gamma\delta\left(\mathbf{r}-\gamma\right) . \tag{3.6.9}$$

Note that this is a discrete version of Poisson's equation: the LHS is a discrete Laplacian and the RHS, originating from deviating rates, acts as a multipole around the origin. This equation is solved in appendix 3.B by a Fourier transformation, leading to

$$\hat{M}(\mathbf{r}) = \frac{7}{8} + \hat{M}(0)\sum_{\mathbf{k}}\frac{E(\mathbf{k})}{1 - D(\mathbf{k})}\exp(-i\mathbf{k}\cdot\mathbf{r}) . \tag{3.6.10}$$

The functions $D(\mathbf{k})$ and $E(\mathbf{k})$ are defined in appendix 3.B; $1 - D(\mathbf{k})$ comes from the discrete Laplacian (in the continuum equation it would simply be k^2), $E(\mathbf{k})$ is the Fourier transform of the source, and the sum over $\mathbf{k}$ is the inverse Fourier transformation running over the Brillouin Zone. The amplitude of the source $\hat{M}(0)$ can be obtained self-consistently, by setting $\mathbf{r} = 0$. This involves a complicated integral over the Brillouin Zone (BZ) of the bcc-lattice; the outcome, however, will be of the order unity. The large r behavior of the correlations is determined by the small $\mathbf{k}$ behavior,

---

[4]For an uncorrelated asymptotic state all $M(\mathbf{r}) = 1$, provided that no indices coincide nor are equal to zero. Any deviation from 1, i.e. $\delta M(\mathbf{r}) \neq 0$, indicates correlations. The same holds for the 'hatted' variables, up to a factor $1 - 2/16 = 7/8$ that comes from the transformation.

so $E(\mathbf{k})/(1 - D(\mathbf{k}))$ has to be expanded around $\mathbf{k} = 0$. The first term that gives a contribution is

$$\frac{49\varepsilon_c}{24} \int \frac{d\mathbf{k}}{(2\pi)^3} \frac{\left(k_x^2 k_y^2 + k_y^2 k_z^2 + k_z^2 k_x^2\right) \exp(-i\mathbf{k} \cdot \mathbf{r})}{k^2}$$

$$\simeq \frac{343\varepsilon_c}{32\pi} \left[5 \frac{x^2 y^2 + y^2 z^2 + z^2 x^2}{r^9} - \frac{1}{r^5}\right] . \qquad (3.6.11)$$

The solution of Eq. (3.6.9) decays as $1/r^5$; the terms $x^2 y^2$ etc. give the proper angular dependence. This result can be directly understood from the analogy with electrostatics. The solution of Poisson's equation Eq. (3.6.9) can be expanded in asymptotically vanishing spherical harmonics: Y_{lm}/r^{l+1}. The symmetry of the bcc lattice allows only harmonics with $l \geq 4$, leading to the observed $1/r^5$ decay.

So we find that the stationary master equation for the moments becomes a discrete Poisson's equation, and the presence of differing transition rates leads to a multipole source around the location of these rates, see Eq. (3.6.9). However, this source is only 'active' if there is no detailed balance, since detailed balance leads to trivial solutions like Eq. (3.6.2).[5] Keeping this in mind, let us now investigate the real fourth order problem, including the differing rates at the special lines and planes. We argue that the asymptotic value is still approached as $1/r^5$, but the amplitude of this field will be modified. Since there is no detailed balance, the differing rates at the lines and planes will act as sources as well. Their amplitudes, however, will decay with increasing distance, since the 'flow' associated with the absence of detailed balance becomes zero at $r \to \infty$. The effect of the induced sources at the special lines and planes can be taken into account perturbatively. The first step is to only consider the effect of the origin, as we have done above. The second step would be to compute the strength of the sources at the lines and planes on the basis of the first order solution, and then to determine their function $E(\mathbf{k})$ and recalculate the solution Eq. (3.6.10). The induced sources around the origin basically lead to a modification of the strength $\hat{M}(0)$, but not of the asymptotic decay. However, the far away points at the lines and planes could modify the asymptotic decay. A closer inspection of the field of these sources shows that it is of order $1/r^7$, since the differing rates lead to a local Laplacian

---

[5] A *discrete* Poisson's equation with a multipole source term can indeed have a short-ranged solution. This is the case if $E(\mathbf{k}) = K(\mathbf{k})(1 - D(\mathbf{k}))$, and $K(\mathbf{k})$ is a regular function.

acting on the first order field decaying as $1/r^5$. Hence, every step of this perturbative calculation yields a leading term $1/r^5$; the amplitude changes in every step and its determination is a difficult problem indeed.

3.6.4 Correlations for general packings

From the previous section, it is clear that correlations occur whenever the detailed balance condition is frustrated around the origin. The stationary master equation then becomes a discrete Poisson's equation in $(n-1)(d-1)$ dimensions, leading to correlations that decay with an integer power of the distance r. Following the derivation in appendix 3.B, it is clear that the asymptotic behavior comes from the lowest non-isotropic term in $E(\mathbf{k})$, since division by $1 - D(\mathbf{k}) \approx k^2$ gives a singularity. The value of the exponent can be calculated as

$$(n - 1)(d - 1) + O - 2 , \qquad (3.6.12)$$

where $(n - 1)(d - 1)$ is the dimensionality of the correlation space and O is the order of the lowest non-isotropic terms in the expansion of $E(\mathbf{k})$. Although this result is remarkably simple, the actual calculation of $E(\mathbf{k})$ is not trivial, as it reflects the symmetries of the jump directions on the $(n - 1)(d - 1)$ dimensional lattice. Working out the 4-dimensional lattice of the third order moments in the fcc packing, we find that $O = 2$ and correlations vanish as $1/r^4$.

3.7 Correlated q-distributions

So far, we have only discussed q-distributions of the type Eq. (3.3.1), for which there are no correlations between q-values at different sites. We have shown that, for these q-distributions, there are no stationary second order weight correlations. In this section we will demonstrate that even the smallest correlation between q-values at different sites induces second order weight correlations. We first solve the problem for arbitrary correlations in the triangular packing. Then, we study the fcc packing assuming only a nearest neighbor q-correlation; this already leads to weight correlations that decay as $1/r^6$.

3.7.1   Triangular packing with arbitrary q-correlations

In general, the (second order) transition rates are defined by Eq. (3.4.5). For $z = 2$, the displacement vector α can only take two values, for which we conveniently choose $\pm\frac{1}{2}$. This allows us to write the transition rates as

$$
\begin{aligned}
\Omega_0(k) &= \overline{q_{i,+\frac{1}{2}}\, q_{i+k,+\frac{1}{2}}} = \overline{q_{i,-\frac{1}{2}}\, q_{i+k,-\frac{1}{2}}}\ , \\
\Omega_{+1}(k) &= \overline{q_{i,-\frac{1}{2}}\, q_{i+k,+\frac{1}{2}}} \\
&= \overline{q_{i,-\frac{1}{2}}\left(1 - q_{i+k,-\frac{1}{2}}\right)} = 1/2 - \Omega_0(k)\ , \\
\Omega_{-1}(k) &= \overline{q_{i,+\frac{1}{2}}\, q_{i+k,-\frac{1}{2}}} \\
&= \overline{q_{i,+\frac{1}{2}}\left(1 - q_{i+k,+\frac{1}{2}}\right)} = 1/2 - \Omega_0(k)\ . \qquad (3.7.1)
\end{aligned}
$$

Asymptotically $\Omega_0(k)$ has to approach the value $1/4$, for q-distributions without long-ranged correlations. As the second moments diffuse on a line, one can easily construct a detailed balance solution:

$$
[1/2 - \Omega_0(k-1)]\, M(k-1) = [1/2 - \Omega_0(k)]\, M(k)\ , \qquad (3.7.2)
$$

or

$$
M(k) = \frac{1/2 - \Omega_0(0)}{1/2 - \Omega_0(k)}\, M(0)\ . \qquad (3.7.3)
$$

This is the general form of the second order weight correlations $M(k)$ in the triangular packing, as a function of $\Omega_0(k)$ that describes the q-correlations. One can draw two interesting conclusions from this result. First of all, there can only be an uncorrelated solution if $\Omega_0(k)$ is constant (i.e. $1/4$) for each $k \neq 0$. This means that even the smallest q-correlations lead to weight correlations. Secondly, the long distance behavior of the second order weight correlations is identical to that of the second order q-correlations, following from the simplicity of Eq. (3.7.3).

3.7.2   fcc packing with nearest neighbor q-correlations

Unfortunately, the analysis is much more complicated for the fcc packing, whose second order moments live on the 2-dimensional triangular lattice of Fig. 3.5. We therefore allow only correlations between q-values at neighboring sites. Remember that one can easily construct an uncorrelated solution $M(\mathbf{r})$ for uncorrelated q-distributions, Eq. (3.6.1), since all detailed balance conditions at the origin are identical by symmetry. This

still holds when there are nearest neighbor correlations. However, the detailed balance condition will now be frustrated on the ring of surrounding sites, as these are connected in four a priori different directions, see Fig. 3.5. In analogy to the problem discussed in the previous section, the stationary master equation for $\delta\hat{M}(\mathbf{r})$ transforms into

$$\delta\hat{M}(\mathbf{r}) - 1/6 \sum_{\gamma\neq\mathbf{0}} \delta\hat{M}(\mathbf{r}-\boldsymbol{\gamma}) = \rho(\mathbf{r}) \ . \tag{3.7.4}$$

The 'charge density' $\rho(\mathbf{r})$ is only non-zero around the frustrated ring, see appendix 3.C. Again, it is a discrete version of Poisson's equation, but now in 2-dimensions. The solution can therefore be expanded in cylindrical harmonics, $\exp(in\phi)/r^n$, and the six-fold symmetry of the lattice requires $n \geq 6$. The problem is again solved rigorously by Fourier transformation of Eq. (3.7.4). In appendix 3.C we show that

$$\delta\hat{M}(\mathbf{r}) \propto \frac{\cos(6\phi)}{r^6} \ , \tag{3.7.5}$$

which is in agreement with the simple electrostatic picture.
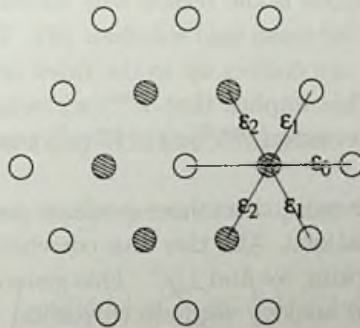
Figure 3.5: fcc packing: second order moments diffuse on a triangular lattice. The ring around the origin has differing rates.

So, for the fcc packing, we find that even a nearest neighbor q-correlation leads to second order weight correlations that decay with a power law. This algebraic decay is generic for $z \geq 3$ since any q-correlations lead to a master equation whose detailed balance relations cannot be solved around the origin.

3.8   Conclusion

We have studied stationary solutions and the corresponding weight cor-
relations in the q-model, for general q-distributions. It turns out that
there is a special class of q-distributions, given by Eq. (3.3.9), for which
the stationary solution is a product measure, and thus displays no weight
correlations at all. This has been demonstrated by means of condition
(3.3.7), which has a nice physical interpretation in terms of the 'inter-
particle forces' qw.

All q-distributions that do not fall into this special class *do* give rise
to weight correlations. The calculated correlation functions are rather un-
usual: for q-distributions of the type Eq. (3.3.1), correlations only show up
at higher orders, and these correlations decay with a power of the distance.
The results for the triangular packing and the fcc packing are summarized
in Table 3.1. To examplify these results, consider two different sites i and
$i + k$ in a layer of the triangular packing. Since there are no correlations
in the second and third order weight moments, we find $\langle w_i w_{i+k} \rangle = 1$ and
$\langle w_i^2 w_{i+k} \rangle = \langle w^2 \rangle$, independent of the distance k. However, the moments
$\langle w_i^3 w_{i+k} \rangle$ and $\langle w_i^2 w_{i+k}^2 \rangle$ do display correlations and approach their asym-
potitic values as $1/k^5$. The fact that one has to go to higher orders to
observe weight correlations is the reason why numerical simulations only
marginally differ from the mean field solutions [30]. The (single-site) mean
field solutions $\mathcal{P}^{\mathrm{mf}}(w)$ are correct up to the third order moments, for the
triangular packing. This implies that $\mathcal{P}^{\mathrm{mf}}(w)$ 'wiggles' around the real
solution $\mathcal{P}^*(w)$; the deviation $\mathcal{P}^{\mathrm{mf}}(w) - \mathcal{P}^*(w)$ changes its sign 4 times
(Fig. 3.1).

Packings that have more than three q-values per site ($z \geq 3$) already
have third order correlations. Also this time correlations only decay algeb-
raically; for the fcc packing we find $1/r^4$. This generic algebraic decay can
be understood from an analogy with electrostatics. The weight moments
evolve according to a master equation, and the corresponding station-
ary state is described by a discrete version of Poisson's equation. The
'source' turns out to be a multipole around the origin, which is only act-
ive whenever the master equation has no simple detailed balance solution.
The moments therefore approach their asymptotic (uncorrelated) values
algebraically. The value of the exponent depends on the dimension of the
correlation space $(n - 1)(d - 1)$, and on the symmetry of the multipole,
see Eq. (3.6.12).

Finally, we found that there will be second order weight correlations

whenever the q-values of different sites are correlated. Even with only nearest neighbor q-correlations, the fcc packing has weight correlations that vanish as $1/r^6$. Again, the triangular packing is less sensitive for correlations; the nature of the weight correlations is identical to that of the q-correlations, Eq. (3.7.3).

packing	$n = 2$	$n = 3$	$n = 4$	$n = 2$, with q-corr.
triangular $(d = 2)$	line no corr.	triangular no corr.	bcc $1/r^5$	line like q-corr.
fcc $(d = 3)$	triangular no corr.	4-dim. $1/r^4$	6-dim. -	triangular $1/r^6$

Table 3.1: Summary of the results for the triangular packing ($z = 2$; $d = 2$) and the fcc packing ($z = 3$; $d = 3$). The nth order weight moments diffuse on a $(n - 1)(d - 1)$ dimensional lattice; the lattice structures are listed in the first row. The second row shows the nature of the corresponding weight correlations in the stationary state.

3.A   Moments of q-distributions

This appendix is about the moments of the q-distributions, defined by

$$\overline{q_1^{n_1} q_2^{n_2} ... q_z^{n_z}} = \int \eta(\vec{q}) \delta \left(1 - \sum_\alpha q_\alpha \right) d\vec{q} \, q_1^{n_1} q_2^{n_2} ... q_z^{n_z} . \qquad (3.A.1)$$

These different moments are not independent because of the δ-constraint. As the distributions are normalized, the zeroth order moments are unity; the first order moments are, of course, all $1/z$. All second order moments, for which $\sum_i n_i = 2$, can be described by only one free parameter. Defining η_n as

$$\eta_n = \int \eta(\vec{q}) \delta \left(1 - \sum_\alpha q_\alpha \right) d\vec{q} \, q_1^n , \qquad (3.A.2)$$

one finds

$$\sum_{i=1}^{z} \overline{q_1 q_i} = \eta_2 + (z-1)\overline{q_1 q_2} =$$

$$\int \eta(\vec{q})\delta\left(1 - \sum_{\alpha} q_\alpha\right) d\vec{q} \; q_1 \sum_{i=1}^{z} q_i = 1/z , \qquad (3.A.3)$$

hence

$$\overline{q_1 q_2} = \frac{1}{(z-1)}(1/z - \eta_2) . \qquad (3.A.4)$$

From a similar argument, one can derive for the third order moments

$$\overline{q_1^3} = \eta_3 \qquad \overline{q_1^2 q_2} = \frac{1}{(z-1)}(\eta_2 - \eta_3) . \qquad (3.A.5)$$

For $z = 2$ there is even a relation between η_3 and η_2:

$$1 = \sum_{ijk} \overline{q_i q_j q_k} = 2\eta_3 + 6\overline{q_1^2 q_2} \quad\Longrightarrow\quad \eta_3 = \frac{3}{2}\eta_2 - 1/4 . \qquad (3.A.6)$$

For $z = 3$, there is an additional third moment, namely

$$1 = \sum_{ijk} \overline{q_i q_j q_k} = 3\eta_3 + 18\overline{q_1^2 q_2} + 6\overline{q_1 q_2 q_3}$$

$$\Longrightarrow \quad \overline{q_1 q_2 q_3} = \frac{1}{6}(1 - 9\eta_2 + 6\eta_3) . \qquad (3.A.7)$$

The extension to higher orders and higher z is straightforward.

For the special class of $\eta(\vec{q})$ defined in Eq. (3.3.9), one can calculate the moments η_n from a generalization of Eq. (3.3.8) [68]

$$\eta_n = \frac{\Gamma(zr)\Gamma(r+n)}{\Gamma(r)\Gamma(zr+n)} . \qquad (3.A.8)$$

In order to show that Eq. (3.3.16) is indeed obeyed by the special class (with $z = 2$), we first invert Eq. (3.A.8) for $n = 2$

$$\eta_2 = \frac{r+1}{4r+2} \quad\Longrightarrow\quad r = \frac{1 - 2\eta_2}{4\eta_2 - 1} . \qquad (3.A.9)$$

From this one can calculate η_4 as a function of η_2, which precisely results in Eq. (3.3.16). A similar inversion for $z = 3$ leads to

$$r = \frac{1 - 3\eta_2}{9\eta_2 - 1} , \qquad (3.A.10)$$

from which one derives Eq. (3.3.17).

3.B The bcc lattice

In the triangular packing, the fourth order weight moments $\langle w_i w_{i+k} w_{i+l} w_{i+m}\rangle$ diffuse on the bcc lattice of Fig. 3.4, with differing jump rates on special lines and planes. In this appendix, we list these rates explicitly and we solve the corresponding stationary master equation.

The jump rates can be calculated from

$$\Omega_\gamma(k, l, m) = \overline{q_{i,\alpha}\, q_{i+k,\alpha'}\, q_{i+l,\alpha''}\, q_{i+k,\alpha'''}} \;, \qquad (3.B.1)$$

with the $z^4 = 16$ jump directions

$$\gamma = (\alpha' - \alpha, \alpha'' - \alpha, \alpha''' - \alpha) \;. \qquad (3.B.2)$$

As α can take the values $\pm\frac{1}{2}$, there are two *self rates* for which all α's are the same. As a consequence, there are 14 outgoing directions, namely $\pm(1, 0, 0)$, $\pm(1, 1, 1)$, and $\pm(1, 1, 0)$ plus their permutations. The first two are directions for which three of the four α's are equal, and they correspond to the *corners* of Fig. 3.4; the third represents the jumps towards the *body centers*. If all position indices in Eq. (3.B.1) are different, the transition rates are simply $1/z^4 = 1/16$. On the special lines and planes where one or more position indices coincide, we encounter differing rates. The geometry of the problem is summerized in Table 3.2.

	from \ to	$(0,0,0)$	$(k,0,0)$	$(k,k,0)$	$(k,l,0)$	(k,l,m)
origin	$(0,0,0)$	$\overline{q_1^4}$	$\overline{q_1^3 q_2}$	$\overline{q_1^2 q_2^2}$	–	–
line (c)	$(k,0,0)$ (k,k,k)	$\frac{1}{2}\overline{q_1^3}$	$\frac{1}{2}\overline{q_1^3}$	$\frac{1}{2}\overline{q_1^2 q_2}$	$\frac{1}{2}\overline{q_1^2 q_2}$	–
line (b)	$(k,k,0)$	$(\overline{q_1^2})^2$	$\overline{q_1^2}\,\overline{q_1 q_2}$	$(\overline{q_1^2})^2$	$\overline{q_1^2}\,\overline{q_1 q_2}$	$(\overline{q_1 q_2})^2$
plane	$(k,l,0)$ (k,k,l)	–	$\frac{1}{4}\overline{q_1^2}$	$\frac{1}{4}\overline{q_1^2}$	$\frac{1}{4}\overline{q_1^2}$	$\frac{1}{4}\overline{q_1 q_2}$
bulk	(k,l,m)	–	–	$\frac{1}{16}$	$\frac{1}{16}$	$\frac{1}{16}$

Table 3.2: The transition rates $\Omega_\gamma(\mathbf{r})$ for the fourth order master equation.

From this table we deduce the rates ε_c to the corners and ε_b to the

body centers, which occur in relation (3.6.8). We find

$$\varepsilon_c = \frac{\overline{q_1^3 q_2}}{1 - 2\overline{q_1^4}} - \frac{1}{14}, \qquad \varepsilon_b = \frac{\overline{q_1^2 q_2^2}}{1 - 2\overline{q_1^4}} - \frac{1}{14}, \qquad (3.B.3)$$

and one easily verifies from the property $q_1 + q_2 = 1$ that the relation $8\varepsilon_c + 6\varepsilon_b = 0$ holds. In general, the rates do not obey the detailed balance condition Eq. (3.5.5) in the elementary loop *origin-corner-body center-origin*. Keeping only the rates in this loop as deviations from the bulk leads to Eq. (3.6.9). For the definition of the two functions $E(\mathbf{k})$ and $D(\mathbf{k})$ we introduce two auxiliary functions: one for the contribution of the corners

$$\begin{aligned}
\tilde{E}_c(\mathbf{k}) &= \frac{1}{4}\left[\cos\frac{k_x + k_y + k_z}{2} + \cos\frac{k_x - k_y + k_z}{2}\right.\\
&\left. + \cos\frac{k_x + k_y - k_z}{2} + \cos\frac{k_x - k_y - k_z}{2}\right]
\end{aligned}$$
$$(3.B.4)$$

and one related to the body centers

$$\tilde{E}_b(\mathbf{k}) = \frac{1}{3}(\cos k_x + \cos k_y + \cos k_z) . \qquad (3.B.5)$$

The two functions $\tilde{D}(\mathbf{k})$ and $\tilde{E}(\mathbf{k})$ are then given as

$$\begin{aligned}
\tilde{D}(\mathbf{k}) &= \frac{4}{7}\tilde{E}_c(\mathbf{k}) + \frac{3}{7}\tilde{E}_b(\mathbf{k})\\
\tilde{E}(\mathbf{k}) &= \varepsilon[\,\tilde{E}_c(\mathbf{k}) - \tilde{E}_b(\mathbf{k})\,] ,
\end{aligned} \qquad (3.B.6)$$

with $\varepsilon = 8\varepsilon_c = -6\varepsilon_b$.

For the large $\mathbf{r}$ behavior we need the expansions for small k. One finds

$$\tilde{E}_c(\mathbf{k}) = 1 - \frac{1}{8}k^2 + \frac{1}{384}[k^4 + 4(k_x^2 k_y^2 + k_y^2 k_z^2 + k_z^2 k_x^2)] + \cdots \qquad (3.B.7)$$

and

$$\tilde{E}_b(\mathbf{k}) = 1 - \frac{1}{6}k^2 + \frac{1}{72}[k^4 - (k_x^2 k_y^2 + k_y^2 k_z^2 + k_z^2 k_x^2)] + \cdots \qquad (3.B.8)$$

From these expressions one derives the expansion

$$\frac{\tilde{E}(\mathbf{k})}{1 - \tilde{D}(\mathbf{k})} = \frac{7\varepsilon}{24}\left(1 - \frac{7}{32}k^2 + \frac{7}{8}\frac{k_x^2 k_y^2 + k_y^2 k_z^2 + k_z^2 k_x^2}{k^2} + \cdots\right) . \qquad (3.B.9)$$

The first two terms in the expansion are regular and thus give rise to short range contributions. The last term leads to the asymptotic behavior, by means of the inverse Fourier transform

$$\int \frac{d\mathbf{k}}{(2\pi)^3} \frac{\left(k_x^2 k_y^2 + k_y^2 k_z^2 + k_z^2 k_x^2\right) \exp(-i\mathbf{k} \cdot \mathbf{r})}{k^2} . \qquad (3.B.10)$$

This integral can be evaluated by differentiation of the well-known

$$\int \frac{d\mathbf{k}}{(2\pi)^3} \frac{\exp(-i\mathbf{k} \cdot \mathbf{r})}{k^2} \simeq \frac{1}{4\pi r} , \qquad (3.B.11)$$

where a factor k_x in Eq. (3.B.10) corresponds to applying $\partial/\partial x$. This leads to expression Eq. (3.6.11).

3.C $\quad q$-correlations in the fcc packing

In Eq. (3.7.4) we formulated the problem for the second moments in the fcc packing with nearest-neighbor q-correlations. The 'charge density' $\rho(\mathbf{r})$ on the right hand side of the equation is the product of the moment $\hat{M}(\boldsymbol{\gamma})$, referring to the neighbors of the origin (all are the same by symmetry), with a function whose Fourier transform is given by

$$\tilde{E}(\mathbf{k}) = \sum_{\gamma',\gamma} \omega_{\gamma-\gamma'} \exp[i\mathbf{k} \cdot (\boldsymbol{\gamma} + \boldsymbol{\gamma}')] . \qquad (3.C.1)$$

The $\omega_{\gamma-\gamma'}$ are the deviations from the bulk transition rates $1/6$. These are only non-zero for the ring of nearest neighbors around the origin shown in Fig. 3.5:

$$\begin{aligned} \omega_0 &= -\varepsilon_0, & \omega_1 = \omega_5 = -\varepsilon_1, \\ \omega_2 &= \omega_4 = -\varepsilon_2, & \omega_3 = \varepsilon_0 + 2\varepsilon_1 + 2\varepsilon_2 . \end{aligned} \qquad (3.C.2)$$

The equalities reflect the symmetry of the triangular lattice. Inserting Eq. (3.C.1) into the Fourier transform of Eq. (3.7.4) leads to

$$\hat{M}(\mathbf{r}) = 2/3 + \hat{M}(\boldsymbol{\gamma}) \sum_{\mathbf{k}} \frac{\tilde{E}(\mathbf{k})}{1 - \tilde{D}(\mathbf{k})} \exp(-i\mathbf{k} \cdot \mathbf{r}) . \qquad (3.C.3)$$

The consistency equation for $\hat{M}(\boldsymbol{\gamma})$ follows by taking $\mathbf{r}$ as one of the nearest neighbors of the origin. The function $\tilde{D}(\mathbf{k})$ is given by

$$\tilde{D}(\mathbf{k}) = \frac{1}{3} \left(\cos k_x + \cos \frac{k_x + \sqrt{3}k_y}{2} + \cos \frac{k_x - \sqrt{3}k_y}{2} \right) , \qquad (3.C.4)$$

and $\tilde{E}(\mathbf{k})$ can be expressed as

$$\tilde{E}(\mathbf{k})/6 = \varepsilon_0[1 - \tilde{D}(2\mathbf{k})] + 2\varepsilon_1[1 - \tilde{D}'(\mathbf{k})] + 2\varepsilon_2[1 - \tilde{D}(\mathbf{k})] , \qquad (3.C.5)$$

with the new function

$$\tilde{D}'(\mathbf{k}) = \tilde{D}(\sqrt{3}\,k_y, \sqrt{3}\,k_x) . \qquad (3.C.6)$$

For the asymptotic behavior of $\hat{M}(\mathbf{r})$ we must make an expansion of $\tilde{E}(\mathbf{k})/(1 - \tilde{D}(\mathbf{k}))$. For the first two terms we find

$$\frac{1 - \tilde{D}(2\mathbf{k})}{1 - \tilde{D}(\mathbf{k})} = 4\left(1 - \frac{3}{16}k^2 + \frac{3}{256}k^4 + \frac{1}{192}\frac{k_x^6 - 6k_x^4 k_y^2 + 9k_x^2 k_y^4}{k^2} + \cdots\right) ,$$
$$\qquad (3.C.7)$$

$$\frac{1 - \tilde{D}'(\mathbf{k})}{1 - \tilde{D}(\mathbf{k})} = 3\left(1 - \frac{1}{8}k^2 + \frac{1}{128}k^4 + \frac{1}{288}\frac{k_x^6 - 6k_x^4 k_y^2 + 9k_x^2 k_y^4}{k^2} + \cdots\right) ,$$
$$\qquad (3.C.8)$$

and the third term is simply a constant. The asymptotic behavior is given by Fourier inversion of the first singular term in $\mathbf{k}$, i.e.

$$\int \frac{d\mathbf{k}}{(2\pi)^2} \frac{(k_x^6 - 6k_x^4 k_y^2 + 9k_x^2 k_y^4)\exp(-i\mathbf{k}\cdot\mathbf{r})}{k^2} \simeq \frac{960}{\pi}\frac{\cos(6\phi)}{r^6} . \qquad (3.C.9)$$

This integral can be obtained by differentiation of

$$\int \frac{d\mathbf{k}}{(2\pi)^2} \frac{\exp(-i\mathbf{k}\cdot\mathbf{r})}{k^2} \simeq \frac{\log(L/r)}{2\pi} , \qquad (3.C.10)$$

where L is the size of the system.

Relaxation of weight distributions in the q-model

4.1 Introduction

So far, we have investigated the q-model in the limit of large depths. Interpreting the downward direction as time, this corresponds to the limit $t \to \infty$. In this chapter we study transient behavior in the q-model: How is the approach to the stationary $\mathcal{P}^*(w)$ as a function of time? In terms of granular media, this transient behavior expresses how force or weight fluctuations build up from the top surface into the bulk of the packing; some results of this chapter have already been compared to our simulations of Hertzian particles in Chapter 2.

Most of the analysis will be about the q-model without injection, i.e. starting from Eq. (3.2.2). This corresponds to a situation where the applied force on the top layer is large compared to the particle weight, or when the direction of propagation is perpendicular to gravity. At the end of this chapter, we show how the injection term affects the relaxation.

4.2 Uniqueness of stationary solutions

This section addresses the question of which initial weight distributions evolve to the stationary states that were analyzed in the previous section. So, in what sense are the fixed points unique for a given $H(\vec{q})$?

The strategy is to first study an obvious invariant of the problem: the total weight on the particles of one layer

$$W = \sum_i w_i \ . \tag{4.2.1}$$

This is an invariant since

$$W' = \sum_j w'_j = \sum_{j,\alpha} q_{j-\alpha,\alpha} w_{j-\alpha} = W \ , \tag{4.2.2}$$

which follows from changing the summation variable j to $i = j - \alpha$. Due to the linearity of Eq. (3.2.2), the magnitude of W is irrelevant for the problem. We could thus fix the value of W and only consider distributions having strictly this value, but it is mathematically more convenient to allow for fluctuations in W, described by a distribution $\mathcal{R}(W)$:

$$\mathcal{R}(W) = \int d\vec{w}\, P(\vec{w})\, \delta\left(W - \sum_i w_i\right) \ . \tag{4.2.3}$$

It is easily shown that $R(W)$ is invariant under recursion, since Eq. (4.2.2) holds for any set of q's:

$$
\begin{aligned}
\mathcal{R}'(W) &= \int d\vec{w}'\, P'(\vec{w}')\, \delta\left(W - \sum_j w'_j\right) \\
&= \int d\vec{q}\, H(\vec{q}) \int d\vec{w}\, P(\vec{w})\, \delta\left(W - \sum_i w_i\right) \\
&= \mathcal{R}(W) \ .
\end{aligned}
\tag{4.2.4}
$$

So, the initial distribution $\mathcal{R}^{(0)}(W)$ dictates that of the stationary state at infinite depth. This might seems a strong restriction on the relaxation of the distribution function, but this is not so in the thermodynamic limit where $N \to \infty$. To see this, we exploit the invariance of the moments of $\mathcal{R}(W)$:

$$
\begin{aligned}
\langle W^n \rangle &= \int_i^\infty dW\, W^n\, \mathcal{R}(W) \\
&= \int d\vec{w} \left(\sum_{i_1 \cdots i_n} w_{i_1} \cdots w_{i_n}\right) P(\vec{w}) \\
&= \sum_{i_1 \cdots i_n} \langle w_{i_1} \cdots w_{i_n} \rangle \ .
\end{aligned}
\tag{4.2.5}
$$

Hence the sum over all weight moments is also invariant under recursion. Now consider the second moments. Any multiple of Eq. (3.6.1) is a stationary solution, so we can write

$$\langle \mathcal{W}^2 \rangle = c \left[N(N-1) + N \frac{z-1}{z(1-z\eta_2)} \right] . \qquad (4.2.6)$$

Due to the invariance of $\langle \mathcal{W}^2 \rangle$, the value of c is solely determined by the initial conditions, which we write as

$$\langle w_i w_j \rangle^{(0)} = 1 + \delta M^{(0)}(i,j) . \qquad (4.2.7)$$

The terms $\delta M^{(0)}(i,j)$ represent correlations in the (initial) second order moments. Equating the sum of these moments with Eq. (4.2.6) yields

$$c = \frac{1 + \frac{1}{N^2} \sum_{i,j} \delta M^{(0)}(i,j)}{1 + \frac{1}{N} \left(\frac{z-1}{z(1-z\eta_2)} - 1 \right)} . \qquad (4.2.8)$$

We thus find that $c = 1$ in the limit $N \to \infty$, unless the sum over the N^2 correlation terms is of the order N^2. This is never the case, however, as long as all correlations are finite and decay as a function of the distance $\mathbf{r} = |\mathbf{r}_i - \mathbf{r}_j|$, i.e.

$$\lim_{\mathbf{r} \to \infty} \delta M^{(0)}(\mathbf{r}) = 0 . \qquad (4.2.9)$$

What does this mean? First of all that in the thermodynamic limit, all physically acceptable initial conditions will lead to the same stationary solution[1], since $c = 1$. This also follows from the observation that all initial $\mathcal{R}^{(0)}(\mathcal{W})$ become sharply peaked as $N \to \infty$:

$$\frac{\langle (\Delta \mathcal{W})^2 \rangle}{\langle \mathcal{W} \rangle^2} = \frac{1}{N^2} \sum_{i,j} \delta M^{(0)}(i,j) \longrightarrow 0 . \qquad (4.2.10)$$

This is very reminiscent of the behavior of the energy distribution in the canonical ensemble. Indeed this analogy, also mentioned in [30], is illuminating. It is well known that correlation functions in the canonical ensemble and the micro-canonical ensemble (in which the energy is fixed), coincide for all distances, up to order $1/N$. Fixing $\mathcal{W}$ in the q-model,

---

[1]We have shown this explicitly for the second order moments, but starting from Eq. (4.2.5), the analysis is similar for the higher moments.

e.g. by putting $\delta M^{(0)}(i,j) = 0$, would also lead to $1/N$ corrections for c and thus for the correlation functions. Another consequence of the analysis above is that in *finite* systems, there are many different stationary solutions. However, these differ only up to order $1/N$ from one another.

4.3   Diffusion of first moments

Before we address the relaxation of the second and higher order moments, we first show that spatially inhomogeneous weights on the top layer will diffusively spread into the lower layers [33]. This is why the q-model is referred to as a *parabolic* model: the continuum limit of this process of weight propagation is a simple (parabolic) diffusion equation.

We thus consider the first moments $\langle w_j \rangle$ for an inhomogeneous initial distribution. The evolution of these moments is given by

$$\langle w_j \rangle' = \int d\vec{q}\, H(\vec{q}) \int d\vec{w}\, \mathcal{P}(\vec{w}) \sum_\alpha q_{j-\alpha,\alpha}\, w_{j-\alpha} = \frac{1}{z} \sum_\alpha \langle w_{j-\alpha} \rangle \ . \quad (4.3.1)$$

This simple recursion law tells us that all localized first moments gradually spread over the lower layers like ordinary random walkers.

In order to understand the role of system size it is useful to inspect the Fourier transform

$$m(\mathbf{k}) = \sum_i \langle w_i \rangle \exp(i\mathbf{k} \cdot \mathbf{r}_i) \ , \quad (4.3.2)$$

which relaxes from layer to layer as

$$m'(\mathbf{k}) = \lambda(\mathbf{k})\, m(\mathbf{k}) \ , \quad (4.3.3)$$

with the transmission function

$$\lambda(\mathbf{k}) = \frac{1}{z} \sum_\alpha \exp(i\mathbf{k} \cdot \mathbf{r}_\alpha) \ . \quad (4.3.4)$$

In accordance with the conservation of the total weight, we see that the mode $\mathbf{k} = \mathbf{0}$ is conserved as $\lambda(\mathbf{0}) = 1$. All the other modes decay exponentially since $|\lambda(\mathbf{k} \neq \mathbf{0})| < 1$. So we find asymptotically

$$m^{(\infty)}(\mathbf{k}) = \delta_{\mathbf{k},0}\, m(\mathbf{0}) \ , \quad (4.3.5)$$

with $m(0)$ the average of the (initial) total weight. Translating it back to space yields

$$\langle w_i \rangle^{(\infty)} = \langle \mathcal{W} \rangle / N \ , \qquad (4.3.6)$$

i.e. all sites feel the same average weight regardless of the initial distribution.

Clearly this result holds in the limit $t \gg N$, where t denotes the position of a given layer with respect to the top. In the other limit $N \gg t$ we may replace the summation over $\mathbf{k}$ by an integration over the Brillouin Zone (BZ) of the (d-1)-dimensional layer and one gets the standard diffusion process from the integral

$$\langle w_j \rangle^{(t)} \simeq \left(\frac{1}{2\pi} \right)^{d-1} \int_{BZ} d\mathbf{k} \, m^{(0)}(\mathbf{k}) \, e^{t \log[\lambda(\mathbf{k})] - i\mathbf{k}\cdot\mathbf{r}_j} \ . \qquad (4.3.7)$$

In the limit of large t the integral can be evaluated by the saddle point method, using the fact that the dominant contribution comes from small $\mathbf{k}$. This allows us to approximate $\lambda(\mathbf{k})$ by

$$\log[\lambda(\mathbf{k})] \simeq \log[1 - \sum_\alpha (\mathbf{k}\cdot\mathbf{r}_\alpha)^2/2] \simeq -D\,k^2 \ , \qquad (4.3.8)$$

which renders the integration effectively a Gaussian:

$$
\begin{aligned}
\langle w_j \rangle^{(t)} &\simeq \sum_i \langle w_i \rangle^{(0)} \left(\frac{1}{2\pi} \right)^{d-1} \int_{BZ} d\mathbf{k} \, e^{-Dtk^2 - i\mathbf{k}\cdot(\mathbf{r}_j - \mathbf{r}_i)} \\
&\simeq \sum_i \langle w_i \rangle^{(0)} \left(\frac{1}{\sqrt{4\pi Dt}} \right)^{d-1} e^{-(\mathbf{r}_j - \mathbf{r}_i)^2/4Dt} \ . \qquad (4.3.9)
\end{aligned}
$$

The diffusion constant D depends on the latttice structure of the layer, with $D = 1/8$ for the triangular packing and $D = 1/12$ for the fcc packing. Thus one sees that the ratio of t/N decides whether we should take a discrete sum over the $\mathbf{k}$ variables ($t \gg N$) or whether we should integrate over the Brillouin Zone ($N \gg t$). In the first case, only $\mathbf{k} = 0$ matters and we have diffusion crossing the periodic boundary conditions in the layer. In the second case, a region around $\mathbf{k} = 0$ has an influence and there are no effects from the finite size of the layer.

4.4   Relaxation of second moments

Having seen the washing out of spatial inhomogeneities, we now concentrate on translationally invariant initial conditions and on the case $N \gg t$. The relaxational properties of $\mathcal{P}(\vec{w})$ then show up in the second and higher order moments. To study the relaxation of the second moments, we use the master equation formulation Eq. (3.4.4), that has been derived in the previous Chapter. This relaxation is an anomalous diffusion process, since the transition rates are all $1/z^2$, except those leaving the origin, see Eq. (3.4.8). It is therefore convenient to write the recursion as

$$\langle w_i w_{i+n} \rangle' = \frac{1}{z^2} \sum_\gamma \langle w_i w_{i+n-\gamma} \rangle + g_n \langle w_i^2 \rangle , \tag{4.4.1}$$

where the function g_n incorporates the anomalous transition rates; the only non-zero terms are

$$g_0 = z \left(\eta_2 - 1/z^2 \right) , \qquad g_{\gamma \neq 0} = -\frac{\eta_2 - 1/z^2}{z-1} . \tag{4.4.2}$$

To study the relaxation in more detail, we consider the difference with respect to values of the stationary distribution

$$A_n = \langle w_i w_{i+n} \rangle - \langle w_i w_{i+n} \rangle^* , \tag{4.4.3}$$

which will of course relax according to Eq. (4.4.1) as well. To examplify this relaxation process, we have depicted the flow diagram for the A_n for the triangular packing in Fig. 4.1. The advantage of taking the difference
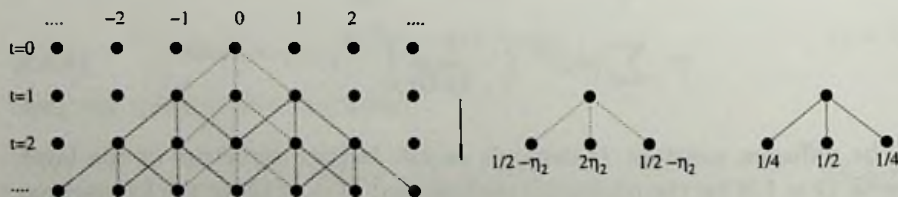

Figure 4.1: The flow diagram for $A_n^{(t)}$ in the triangular lattice, starting with only $A_0^{(0)} \neq 0$; the horizontal index n indicates the relative distance. Since $2\eta_2$ is larger than $1/2$, the values of $A_0^{(t)}$ will be enhanced.

is that its Fourier transform is well behaved for distributions which have

short range correlations, since both the initial correlation function and the stationary values approach 1 for large distances n. The Fourier transforms are defined as

$$A(\mathbf{k}) = \sum_n A_n \exp(i\mathbf{k} \cdot \mathbf{r}_n), \quad A_n = \left(\frac{1}{2\pi}\right)^{d-1} \int_{BZ} d\mathbf{k} \, A(\mathbf{k}) \exp(-i\mathbf{k} \cdot \mathbf{r}_n) ,$$

(4.4.4)

and $A(\mathbf{k})$ transforms as

$$A'(\mathbf{k}) = \lambda(\mathbf{k}) \, \lambda(-\mathbf{k}) \, A(\mathbf{k}) + A_0 \, g(\mathbf{k}). \tag{4.4.5}$$

The correction function $g(\mathbf{k})$ reads

$$g(\mathbf{k}) = g_0 + \sum_{\gamma \neq 0} g_\gamma \exp(i\mathbf{k} \cdot \boldsymbol{\gamma}) = \left(\frac{z^2 \eta_2 - 1}{z - 1}\right) \left[1 - \lambda(\mathbf{k}) \, \lambda(-\mathbf{k}) \right] . \tag{4.4.6}$$

The recursion of Eq. (4.4.5) can be solved by introducing the generating function

$$A(u, \mathbf{k}) = \sum_{t=0}^{\infty} A^{(t)}(\mathbf{k}) \, u^t , \tag{4.4.7}$$

where the sum extends over all layers t. Multiplying Eq. (4.4.5) by u^{t+1} and summing over t gives an algebraic equation for the generating function

$$A(u, \mathbf{k}) - A^{(0)}(\mathbf{k}) = u \left[\lambda(\mathbf{k}) \, \lambda(-\mathbf{k}) \, A(u, \mathbf{k}) + A_0(u) \, g(\mathbf{k}) \right] . \tag{4.4.8}$$

Here we introduced the auxiliary function $A_0(u)$

$$A_0(u) = \sum_{t=0}^{\infty} A_0^{(t)} \, u^t , \tag{4.4.9}$$

which can also be obtained from $A(u, \mathbf{k})$ by inverse Fourier transformation

$$A_0(u) = \left(\frac{1}{2\pi}\right)^{d-1} \int_{BZ} d\mathbf{k} \, A(u, \mathbf{k}) . \tag{4.4.10}$$

This $A_0(u)$ is our prime interest as it contains the center coefficients $A_0^{(t)}$, giving information about the relaxation of the single-site weight distribution. The other $A_n^{(t)}$ contain correlations between two sites.

Using Eq. (4.4.6), we rewrite Eq. (4.4.8) as

$$A(u,k) = \frac{A^{(0)}(\mathbf{k})}{1 - u\,\lambda(\mathbf{k})\,\lambda(-\mathbf{k})} + \left(\frac{z^2\eta_2 - 1}{z - 1}\right) A_0(u) \left(1 - \frac{1 - u}{1 - u\,\lambda(\mathbf{k})\,\lambda(-\mathbf{k})}\right)$$

$$(4.4.11)$$

Together with Eq. (4.4.10), this has become a closed equation for $A_0(u)$. Before solving this equation, let us briefly discuss the terms appearing on the right hand side. The first term will be shown to give purely diffusive behavior, since without the corrections g_n, Eq. (4.4.1) becomes a regular random walk in a layer of dimension $d - 1$. The second and third term originate from the g_n; we show below that the second term contains a correction to the asymptotic amplitude, whereas the third term (proportional to $1 - u$) will turn out to represent a transient. Hence, we anticipate diffusive relaxation $\sim \left(1/\sqrt{t}\right)^{(d-1)}$.

We have assumed the initial conditions to be short-ranged, such that $A^{(0)}(\mathbf{k})$ is a regular function of $\mathbf{k}$ at the origin. Since the large t behavior turns out to be dominated by the behavior at small $\mathbf{k}$, we may as well consider totally *uncorrelated* initial distributions. For such initial conditions, only $A_0^{(0)}$ is nonzero, see e.g. Fig. 4.1. The value of $A_0^{(0)}$ sets the amplitude of the relaxation process as

$$A^{(0)}(\mathbf{k}) = A_0^{(0)} \ . \tag{4.4.12}$$

Before discussing the asymptotics of the general case we begin by giving the results for the triangular packing with $z = 2$. In this case all the integrals can be carried out explicitly by writing them as contour integrals in the complex $v = e^{ik}$ plane; the explicit calculation is given in Appendix 4.A. From (4.4.10) and (4.4.11) we get

$$A_0(u) = \frac{A_0^{(0)}}{\sqrt{1 - u}} + (4\eta_2 - 1)\, A_0(u) \left(1 - \frac{1 - u}{\sqrt{1 - u}}\right) , \tag{4.4.13}$$

which can be solved as

$$A_0(u) = \frac{1}{2(1 - 2\eta_2)} \frac{A_0^{(0)}}{\sqrt{1 - u}} \left(\frac{1}{1 + \frac{4\eta_2 - 1}{2(1 - 2\eta_2)}\sqrt{1 - u}}\right) . \tag{4.4.14}$$

This intricate result is best understood for a concrete example. We therefore consider the uniform q-distribution, which has $\eta_2 = 1/3$ and $\langle w^2 \rangle^* = 3/2$. The function $A_0(u)$ then simply reads

$$
\begin{aligned}
A_0(u) &= \frac{3A_0^{(0)}}{2\sqrt{1-u}} \left(\frac{1}{1+\frac{1}{2}\sqrt{1-u}} \right) \\
&= \frac{3A_0^{(0)}}{2\sqrt{1-u}} \left(1 - \frac{1}{2}\sqrt{1-u} + \frac{1}{4}(1-u) - \cdots \right) . \quad (4.4.15)
\end{aligned}
$$

The expansion in powers of $\sqrt{1-u}$ is instructive since each higher order term leads to a weaker singularity and thus to a faster decay. The leading singularity gives an expansion

$$
\frac{1}{\sqrt{1-u}} = \sum_{t=0}^{\infty} \frac{1}{2^{2t}} \frac{(2t)!}{(t!)^2} u^t , \qquad (4.4.16)
$$

which are precisely the binomial coefficients one expects from the random walk described by the first term in (4.4.1). The corrections g_n thus lead to a modification of the amplitude by a factor $3/2$, and they give rise to transients. The number $3/2$ is special for the uniform q-distribution that has $\eta_2 = 1/3$; in general it reads $\langle w^2 \rangle^* = \frac{1}{2(1-2\eta_2)}$. Using Stirlings formula for the factorials, we obtain as the leading behavior for $A_0^{(t)}$

$$
A_0^{(t)} \simeq \frac{1}{2(1-2\eta_2)} \frac{A_0^{(0)}}{\sqrt{\pi t}} , \qquad t \to \infty . \qquad (4.4.17)
$$

The asymptotic analysis for $z = 2$ is easily generalized. Defining the integral

$$
D(u) = \left(\frac{1}{2\pi} \right)^{d-1} \int_{BZ} d\mathbf{k} \, \frac{1}{1 - u\,\lambda(\mathbf{k})\lambda(-\mathbf{k})} , \qquad (4.4.18)
$$

we obtain for $A_0(u)$

$$
A_0(u) = A_0^{(0)} D(u) + \left(\frac{z^2\eta_2 - 1}{z - 1} \right) A_0(u) \left[1 - (1-u)D(u) \right] . \qquad (4.4.19)
$$

Comparing this with the results for $z = 2$, it is clear that the first term contains the diffusive singularity at $u = 1$; the integral for $D(u)$ develops a singular denominator for $u = 1$ at the point $\mathbf{k} = \mathbf{0}$. The type of singularity depends on the dimension $d-1$ of the $\mathbf{k}$ integral and thus on the dimension of the system. The singularity can be obtained by the saddle point method

using the approximation of Eq. (4.3.8) for $\lambda(\mathbf{k})$ and reads $(1 - u)^{(d-3)/2}$, where the power 0 means a logarithm (for the fcc packing). Consequently the decay is as $(1/\sqrt{t})^{(d-1)}$ for large t. The other terms in (4.4.19) give a modification of the amplitude by a factor $\langle w^2 \rangle^*$ and a faster decay term (due to a weaker singularity).

4.5   Modes of decay for $\mathcal{P}(\vec{w})$

4.5.1   Derivation of modes for product measure solutions

So far, we have discussed the relaxation of the second moments of $\mathcal{P}(\vec{w})$ towards their stationary values. In this section, we discuss the relaxation of the entire weight distribution, for the special q-distributions that lead to product measure solutions (Eq. (3.3.9)). For these q-distributions it is possible to derive the *modes* along which the stationary $\mathcal{P}^*(\vec{w})$ is approached. To do so, we again use Eq. (3.3.8), which we now write as

$$
\int \eta_r(\vec{q}) \delta \left(1 - \sum_\alpha q_\alpha \right) d\vec{q} \left(\frac{1}{1 + \lambda \sum_\alpha q_\alpha s_\alpha} \right)^{zr} = \prod_\alpha \left(\frac{1}{1 + \lambda s_\alpha} \right)^r .
$$

(4.5.1)

Here, the $\eta_r(\vec{q})$ represent the special q-distributions, and we have rescaled the Laplace variables s_α to λs_α.

Let us first briefly repeat the construction of the stationary states. If we apply the recursion to the (normalized) distribution

$$
\tilde{P}^*(\vec{s}) = \prod_i \left(\frac{1}{1 + \lambda s_i} \right)^{zr} ,
$$

(4.5.2)

we see from Eq. (4.5.1) that each (zr)th power splits up into z factors to the power r of the neighboring sites. The product over all sites in a layer then restores the (zr)th power of the denominator, which makes $\tilde{P}^*(\vec{s})$ an invariant. Putting the mean weight equal to 1 requires that $\lambda = 1/zr$, leading to the solutions of Eq. (3.3.11).

Further information is deduced by differentiation of Eq. (4.5.1) with

respect to λ, yielding

$$\int \eta_r(\vec{q})\delta\left(1 - \sum_\alpha q_\alpha\right) d\vec{q} \frac{\sum_\alpha q_\alpha s_\alpha}{(1 + \lambda \sum_\alpha q_\alpha s_\alpha)^{zr+1}}$$

$$= \frac{1}{z}\left(\prod_\alpha \frac{1}{1 + \lambda s_\alpha}\right)^r \sum_{\alpha'} \frac{s_{\alpha'}}{1 + \lambda s_{\alpha'}} \,. \tag{4.5.3}$$

This allows us to construct another invariant

$$\tilde{\mathcal{P}}_1^*(\vec{s}) = \tilde{\mathcal{P}}^*(\vec{s}) \sum_i \frac{s_i}{1 + \lambda s_i} \,. \tag{4.5.4}$$

Inserting this expression into the recursion of Eq. (3.2.7), we encounter the integral of Eq. (4.5.1) for all sites, except for site i where we have to perform the integral of the left hand side of Eq. (4.5.3). That produces factors with the power $zr + 1$ for a set of surrounding sites and the numerics is such that adding them together yields again a sum as in Eq. (4.5.4). It is not surprising that this additional invariant exists since we showed that Eq. (4.5.2) was invariant for arbitrary λ or scale of the weights. Thus the invariance of Eq. (4.5.4) is nothing else than expressing this scale invariance; in fact Eq. (4.5.4) follows directly from differentiating Eq. (4.5.2) with respect to λ. However, this invariant $\tilde{\mathcal{P}}_1^*(\vec{s})$ is not normalizable since its norm $\tilde{\mathcal{P}}_1^*(\vec{0}) = 0$.

It is rewarding to continue to differentiate Eq. (4.5.1) with respect to λ, yielding

$$\int \eta_r(\vec{q})\delta\left(1 - \sum_\alpha q_\alpha\right) d\vec{q} \frac{(\sum_\alpha q_\alpha s_\alpha)^2}{(1 + \lambda \sum_\alpha q_\alpha s_\alpha)^{zr+2}}$$

$$= \frac{1}{z(zr+1)}\left(\prod_\alpha \frac{1}{1 + \lambda b_\alpha}\right)^r \sum_{\alpha',\alpha''} \frac{s_{\alpha'}(r + \delta_{\alpha',\alpha''})s_{\alpha''}}{(1 + \lambda s_{\alpha'})(1 + \lambda s_{\alpha''})} \,. \tag{4.5.5}$$

Now the distribution

$$\tilde{\mathcal{P}}(\vec{s}) = \tilde{\mathcal{P}}^*(\vec{s}) \sum_i \left(\frac{s_i}{zr + s_i}\right)^2 \,, \tag{4.5.6}$$

is not invariant since the right hand side of Eq. (4.5.5) produces terms with powers $zr + 1$ of the denominator on two sites. As we argue below, Eq. (4.5.6) leads to the *slowest mode* decaying towards the stationary state.

4.5.2   The slowest mode

Let us now investigate how a deviation from $\tilde{\mathcal{P}}^*(\vec{s})$ will decay under recursion. We take an initial distribution of the type

$$\tilde{\mathcal{P}}(\vec{s}) = \tilde{\mathcal{P}}^*(\vec{s})[1 + \Delta\tilde{\mathcal{P}}(\vec{s})] \, , \qquad (4.5.7)$$

and in the spirit of the previous section we consider deviations of the form

$$\Delta\tilde{\mathcal{P}}(\vec{s}) = \sum_n A_n \tilde{Q}_n(\vec{s}) \, , \qquad (4.5.8)$$

where the $Q_n(\vec{s})$ are products of two factors

$$\tilde{Q}_n(\vec{s}) = \sum_i \left(\frac{s_i}{zr + s_i} \right) \left(\frac{s_{i+n}}{zr + s_{i+n}} \right) \, . \qquad (4.5.9)$$

It is clear from the previous section that, after the transformation, such a $\Delta\tilde{\mathcal{P}}(\vec{s})$ is again a sum over $\tilde{Q}_n(\vec{s})$:

$$\Delta\tilde{\mathcal{P}}'(\vec{s}) = \sum_n A_n' \tilde{Q}_n(\vec{s}) \, . \qquad (4.5.10)$$

The transformed coefficients A_n' are expressed in terms of the A_n of the previous layer, using the formulae of the previous section, as

$$A_n' = \sum_\gamma \Omega_\gamma(n - \gamma)A_{n-\gamma} \, , \qquad (4.5.11)$$

where

$$
\begin{aligned}
n = 0 \;\; &\Rightarrow \;\; \Omega_0(0) = \frac{r+1}{z(zr+1)} \qquad \Omega_{\gamma \neq 0}(0) = \frac{r}{z(zr+1)} \, , \\
n \neq 0 \;\; &\Rightarrow \;\; \Omega_\gamma(n) = \frac{1}{z^2} \, .
\end{aligned}
\qquad (4.5.12)
$$

This recursion of the coefficients of $\tilde{Q}_n(\vec{s})$ is exactly the same as the recursion of the second moments, as derived in Section 3.4: for the special q-distributions of Eq. (3.3.9), we have

$$\eta_2 = \frac{\Gamma(zr)\Gamma(r+2)}{\Gamma(r)\Gamma(zr+2)} = \frac{r+1}{z(zr+1)} \, , \qquad (4.5.13)$$

which makes the transition rates of Eq. (3.4.8) identical to the rates of Eq. (4.5.12). So, for the decay of $\Delta\tilde{\mathcal{P}}(\vec{s})$ we can simply take over the

conclusions of Section 4.4. Analogous to the discussion for the second moments, consider an initial condition where only $A_0^{(0)} \neq 0$. This is a minimal disturbance of the stationary state with only a modification of the single-site probability distribution and no correlations between sites.[2] The evolution of this deviation is exactly the same as that of the second moment of an arbitrary deviation from the stationary state. The difference is that we now have the relaxation of the full weight distribution. Projecting this joint distribution onto a single-site distribution, by putting all $s_i = 0$ except for one, one finds

$$\tilde{\mathcal{P}}^{(t)}(s) = \tilde{\mathcal{P}}^*(s) \left(1 + A_0^{(t)} \frac{s^2}{(zr+s)^2} \right) . \qquad (4.5.14)$$

So on the level of the single-site distribution the shape of the deviation remains invariant, but the amplitude decays as $A_0^{(t)} \sim \left(1/\sqrt{t} \right)^{d-1}$. This means that not only the second moment, but the whole single-site distribution relaxes towards the stationary state with a characteristic shape of the single-site distribution given by Eq. (4.5.14).

4.5.3 Higher moments and faster modes

In this section we show that higher moments lead to faster modes. The discussion for the higher moments is very similar to that of the second moments. The starting point is the master equation Eq. (3.4.9), which is a generalization of the equation for the second moments. It is, however, much more complicated: for the second moments all transition rates are equal except those leaving the origin, whereas for the higher moments there are also differing rates on special lines and planes in the correlation space (see Sections 3.4 and 3.6). From the analysis in Section 4.4 it is clear, however, that such localized corrections do not affect the *power* of the asymptotic decay. So, for the leading behavior we can simply consider ordinary diffusion with equal transition rates.

Consider the class of uncorrelated initial conditions that coincide with $\mathcal{P}^*(w)$ up to the second moment, but deviate at the level of the third moment. The difference of the third order moments with respect to the stationary state then only has a value for $k = l = 0$. Such a disturbance gradually spreads over the $2(d-1)$ dimensional space of the indices k and

---

[2]It is not a product distribution, but it can be seen as the linearization of a product distribution.

l (e.g. see Fig. 3.3). The decay is therefore as $(1/t)^{d-1}$ which is faster than the $\left(1/\sqrt{t}\right)^{d-1}$ of the slowest mode.

The same story holds for the construction of the higher modes. By further differentiation of Eq. (4.5.5), one derives the transformation law of the functions which have 3 factors of the type $s_i/(zr + s_i)$ extra over the stationary state. Such functions do not modify the normalisation, the mean weight and the second moment, and therefore couple to the decay of the third moment as we have described above. On the level of the single-site distribution the mode takes the form

$$\tilde{\mathcal{P}}^{(l)}(s) = \tilde{\mathcal{P}}^*(s) \left[1 + B_{0,0}^{(t)} \left(\frac{s}{zr + s} \right)^3 \right] , \qquad (4.5.15)$$

with the $B_{0,0}^{(t)} \sim (1/t)^{d-1}$.

The generalization to higher moments and faster modes is evident. On the level of the single site distribution it simply means a change of the power of the last factor in Eq. (4.5.15). The coefficient in front of a power m decays as $\left(1/\sqrt{t}\right)^{(d-1)(m-1)}$.

4.5.4   Simulation results

The question that emerges is: can one observe these modes in the relaxation of an actual simulation? This question is related to the problem of whether an arbitrary initial distribution can be decomposed as a superposition of these modes. Already on the level of the single site distribution one observes that our modes do not form a complete set in the mathematical sense. All modes start with a power w^{zr-1} in the weight distribution; hence the modes form a poor basis for the small w behavior. Nevertheless, the modes that we have constructed do describe the asymptotic decay. We should realize that before the asymptotic regime sets in, a fast process takes place. For a small resultant weight w'_j to occur, either the $q_{j-\alpha,\alpha}$ or the $w_{j-\alpha}$ have to be small. Already after one recursion step, an arbitrary initial probability density (in the single-site distribution) will be replaced by a probability density starting as w^{zr-1} (modulo logarithmic factors, which move to higher orders in the next recursion steps). Thus after a few steps, the decay of the probability distribution can be well described by the above constructed modes.

In order to test the mode picture we have performed numerical simulations on the 2-dimensional triangular packing and the 3-dimensional fcc

packing, using the uniform q-distribution. We took the initial condition $w_i = 1$ for each site i, which also means $\langle w_i^2 \rangle = 1$. This initial distribution is a substantial deviation from the stationary state, i.e. Eq. (3.3.11) with $r = 1$. In Fig. 4.2 we have compared the numerically obtained single-site distributions with the analytical results. In the Fig. 4.2a, we show the single-site weight distribution of the $t = 50$th layer in the triangular packing, after subtracting $\mathcal{P}^*(w)$. The analytical curve (solid line) is the slowest mode Eq. (4.5.14), whose amplitude has been computed from the recursive scheme of Eq. (4.5.11), with the initial value $A_0^{(0)} = -1$, corresponding to the initial second moment $\langle w_i^2 \rangle = 1$. As the comparison with the numerical result (dotted line) does not involve any free parameters the correspondence is remarkable; the more so since the deviations bear the signature of the next slowest mode Eq. (4.5.15). In Fig. 4.2b, the simulation data is shown for the fcc packing with the same initial distribution and $t = 10$. In line with the fact that the modes decay faster in a higher dimension, the agreement is even more impressive.
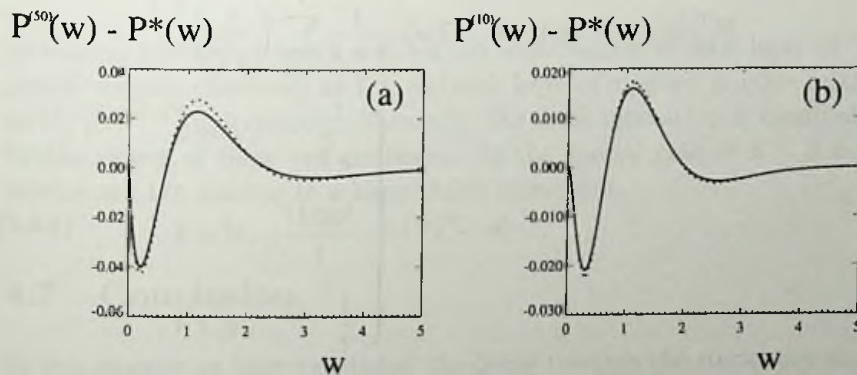

Figure 4.2: Comparison of the slowest mode of Eq. (4.5.14) (solid lines) with numerical simulations (dotted lines) for *(a)* the triangular packing ($z = 2$) at $t = 50$, and *(b)* the fcc packing ($z = 3$) at $t = 10$.

4.6   Influence of injection

After this detailed analysis of the relaxation without the injection term $mg = 1$ in Eq. (1.4.3), we now investigate how this injection affects the relaxation process. Let us remark that the discussion below is more qual-

itative than those of the preceding sections, and based on numerical simulations.

An important observation is that the recursive relation for the weights, Eq. (1.4.3), is a *linear* equation. The q-model with injection can therefore be interpreted as a superposition of q-models without injection, with differently positioned initial layers. Although it is not a priori clear how this superposition property is reflected in the weight distributions $\mathcal{P}_{\text{inj}}^{(t)}(w)$ (with injection) and $\mathcal{P}^{(t)}(w)$ (without injection), we propose the following approximate mapping:

$$\mathcal{P}_{\text{inj}}^{(t)}(w) = \frac{1}{t+1} \sum_{t'=0}^{t} \mathcal{P}^{(t')}(w) \ . \tag{4.6.1}$$

If we combine this with the result of Eq. (4.5.14), we obtain the following relaxation as $t \to \infty$:

$$\mathcal{P}_{\text{inj}}^{(t)}(w) - \mathcal{P}^*(w) \ \propto \ \mathcal{F}(w) \ \frac{1}{t+1} \sum_{t'\neq 0}^{t} \left(\frac{1}{\sqrt{t'}} \right)^{d-1}$$

$$\propto \ \mathcal{F}(w) \begin{cases} \dfrac{1}{\sqrt{t}} & , d = 2 \\[2mm] \dfrac{\log(t)}{t} & , d = 3 \\[2mm] \dfrac{1}{t} & , d \geq 4 \ , \end{cases} \tag{4.6.2}$$

where $\mathcal{F}(w)$ is the inverse Laplace transform of $\tilde{P}^*(s)\, s^2/(zr+s)^2$; see Eq. (4.5.14). This behavior is indeed observed for the relaxation of the second moments in numerical simulations with $d = 2$ and $d = 3$, using a uniform q-distribution. In Fig. 4.3, we show the results for an fcc packing ($d = 3$). We plot $t \times |\langle w^2 \rangle^{(t)} - 4/3|$ as function of depth t, where $\langle w^2 \rangle^{(\infty)} = 4/3$. The climbing straight line on the lin-log plot confirms the remarkable $\log(t)/t$ relaxation. We also plot the same data for the q–model without injection; this curve becomes flat in agreement with Eq. (4.4.17).

Although the mapping of Eq. (4.6.1) is definitely not exact, it apparently captures the main physics of the relaxation process. This can be understood as follows. There are two slow processes involved: *(i)* the
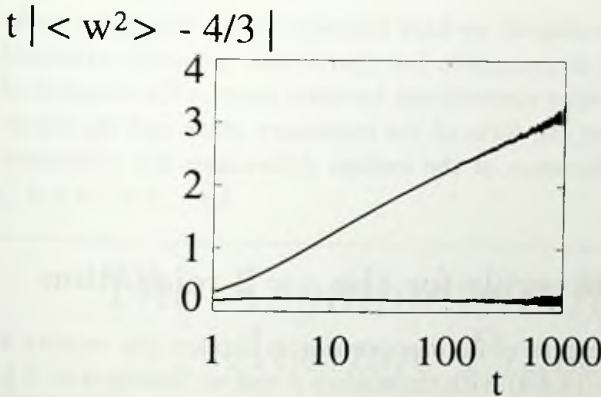
$$t \, | <w^2> \, - \, 4/3 \, |$$

Figure 4.3: Relaxation of the second moments with injection (climbing line) and without injection (flat line) towards their asymptotic values 4/3. The climbing straight line confirms the $\log(t)/t$ relaxation for the q-model with injection; without injection the relaxtion is simply $1/t$.

increasing number of layers reduces the contribution of each layer of 'injected' weights effectively as $1/t$; *(ii)* each layer of injected weights relaxes as $(1/\sqrt{t})^{(d-1)}$ individually. Naturally, the total relaxation is dominated by the slower of these two processes. In the special case of $d = 3$ both powers are $1/t$, leading to a logarithmic correction.

4.7 Conclusion

In this chapter we have calculated the decay towards the stationary state $\mathcal{P}^*(w)$ in the q-model, starting from arbitrary initial weight distributions that have short-ranged weight correlations. Since we can fix the average weight, the relaxation occurs for the second and higher order weight moments. The short-ranged correlations become longer ranged while their amplitudes diminish in a diffusion process in correlation space. This accounts for the slow algebraic relaxation of the second moments of the weight. These moments also dictate the slowest modes of relaxation of the full distribution function. For the special class of q-distributions of Eq. (3.3.9) we have derived the asymptotic form of Eq. (4.5.14) for the relaxation of the single-site distribution from arbitrary initial conditions. Furthermore, we have shown how the injection term affects the relaxation

– see Eq. (4.6.2). In this chapter we have focussed on the triangular packing and the fcc packing as examples, but the results are easily extended to other packings and other connections between layers. The number of connections z determines the form of the stationary state and the decay modes, whereas the dimension of the system determines the relaxation powers of the modes.

4.A   Contour integrals for the $z = 2$ relaxation

For the triangular packing ($z = 2$), one can simply replace the vectors $\mathbf{k}$ and $\mathbf{r}_n$ appearing in Eq. (4.4.4) with the scalars k and n. Taking $\alpha = \pm\frac{1}{2}$, the transmission function becomes

$$\lambda(k) = \frac{1}{2}\left(e^{ik/2} + e^{-ik/2}\right) , \tag{4.A.1}$$

hence

$$\lambda(k)\lambda(-k) = \frac{1}{4}\left(e^{ik} + 2 + e^{-ik}\right) . \tag{4.A.2}$$

To obtain a closed relation for $A_0(u)$, we Fourier invert Eq. (4.4.11) at $n = 0$. The left hand side becomes the sought for $A_0(u)$. The terms on the right hand side with denominator $1 - u\lambda(k)\lambda(-k)$ can be obtained by contour integration over the unit circle, using the transformation $v = e^{ik}$:

$$\begin{aligned}
\int_0^{2\pi} \frac{dk}{2\pi} \frac{1}{1 - u\lambda(k)\lambda(-k)} &= \frac{1}{2\pi i} \oint \frac{dv}{v} \frac{1}{1 - \frac{u}{4}(v + 2 + 1/v)} \\
&= -\frac{1}{2\pi i} \frac{4}{u} \oint dv \frac{1}{(v - v_+)(v - v_-)} ,
\end{aligned} \tag{4.A.3}$$

where the poles $v_\pm$ are

$$v_\pm = \frac{2}{u}\left(1 - \frac{1}{2}u \pm \sqrt{1 - u}\right) . \tag{4.A.4}$$

Since only v_- lies within the unit circle, the outcome of the integral becomes

$$-\frac{1}{2\pi i} \frac{4}{u}\left(2\pi i \frac{1}{v_- - v_+}\right) = \frac{1}{\sqrt{1 - u}} , \tag{4.A.5}$$

which results into Eq. (4.4.13).

The Asymmetric Random Average Process

5.1 Introduction

In this chapter we apply the techniques and results derived for the q-model to the so-called Asymmetric Random Average Process (ARAP). The ARAP is a non-equilibrium model for one-dimensional interacting particles moving on a continuous line. Although many studies have been devoted to systems of particles moving on a discrete lattice, like for example the asymmetric exlusion process [73, 74], there are only a few analytical results for particle systems on the real line [71, 75, 76]. Some of these results actually originate from a mapping between the q-model and the ARAP. Along this line, we extend our results of the previous chapters to the ARAP, leading to interesting features that are not present in the q-model.

Let us first define the model and show the connection to the q-model. In the ARAP, one considers particles with positions $x_i \in \mathbb{R}$, which move to the right without passing one another. In an elementary movement, particle i jumps to a position $x_i + \delta_i$ between x_i and the particle ahead at $x_{i+1} > x_i$, as depicted schematically in Fig. 5.1. The large scale dynamics of such a system depends very much on the local dynamics, i.e. how the jumps δ_i are chosen. In models for traffic flow, for example, these jumps typically depend on velocity and on available space in front of a car [77]. In order to perform an analytical study we restrict ourselves to a very
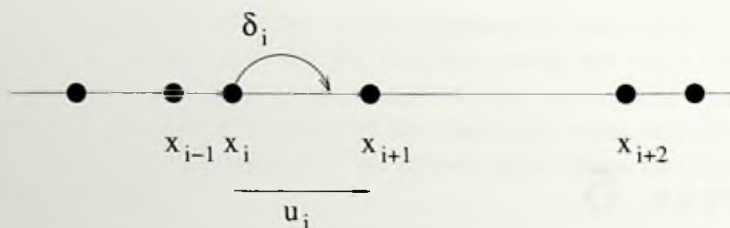
Figure 5.1: In the ARAP, particles move in one direction on a continuous line. A particle at position x_i jumps to a position $x_i + \delta_i$, where δ_i can not exceed the headway u_i.

simple update rule, for which the length scale for δ_i solely depends on the *headways* defined by $u_i = x_{i+1} - x_i$. So, the δ_i are generated from a distribution

$$P(\delta_i \,; u_i) = \frac{1}{u_i}\, \eta\left(\delta_i/u_i\right) \;. \tag{5.1.1}$$

It is convenient to introduce the notation $q_i = \delta_i/u_i$. Since particles can only move to the right, we have $q_i \geq 0$, and the hard-core particle interaction ensures that $q_i < 1$. If all positions x_i are updated simultaneously, we can write

$$\begin{aligned} x'_{i+1} &= x_{i+1} + q_{i+1}u_{i+1} \\ x'_i &= x_i + q_i u_i \;, \end{aligned} \tag{5.1.2}$$

which after subtraction yields

$$u'_i = q_{i+1}u_{i+1} + (1 - q_i)\, u_i \;. \tag{5.1.3}$$

So, we have obtained a recursion relation for the headways u_i that is obviously identical to the recursion of the weights w_i in the q-model on a triangular lattice. In the case of the ARAP, however, there is no reason to treat the fractions q_i and $1 - q_i$ in a symmetrical manner, like we did in the q-model. The fraction q_i corresponds to a jump forward, whereas $1 - q_i$ represents the remainder of the headway u_i after the jump of particle i. We therefore allow for asymmetric q-distributions $\eta(q) \neq \eta(1 - q)$, which gives some interesting new physics to the problem of the q-model.

It is clear that the recursion of Eq. (5.1.3) holds for a so-called *parallel update*, where all particle positions are updated simultaneously. However, one can use it for a *random sequential update* scheme as well, in which

particles move one by one in a random order [76]. In the following section we investigate the existence of uncorrelated stationary probability distributions for both types of updates. We then calculate the correlation functions for q-distributions that do not lead to stationary product measures.

5.2 Stationary states in the ARAP

5.2.1 Parallel update

We have seen that the ARAP with parallel update is mathematically equivalent to the q-model on a triangular lattice with asymmetric $\eta(\vec{q})$. In order to investigate the existence of stationary product measures in the ARAP, we can thus simply follow the analysis of Sec. 3.3, but allow for asymmetries in the arguments of $\eta(\vec{q})$. The crucial step in the derivation of the criterion for factorization, Eq. (3.3.7), was that the function $\tilde{\psi}(s_{i+\alpha_1}, \cdots, s_{i+\alpha_z})$ factorizes into identical $\tilde{\psi}(s_{i+\alpha})$. From Eq. (3.3.3) one sees that the arguments of this function are coupled to the $q_{i,\alpha}$; for asymmetric $\eta(\vec{q})$ the function may therefore factorize in an asymmetrical manner as

$$\tilde{\psi}(s_{i+\alpha_1}, \cdots, s_{i+\alpha_z}) = \prod_\alpha \tilde{\psi}_\alpha(s_{i+\alpha}) , \qquad (5.2.1)$$

where the $\tilde{\psi}_\alpha(s)$ can differ for each α (compare with Eq. (3.3.5)). The corresponding single-site $\tilde{\mathcal{P}}^*(s_j)$ reads

$$\tilde{\mathcal{P}}^*(s_j) = \prod_\alpha \tilde{\psi}_\alpha(s_j) . \qquad (5.2.2)$$

The criterion for factorization thus becomes that for a given $\eta(\vec{q})$, there are functions $\tilde{\psi}_\alpha(s)$ that obey

$$\int \eta(\vec{q}) \delta \left(1 - \sum_\alpha q_\alpha \right) d\vec{q} \prod_\alpha \tilde{\psi}_\alpha \left(\sum_\alpha q_\alpha s_\alpha \right) = \prod_\alpha \tilde{\psi}_\alpha(s_\alpha) . \qquad (5.2.3)$$

It is again possible to construct a special class of $\eta(\vec{q})$ that obey this criterion and thus lead to uncorrelated weight distributions. We make use of a generalization of Eq. (3.3.8): the results are obtained by replacing r with r_α, and zr with $\sum_\alpha r_\alpha$ in Eqs. (3.3.8)-(3.3.11). For the ARAP, where the arguments q_α are simply q and $1 - q$, we thus obtain

$$\eta(q) = \frac{\Gamma(r_1 + r_2)}{\Gamma(r_1)\Gamma(r_2)} \, q^{r_1 - 1} (1 - q)^{r_2 - 1} \, , \qquad r_1, r_2 > 0 \, , \qquad (5.2.4)$$

for which

$$\tilde{\psi}_{1,2} = \frac{1}{(1 + s)^{r_{1,2}}} \, , \qquad (5.2.5)$$

leading to the following stationary product measures:

$$\mathcal{P}^*(w) = \frac{a^a}{\Gamma(a)} \, w^{a-1} \, e^{-aw} \qquad \text{with} \qquad a = r_1 + r_2 \, . \qquad (5.2.6)$$

So, allowing for asymmetric $\eta(q)$ has extended the class of solutions from a one-parameter set to a two-parameter set. All other q-distributions again give rise to correlations, as will be discussed in Sec. 5.3.

5.2.2   Random sequential update

We now study the ARAP with random sequential update dynamics: at each time step, only one randomly selected particle i will jump a distance $\delta_i = q_i u_i$, with q_i chosen from some distribution $\phi(q_i)$. We first argue that one obtains this random sequential dynamics by using a distribution of the type[1]

$$\hat{\eta}(q_i) = (1 - p) \, 2\delta(q_i) + p \, \phi(q_i) \, , \qquad (5.2.7)$$

in the limit $p \ll 1/N$ with a parallel update; here N indicates the number of particles in the system. In this limit, one can approximate the joint q-distribution, i.e. the product of the $\hat{\eta}(q_i)$, as

$$\prod_{i=1}^{N} \hat{\eta}(q_i) \simeq (1 - Np) \prod_{i=1}^{N} 2\delta(q_i) + \sum_{i=1}^{N} p \, \phi(q_i) \prod_{j \neq i} 2\delta(q_j) \, . \qquad (5.2.8)$$

This means that for most recursion steps there is no particle motion at all; there is only a probability $Np \to 0$ that a randomly selected particle moves, with a q_i chosen from $\phi(q_i)$. The probability of two particles moving simultaneously is $N(N-1)\,p^2/2$ and can thus be neglected. So, using $\hat{\eta}(q)$ of Eq. (5.2.7) with a parallel update in the limit $p \ll 1/N$ is indeed equivalent to using $\phi(q)$ with a random sequential update. One can also

---

[1] The contribution of $\delta(q_i)$ to the norm is only $1/2$, since $\hat{\eta}(q_i)$ is defined on $[0, 1)$.

interpret this random sequential update as a continuous time dynamics, by taking $p = \Delta t$.

The statistics of the headways in the ARAP depends very much on the type of update that is used. This has been illustrated by Rajesh and Majumdar [76] for the uniform q-distribution: within a mean-field approximation, they found for the random sequential update

$$\mathcal{P}^*(u) = \frac{1}{\sqrt{2\pi u}} \, e^{-u/2} \; , \qquad (5.2.9)$$

which is very different from the solution for the parallel update, i.e. $\mathcal{P}^*(u) = 4 \, u \, e^{-2u}$. Remarkably enough, the mean-field result Eq. (5.2.9) is of the same form as the product measure solution of Eq. (5.2.6) with $a = 1/2$. This raises the question of whether stationary product measures may exist for the random sequential update. In other words:

Is there some $\phi(q)$ for which $\hat{\eta}(q)$ of Eq. (5.2.7) leads to a product measure solution in the limit $p \to 0$?

At first sight this may seem impossible, since $\hat{\eta}(q)$ does not lie within the special class of Eq. (5.2.4) for which factorization occurs. In the limit $r_1 \to 0$, however, these special q-distributions diverge as $1/q$ and the q-values thus become increasingly concentrated around 0, just like for $\delta(q)$. If now all moments of $\hat{\eta}(q)$ approach those of Eq. (5.2.4) in the limit $p, r_1 \to 0$, the 'amplitude' of the correlations will go to zero for the random sequential update with $\phi(q)$. The strategy is thus to equate the moments of $\hat{\eta}(q)$ and $\eta(q)$ of Eq. (5.2.4); we will show below that this leads to unphysical distributions $\phi(q)$, so we will conclude that there are no stationary product measures in the ARAP with random sequential update.

Zielen and Schadschneider demonstrated that if a given $\eta(q)$ leads to an uncorrelated stationary state, all higher moments are *uniquely* defined by η_1 and η_2 [71]. From Eq. (5.2.4), one can show that these moments can be obtained from the recursion

$$\eta_{n+1} = \frac{r_1 + n}{r_1 + r_2 + n} \, \eta_n \; , \qquad (5.2.10)$$

with the normalization condition

$$\eta_0 = 1 \; . \qquad (5.2.11)$$

In order to obey the general moment property $1 > \eta_1 > \eta_2 \geq \eta_1^2$, we have to take $r_1, r_2 > 0$. On the other hand, one can write the moments of Eq. (5.2.7) as

$$\hat{\eta}_n = p\,\phi_n + (1-p)\,\delta_{n,0}\;, \qquad (5.2.12)$$

where ϕ_n are the moments of $\phi(q)$. Now, if all moments $\hat{\eta}_n$ approach those produced by the recursion of Eq. (5.2.10) in the limit $p \to 0$, then all correlations will indeed vanish for $\phi(q)$ with a random sequential update.

Let us start the analysis by identifying the first moments, i.e.

$$p\phi_1 = \frac{r_1}{r_1 + r_2}\;. \qquad (5.2.13)$$

As anticipated above, the limit $p \to 0$ indeed implies[2] $r_1 \to 0$. We can thus write

$$\phi_1 = \left(\frac{r_1}{p}\right)\frac{1}{r_2} + \mathcal{O}(r_1)\;, \qquad (5.2.14)$$

so we have to take the limit $p, r_1 \to 0$ with a fixed ratio r_1/p. Imposing the recursion of Eq. (5.2.10) to the higher moments of $\hat{\eta}(q)$, one finds in this limit

$$\phi_{n+1} = \frac{n}{r_2 + n}\,\phi_n\;, \qquad (5.2.15)$$

yielding

$$\phi_n = \begin{cases} 1 & ,\, n = 0 \\ \dfrac{(n-1)!\,\Gamma(r_2+1)}{\Gamma(r_2+n)}\,\phi_1 & ,\, n \geq 1 \end{cases}\;. \qquad (5.2.16)$$

However, we shall now demonstrate that there is no probability density function $\phi(q)$ that produces this series, for any value of $0 < \phi_1 < 1$ and $r_2 > 0$. We first introduce the generating function

$$\tilde{\phi}(s) = \sum_{n=0}^{\infty} \frac{(-s)^n}{n!}\,\phi_n\;. \qquad (5.2.17)$$

We can extend $\phi(q)$ to the interval $[0,\infty)$ by taking $\phi(q) = 0$ for $q \geq 1$. The generating function then becomes equivalent to the Laplace transform of $\phi(q)$:

$$\int_0^\infty dq\,\phi(q)\,e^{-sq} = \sum_{n=0}^{\infty} \frac{(-s)^n}{n!}\int_0^1 dq\,q^n\,\phi(q) = \tilde{\phi}(s)\;, \qquad (5.2.18)$$

---

[2]The limit $r_2 \to \infty$ leads to $\phi_n = 0$ for all $n \geq 1$, which corresponds to $\phi(q) = 2\delta(q)$ and hence no particle motion at all.

provided that the series converge. Since $\phi(q)$ represents a probability density it can not be negative, and therefore, its Laplace transform $\tilde{\phi}(s)$ must also be positive for each value of s. However, we show below that

$$\tilde{\phi}(s) \simeq -\phi_1 \, r_2 \, \ln(s) \, , \tag{5.2.19}$$

for large s, so $\phi(q)$ can not be a probability density.

To arrive at this result, we write the derivative

$$\begin{aligned}
\frac{d}{ds}\tilde{\phi}(s) &= -\phi_1\Gamma(r_2+1) \sum_{n=1}^{\infty} \frac{\Gamma(n)\,(-s)^{n-1}}{(n-1)!\,\Gamma(r_2+n)} \\
&= -\phi_1\Gamma(r_2+1) \sum_{n=0}^{\infty} \frac{\Gamma(n+1)\,(-s)^n}{n!\,\Gamma(r_2+1+n)} \\
&= -\phi_1 \, M\,(1, r_2+1, -s) \, , \tag{5.2.20}
\end{aligned}$$

where $M\,(1, r_2+1, -s)$ is a Kummer function. For large s, this Kummer function is known to behave as [78]

$$M\,(1, r_2+1, -s) \simeq \frac{r_2}{s} \, , \tag{5.2.21}$$

from which one derives Eq. (5.2.19).

Let us briefly recapitulate. We have shown that there is no distribution $\phi(q)$ that leads to an uncorrelated stationary state within a random sequential update. We used Eq. (5.2.7) within a parallel update in the limit $p \to 0$; all correlations vanish if the moments of this distribution obey the recursion of Eq. (5.2.10). This gives the moments of $\phi(q)$, Eq. (5.2.16), but we have demonstrated that these moments do not correspond to a strictly positive probability density function.

5.3 Correlations in the ARAP

Let us now calculate the correlation functions appearing in the ARAP. We proceed as in Secs. 3.4 - 3.6, by studying the stationary solution of the master equation for the moments Eq. (3.4.9). We first repeat this equation:

$$M'_n(\mathbf{r}) - M_n(\mathbf{r}) =$$
$$\sum_{\gamma} \Omega_\gamma(\mathbf{r}-\gamma)\,M_n(\mathbf{r}-\gamma) - \Omega_{-\gamma}(\mathbf{r})\,M_n(\mathbf{r}) \, , \tag{5.3.1}$$

with the nth order moments,

$$M_n(\mathbf{r}) = M_n(k_1, \cdots, k_{n-1}) = \langle u_i u_{i+k_1} \cdots u_{i+k_{n-1}} \rangle , \qquad (5.3.2)$$

the 'transition rates',

$$\Omega_\gamma(\mathbf{r}) = \overline{q_{i,\alpha} q_{i+k_1,\alpha_1} \cdots q_{i+k_{n-1},\alpha_{n-1}}} , \qquad (5.3.3)$$

and the 'jump vectors',

$$\gamma = (\alpha_1 - \alpha, \alpha_2 - \alpha, \cdots, \alpha_{n-1} - \alpha) .$$

Since for the ARAP we can take $\eta(q) \neq \eta(1-q)$, the transition rates $\Omega_\gamma(\mathbf{r})$ have a different symmetry than the rates in the q-model. In this section we show how this affects the correlation functions.

5.3.1   Second order moments: no correlations

Let us first consider the stationary solution of the master equation for the second order moments, i.e. $n = 2$. In the ARAP there are only two different q-values per site, so we can conveniently choose the displacements α to be $\pm\frac{1}{2}$. The q-values will be referred to as $q_{i,+\frac{1}{2}}$ and $q_{i,-\frac{1}{2}} = 1 - q_{i,+\frac{1}{2}}$, and γ can take the values $-1, 0, +1$. The q-averages defining the transition rates can be expressed in terms of

$$\eta_1 = \overline{q_{i,+\frac{1}{2}}} \qquad \text{and} \qquad \eta_2 = \overline{q^2_{i,+\frac{1}{2}}} , \qquad (5.3.4)$$

as[3]

$$\Omega_{0+}(k) = \overline{q_{i,+\frac{1}{2}} \, q_{i+k,+\frac{1}{2}}} = \begin{cases} \eta_2 & , k = 0 \\ \eta_1^2 & , k \neq 0 \end{cases} \qquad (5.3.5)$$

$$\Omega_{0-}(k) = \overline{q_{i,-\frac{1}{2}} \, q_{i+k,-\frac{1}{2}}} = \begin{cases} 1 - 2\eta_1 + \eta_2 & , k = 0 \\ (1 - \eta_1)^2 & , k \neq 0 \end{cases} \qquad (5.3.6)$$

$$\Omega_{\pm 1}(k) = \overline{q_{i,\mp\frac{1}{2}} \, q_{i+k,\pm\frac{1}{2}}} = \begin{cases} \eta_1 - \eta_2 & , k = 0 \\ \eta_1 - \eta_1^2 & , k \neq 0 . \end{cases} \qquad (5.3.7)$$

---

[3]In the q-model we necessarily encountered $\eta_1 = 1/2$ due to the symmetry of $\eta(q)$.

For the second order moments it is possible to construct a simple detailed balance solution; the detailed balance condition of Eq. (3.5.1) reads

$$\langle u_i u_{i+k} \rangle = \frac{\Omega_{+1}(k-1)}{\Omega_{-1}(k)} \langle u_i u_{i+k-1} \rangle \ .$$
(5.3.8)

for all k. Putting $\langle u_i u_{i+k} \rangle = 1$ for $k \neq 0$, we find:

$$\langle u_i u_{i+k} \rangle = \begin{cases} \dfrac{\eta_1 - \eta_1^2}{\eta_1 - \eta_2} & , k = 0 \\ 1 & , k \neq 0 \ . \end{cases}$$
(5.3.9)

Hence, there will be no second order correlations in the ARAP, as was already pointed out by Krug and Garcia [75].

5.3.2 Third order correlations

Like in the q-model, the third order moments $\langle u_i u_{i+k} u_{i+l} \rangle$ diffuse on the triangular lattice depicted in Fig. 3.3. The transition rates for this diffusion involve averages over three q-values. In Sec. 3.6 it was pointed out that the transitions with $\gamma = 0$ are not important for the stationary solution of the master equation. The $\gamma \neq 0$ involve two $\alpha = +\frac{1}{2}$ and one $\alpha = -\frac{1}{2}$, or vice versa; we denote these as γ^+ and γ^- respectively. It is important to explicitly distinguish between γ^+ and γ^- since we allow for asymmetric q-distributions so that $\Omega_{\gamma^+}(\mathbf{r}) \neq \Omega_{\gamma^-}(\mathbf{r})$. Fig. 5.2 shows how the various γ relate to $\{\alpha, \alpha', \alpha''\}$.

Let us first analyze the solutions corresponding to the special $\eta(q)$ of Eq. (5.2.4). The stationary moments for these q-distributions are simply $\langle u_i \rangle = 1$ in the bulk, $\langle u_i^2 \rangle$ at the lines, and $\langle u_i^3 \rangle$ at the origin. However, unlike in the q-model this is *not* a detailed balance solution. Each bond corresponds to a γ^+ and a $\gamma^- = -\gamma^+$, and for example in the bulk we find $\Omega_{\gamma^+} \neq \Omega_{\gamma^-}$, unless $\eta_1 = 1/2$. In general, there will thus be a *flow* along all bonds in the plane, either in the three γ^+ or in the three γ^- directions (Fig. 5.3). In the absence of correlations, the moments are independent of the distance from the origin; this can only be accomplished by having a constant flow on each bond.

Let us now rewrite the stationary master equation of the moments as

$$0 = \sum_\gamma \Omega_\gamma(\mathbf{r}-\gamma) M(\mathbf{r} - \gamma) - \Omega_\gamma(\mathbf{r}) M(\mathbf{r}) \ .$$
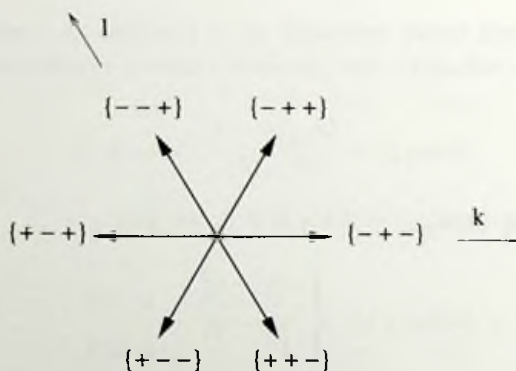(5.3.10)

Figure 5.2: The various jump directions γ^+ and γ^- in the space spanned by k and l. Each γ originates from the indicated combination of $\{\alpha, \alpha', \alpha''\}$.
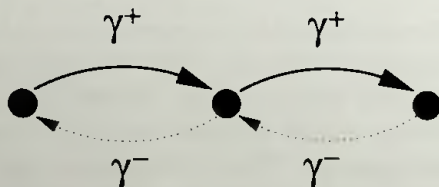

Figure 5.3: Due to the asymmetry $\Omega_{\gamma^+} \neq \Omega_{\gamma^-}$, there will be a resultant flow along each bond. Although this is not a detailed balance solution, the moments can become uncorrelated, i.e. independent of distance from the origin, if the amount of flow is the same at each bond.

One can easily understand that for a solution of constant flow, each term on the right hand side vanishes individually: at a position $\mathbf{r}$, each contribution coming from $\mathbf{r} - \gamma$ is equal to what is given to $\mathbf{r} + \gamma$ (see again Fig. 5.3). Note the subtle difference with a detailed balance solution, where all terms vanish if the indices of the transition rates are *opposite* (γ and $-\gamma$) instead of equal.

So, there are no correlations if all terms in the sums of Eq. (5.3.10) vanish individually. We refer to these as *conditions for constant flow*. For the value at the origin $M(0) = \langle u_i^3 \rangle$, there are two a priori different conditions, corresponding to γ^+ and γ^- respectively. These two conditions

become equivalent if the q-moments obey

$$\eta_3 = \frac{\eta_2 \left(\eta_2 \eta_1 + \eta_1^2 - 2\eta_2\right)}{2\eta_1^2 - \eta_1 - \eta_2}, \tag{5.3.11}$$

which is of course the case for the q-distributions of Eq. (5.2.4). It is easily verified that all symmetric $\eta(q)$ obey this relation as well, since then, there is no difference between γ^+ and γ^-.

What happens if the conditions of constant flow are not obeyed? As shown in Sec. 3.6, one can obtain the leading behavior by ignoring the differing transition rates at the lines, but keeping the differences at the origin. The transition rates can then be written as

$$\Omega_{\gamma\pm}(\mathbf{r}) = \frac{1}{6} \pm \varepsilon_1 \delta(\mathbf{r}) \pm \varepsilon_2, \tag{5.3.12}$$

where ε_2 represents the $\pm$ asymmetry for the bulk rates and ε_1 accounts for the differing rates at the origin. The latter prohibits a solution of constant flow. Furthermore, we eliminated the self-rates and the rescaled moments will be referred to as $\hat{M}(\mathbf{r})$ (see Sec. 3.6). We solve the corresponding stationary master equation by means of Fourier transformation:

$$\hat{M}(\mathbf{r}) = c + \varepsilon_1 \hat{M}(0) \sum_{\mathbf{k}} \frac{E(\mathbf{k}) \exp(-i\mathbf{k} \cdot \mathbf{r})}{1 - D(\mathbf{k}) - \varepsilon_2 E(\mathbf{k})}, \tag{5.3.13}$$

where c is a constant that is approached as $\mathbf{r} \to \infty$. The functions $D(\mathbf{k})$ and $E(\mathbf{k})$ are defined as

$$D(\mathbf{k}) = \frac{1}{6} \sum_{\gamma} \exp\left(i\mathbf{k} \cdot \gamma\right) = 1 - \frac{1}{4}k^2 + \cdots, \tag{5.3.14}$$

$$E(\mathbf{k}) = \sum_{\gamma\pm} \pm \exp\left(i\mathbf{k} \cdot \gamma^\pm\right) = \frac{i}{4}\left(k_x^3 - 3k_x k_y^2\right) + \cdots. \tag{5.3.15}$$

To obtain the large $\mathbf{r}$ behavior one can neglect the term proportional to ε_2 in Eq. (5.3.13), since for small $\mathbf{k}$ we find $1 - D(\mathbf{k}) \sim k^2$ and $E(\mathbf{k}) \sim \mathcal{O}(k^3)$. The sum in Eq. (5.3.13) then simplifies to a solution of Poisson's equation: the leading behavior comes from the lowest cylindrical harmonic obeying the symmetry of the problem, i.e. $\cos(3\phi)/r^3$.

We thus find that correlations in the ARAP already occur at third order due to the asymmetry in $\eta(q)$, and that these correlations decay

as $1/r^3$. Since these correlations are substantially stronger than in the q-model, we have tried to confirm this result numerically, using

$$\eta(q) = 0.95\, \delta\,(q - 0.1) + 0.05\, \delta\,(q - 0.9) \ . \qquad (5.3.16)$$

We calculated $M(k,0) = \langle u_i^2 u_{i+k}\rangle$ and $M(k,k) = \langle u_i u_{i+k}^2\rangle$, which correspond to the lines $l = 0$ and $k = l$ in the two dimensional correlation space. Fig. 5.4a shows that these moments slowly decay towards $\langle u_i^2\rangle = 301/225 \approx 1.338$ as a function of the distance k. In agreement with the $\cos(3\phi)$ proportionality, the curves approach this value from a different side. In order to verify the $1/k^3$ law, we also plotted the differences with the asymptotic value on a log-log plot in Fig. 5.4b. Although the noise level is already reached after one decade[4], the data are consistent with the calculated $1/k^3$ law.
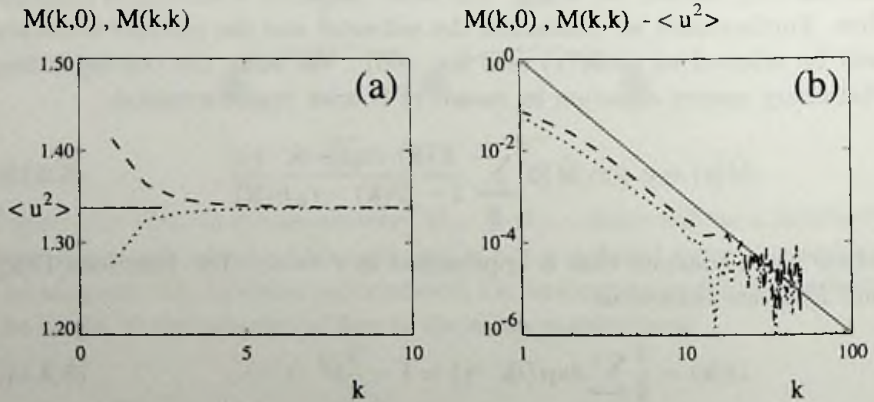
Figure 5.4: *(a)* Third order moments $M(k,0)$ (dotted) and $M(k,k)$ (dashed) as a function of k. *(b)* The differences $|M(k,0) - \langle u_i^2\rangle|$ and $|M(k,k) - \langle u_i^2\rangle|$ on a logarithmic plot: third order correlations decay as $1/k^3$.

---

[4]Due to the slow relaxation towards the stationary solution, it is difficult to reduce the noise level. Our results were obtained by averaging over 10^3 independent realizations of the ARAP with 10^4 particles and 10^6 timesteps. For each realization, the stationary values M^* were estimated by extrapolating $M(t) = M^* + A/\sqrt{t}$

5.4   Conclusion

Although many aspects of the Asymmetric Random Average Process are similar to those of the q-model, we encountered some interesting new features in this chapter. Firstly, the ARAP allows for different update schemes, like the random sequential update. We have shown that this random sequential procedure always leads to correlations in the headways u_i, which are the separations between two neighboring particles. These correlations show up at the third order moments like $\langle u_i^2 u_{i+k} \rangle$, and decay as $1/k^3$, which is different from the q-model.

These correlations are also present in the ARAP with a parallel update, except for the class of q-distributions given by Eq. (5.2.4). Due to the asymmetry between q and $1-q$, this class is a two-parameter family instead of the one-parameter family of the q-model. These asymmetric q-distributions lead to remarkable solutions of the master equation of the moments. The asymmetry prohibits a detailed balance solution, but instead, there are solutions of 'constant flow': at each position $\mathbf{r}$, the contribution coming from $\mathbf{r} - \boldsymbol{\gamma}$ is equal to what is given to $\mathbf{r} + \boldsymbol{\gamma}$. Writing the master equation in the form Eq. (5.3.10), all terms vanish individually.

Towards a microcanonical-like approach to force networks

6.1   Introduction

In Chapter 2 we have seen that the force distribution $P(f)$ is extremely robust, in the sense that it does not depend on the geometry of the particle packing. Other groups that have performed simulations using various different algorithms to generate packings, obtained very similar $P(f)$'s. This suggests that force statistics is also insensitive to the 'packing history'. Typically the force distribution decays exponentially for large forces, and for small forces it 'flattens' to some finite value. This robustness strongly indicates that there is a general mechanism producing these typical force distributions.

In this chapter I will present the very first results of a new conceptual approach to the statistics of force networks in granular media. We wish to stress that these ideas have emerged while this thesis was being prepared, and that they have not yet fully matured. Nevertheless, as we shall see, they appear to be very promising, and so we wish to share with the reader some of our excitement about this new development. Clearly, the presentation will reflect that we can only present a snapshot of ideas which are rapidly evolving. The idea is to start with the basic physics of static granular media, namely that *the assembly of particles is mechanically stable*; during the formation of a static pile, the particles have adjusted

their relative positions $\mathbf{r}_{ij}$ such that the forces $\mathbf{F}_{ij}$ obey the equations of mechanical stability

$$\sum_i \mathbf{F}_{ij} = 0 \quad \text{and} \quad \sum_i \mathbf{r}_{ij} \times \mathbf{F}_{ij} = 0 \ , \qquad (6.1.1)$$

for all particles j. Of course, Newton's third law requires $\mathbf{F}_{ij} = -\mathbf{F}_{ji}$, and, depending on the particles under consideration, there can be additional constraints, like Coulomb's law of friction. As we already pointed out in Chapter 1, these sets of equations are typically *underdetermined*. This means that even for a given packing geometry where all $\mathbf{r}_{ij}$ are fixed, there is a *high dimensional force space* of allowed solutions. The actual forces $\mathbf{F}_{ij}$ in a physical realization are of course determined on the microscopic scale by details of the interparticle contacts. For hard particles, however, a tiny variation in $\mathbf{r}_{ij}$ will have a dramatic effect of the corresponding $\mathbf{F}_{ij}$. This results into an effective *separation of length scales*[1] where the forces $\mathbf{F}_{ij}$ become decoupled from the positions $\mathbf{r}_{ij}$. For some given packing geometry we are therefore allowed to treat the forces as independent from the $\mathbf{r}_{ij}$.

In this chapter we lay out the first steps of a theory based on *equal probability of each point in this phase space of forces*, very much like for the microcanonical ensemble in classical statistical mechanics. We show that with this uniform phase space density one quantitatively reproduces the force distributions observed in experiments and simulations, in a small model system. The motivation for using a flat phase space density is simple: nothing is known about how nature samples the space of force networks, so as a first attempt we try a uniform density. Although for the problem of force networks there is no such thing as Liouville's theorem providing a theoretical foundation for our approach, we will show that already for small regular packings we obtain remarkable results. Not only do we find realistic $P(f)$, but as will be discussed at the end of this chapter, our approach also allows to investigate failure of granular media and thermal effects.

---

[1]Strictly speaking, this separation becomes exact for infinitely hard particles. For packings of steel or glass beads one typically has $\Delta r_{ij}/r_{ij} < 10^{-3}$.

6.2 Theory for frictionless spheres

At this stage we limit ourselves to frictionless spheres for which there are no tangential forces. The normal forces are directed along the centers of the particles, so the torque balance equations are trivially obeyed. For a d-dimensional packing of N particles this means that there are dN remaining equations to determine the $zN/2$ unknown 'force magnitudes', where z is the average coordination number. As long as $z > 2d$, there will be a high dimensional space of allowed force configurations, whose dimension grows linearly with the number of particles N. In this section we first mathematically construct this force space and we discuss the role of a force scale. We then show how to calculate $P(f)$ by integrating over this space.

6.2.1 Matrix formulation of mechanical stability

The equations of mechanical stability Eq. (6.1.1) are linear in the forces, so we can formulate them as a matrix problem. Writing the $\mathbf{F}_{ij}$ as

$$\mathbf{F}_{ij} = f_{ij}\,\hat{\mathbf{r}}_{ij} \, , \tag{6.2.1}$$

where $\hat{\mathbf{r}}_{ij}$ is the unit vector in pointing from particle i to particle j, we see that the f_{ij} are the unknowns of the problem. To explicitly formulate mechanical equilibrium as a matrix equation, it is convenient to label each force amplitude in the system with only one index i, so from now on we write just f_i. Mechanical stability can then be written as

$$A\vec{f} = \vec{0} \, , \tag{6.2.2}$$

with

$$\vec{f} = (f_1, f_2, \cdots, f_{zN/2}) \, . \tag{6.2.3}$$

The matrix A is a $zN/2$ times dN matrix representing the force balance equations. To get a feel for the structure of this matrix, let us consider a packing of 3 balls in a snooker-like triangle, as depicted in Fig. 6.1. For this small system it is easy to write A explicitly, and we will analytically compute the corresponding $P(f)$ in Sec. 6.4.1. In this 3-ball system there are six boundary forces (f_1 to f_6), plus three interparticle forces (f_7, f_8, f_9). These nine unknowns must obey the $2 \times 3 = 6$ balance equations, one equation for the x and y directions for each particle. Working out each of these equations, we find that

$$A = \begin{pmatrix} 0 & 0 & 0 & 0 & 0 & \frac{\sqrt{3}}{2} & -1 & 0 & -\frac{1}{2} \\ 1 & 0 & 0 & 0 & 0 & -\frac{1}{2} & 0 & 0 & -\frac{\sqrt{3}}{2} \\ 0 & 0 & -\frac{\sqrt{3}}{2} & 0 & 0 & 0 & 1 & \frac{1}{2} & 0 \\ 0 & 1 & -\frac{1}{2} & 0 & 0 & 0 & 0 & -\frac{\sqrt{3}}{2} & 0 \\ 0 & 0 & 0 & -\frac{\sqrt{3}}{2} & \frac{\sqrt{3}}{2} & 0 & 0 & -\frac{1}{2} & \frac{1}{2} \\ 0 & 0 & 0 & -\frac{1}{2} & -\frac{1}{2} & 0 & 0 & \frac{\sqrt{3}}{2} & \frac{\sqrt{3}}{2} \end{pmatrix}. \quad (6.2.4)$$

The matrix thus consists of many zeros, except for those forces that are in contact with the particle for which we write mechanical equilibrium. This will also be the case for a general packing: the nonzero elements will always lie between -1 and $+1$, since they are just the sines and cosines of the angles defining the orientations of the forces.
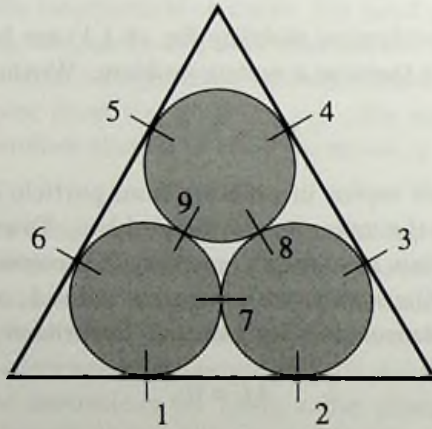
Figure 6.1: Three monodisperse frictionless (infinitely hard) spheres in a snooker triangle. This system has nine unknown force magnitudes: six boundary forces (f_1 to f_6) and three interparticle forces (f_7, f_8 and f_9). In Sec. 6.4.1 we calculate $P(f)$ for both types of forces.

It is important to note that all elements of A are completely determined once a packing structure is given. Each 'force realisation' $\vec{f}$ obeying Eq. (6.2.2) thus provides a static force network for this particular packing. However, since for dry granular matter the particle interactions are purely repulsive we require all $f_i \geq 0$; negative f_i correspond to tensile or attrative forces. We show later how this seemingly innocent condition

forms a tremendous limitation to the physically acceptable $(z/2 - d)N$ dimensional space of solutions.

6.2.2 The role of pressure: fixing the force scale

The matrix equation $A\vec{f} = \vec{0}$ has no intrinsic force scale: if $\vec{f_0}$ is a solution with all $f_i \geq 0$, so is $c\vec{f_0}$ for any $c > 0$. In each physical or numerical realization of a granular packing there is of course a force scale that selects the appropriate value of c. In the carbon paper experiments, for example, this value is imposed by the pressure applied onto the piston confining the grains. The natural way to introduce a force scale in our matrix formulation is thus to fix the total force on a boundary. For the 3-ball snooker triangle this corresponds to keeping the sum $f_1 + f_2$ at a constant value.

It is easily seen for the snooker triangle that fixing the pressure at the boundary implies that the sum of all forces is constant:

$$\sum_i f_i = F_{\text{tot}} = \text{constant} . \tag{6.2.5}$$

In fact, this constraint holds for *any arbitrary packing* once the stress tensor σ is fixed. The components of this stress tensor $\sigma_{\alpha\beta}$ can be expressed in terms of the forces in the system as[2]

$$\sigma_{\alpha\beta} = \sum_i (\mathbf{f}_i)_\alpha \, (\mathbf{r}_i)_\beta , \tag{6.2.6}$$

which in two dimensions reads

$$\sigma_{xx} = \sum_i f_i \, r_i \cos^2 \varphi_i$$

$$\sigma_{yy} = \sum_i f_i \, r_i \sin^2 \varphi_i$$

$$\sigma_{xy} = \sum_i f_i \, r_i \cos \varphi_i \sin \varphi_i . \tag{6.2.7}$$

---

[2]We sidestep here the issue of the coarse graining necessary to derive a macroscopic stress field from a microscopic particle model. Since the systems that we consider are relatively small, this coarse graining will not play a role in our discussion. For details on this, see e.g. [79]

Here φ_i defines the orientation of the force f_i, and r_i is the distance between the centers of two particles connected by f_i. The value of r_i is simply the sum of the radii of the two particles involved, and will be uncorrelated to both f_i and φ_i. We can thus impose the externally applied stress tensor σ by imposing the following constraints:

$$\sum_i f_i \cos^2 \varphi_i = F_{xx} ,$$

$$\sum_i f_i \sin^2 \varphi_i = F_{yy} ,$$

$$\sum_i f_i \cos \varphi_i \sin \varphi_i = F_{xy} , \tag{6.2.8}$$

where F_{xx}, F_{yy} and F_{xy} are constants. In three dimensions there are six stress constraints, one for each independent component of the stress tensor.

By extending the matrix A with these linear equations, we automatically restrict the $\vec{f}$ to realizations with a given σ. Integrating over the space of these solutions, we take *an ensemble average over realizations with equal stress*. These constraints also imply that $\langle f \rangle$ is fixed for all solutions, since

$$F_{xx} + F_{yy} = \sum_i f_i \left(\cos^2 \varphi_i + \sin^2 \varphi_i \right) = F_{\text{tot}} . \tag{6.2.9}$$

6.2.3   Microcanonical-like ensemble of force space

Let us now mathematically construct the phase space of force networks, and show how to derive $P(f)$ or any other statistical quantity from it. The phase space is defined by the force balance equations, represented by the matrix A, the stress constraints of Eq. (6.2.8), and the condition that all $f_i \geq 0$. This can be written as

$$\mathcal{A}\vec{f} = \vec{b} \quad \text{and} \quad \forall \quad f_i \geq 0 , \tag{6.2.10}$$

where $\mathcal{A}$ is the matrix A extended by the stress constraints. For two dimensional packings this schematically reads

$$\left.\begin{array}{c}\left(\text{Mechanical equilibrium}\right) \\ \left(\text{Stress constraints}\right)\end{array}\right) \begin{pmatrix} f_1 \\ f_2 \\ \cdot \\ \cdot \\ \cdot \\ \cdot \\ \cdot \\ \cdot \\ \cdot \\ \cdot \\ \cdot \\ \cdot \\ f_{zN/2} \end{pmatrix} = \begin{pmatrix} 0 \\ 0 \\ \cdot \\ \cdot \\ \cdot \\ 0 \\ F_{xx} \\ F_{yy} \\ F_{xy} \end{pmatrix} ,$$

$$(6.2.11)$$

and for three dimensional packings there will be six instead of three stress equations. We thus encounter an *inhomogeneous* matrix problem, for which we can write the general solution as

$$\vec{f} = \vec{f}_0 + \sum_k a_k \vec{v}_k , \qquad (6.2.12)$$

where $\vec{f}_0$ is a particular solution of the inhomogenous problem and $\mathcal{A}\vec{v}_k = \vec{0}$. The number of independent $\vec{v}_k$ is equal to $(z/2 - d)N$ minus the number of independent stress constraints, and we conveniently take an orthonormal basis $\{\vec{v}_k\}$, so that $\vec{v}_k \cdot \vec{v}_l = \delta_{kl}$. This general solution does not automatically obey the condition that all $f_i \geq 0$. Considering each f_i as a function of $\vec{a} = (a_1, a_2, \cdots)$, we derive constraints for the a_k:

$$f_i(\vec{a}) = f_{0i} + \sum_k a_k v_{ki} \geq 0 \qquad \text{for} \quad i = 1, 2, \cdots, zN/2 ; \qquad (6.2.13)$$

f_{0i} and v_{ki} are the ith components of $\vec{f}_0$ and $\vec{v}_k$ respectively, and can be determined from $\mathcal{A}$.

The phase space of allowed force network solutions is thus defined by Eqs. (6.2.12) and (6.2.13), and this space can be explored by varying the parameters a_k. The central point of our approach is that we assume each point in this space to be equally probable. This means that the probability density for the a_k can be written as

$$P_a\left(\vec{a}\right) = \frac{1}{\Omega} \prod_i \Theta\left(f_{0i} + \sum_k a_k\, v_{ki}\right) , \qquad (6.2.14)$$

where the Heaviside functions assure that $f_i \geq 0$, and this density is normalized by the phase space volume

$$\Omega = \int d\vec{a} \prod_i \Theta\left(f_{0i} + \sum_k a_k\, v_{ki}\right) . \qquad (6.2.15)$$

From this, we can obtain the force distribution $P(f_i)$ as

$$P(f_i) = \int d\vec{a}\, P_a(\vec{a})\, \delta\left(f_i - f_{0i} - \sum_k a_k\, v_{ki}\right) , \qquad (6.2.16)$$

or any other statistical average like correlation functions, as

$$\left\langle G(\vec{f}) \right\rangle = \int d\vec{a}\, P_a(\vec{a})\, G(\vec{f}) . \qquad (6.2.17)$$

The formal analysis above provides an explicit framework to calculate any statistical property of the force network, given the assumptions that all stable (repulsive) force networks are equally probable and that the interparticle forces are decoupled from the particle positions. In the remainder of this chapter we show that these assumptions are indeed sufficient to reproduce nontrivial experimental and numerical results on force network statistics.

6.3   Fixing the force scale: exponential tail

Before solving the full problem described above, it is instructive to ignore the complicated equations of mechanical stability and to discuss the statistics resulting from the stress constraints only. As already mentioned, this stress constraint implies that the sum of all forces is constant, just like the sum of all energies is constant in the microcanonical ensemble. From the latter we know that the energies become distributed according to the Boltzmann weights $e^{-E/k_B T}$, so we anticipate that the stress constraint is responsable for the generic exponential tail in $P(f)$ for force distributions.

Let us briefly reconstruct the argument leading to the purely exponential Boltzmann distribution. Consider a set of n independent variables $x_i \geq 0$ that is constrained by

$$\sum_{i=1}^{n} x_i = X .$$ (6.3.1)

The phase space of these variables is a $(n-1)$ dimensional hyperplane of volume

$$
\begin{aligned}
\Omega_n(X) &= \int d\vec{x}\, \delta\left(X - \sum_{i=1}^{n} x_i\right) \prod_{i=1}^{n} \Theta(x_i) \\
&= X^{n-1} \int_0^1 dq_1 \cdots \int_0^1 dq_n\, \delta\left(1 - \sum_{i=1}^{n} q_i\right) \\
&= \frac{X^{n-1}}{(n-1)!} ,
\end{aligned}
$$ (6.3.2)

where the integral has been evaluated using Eq. (3.3.8). Using a uniform phase space density on this hyperplane, we compute the distribution of one variable $P(x\,;n)$ as:

$$
\begin{aligned}
P(x\,;n) &= \frac{1}{\Omega_n(X)} \int_0^\infty dx_1 \cdots \int_0^\infty dx_{n-1}\, \delta\left(X - x - \sum_{i=1}^{n-1} x_i\right) \\
&= \frac{\Omega_{n-1}(X - x)}{\Omega_n(X)} \\
&= \frac{n-1}{X}\left(1 - \frac{x}{X}\right)^{n-2} ,
\end{aligned}
$$ (6.3.3)

which in the limit $n \to \infty$ becomes

$$P(x\,;\infty) = \frac{1}{\langle x \rangle}\, e^{-x/\langle x \rangle} \qquad \text{with} \qquad \langle x \rangle = X/n .$$ (6.3.4)

This result has a nice geometrical interpretation. The value x can in principle attain a maximum value X, but the available phase space volume decreases as $(1 - x/X)^{n-2}$ when this maximum value is approached. The power $n - 2$ originates from the $(n-1)$ dimensional hyperplane, minus one dimension to indicate the value of x. This is a general route towards an exponential tail: large values of x become exponentially suppressed

whenever the phase space volume decreases with some increasingly high power as a maximum value is approached.

In our case of granular force networks the variables f_i are not only restricted by this overall sum constraint, but there are also dN equations of mechanical equilibrium. As it turns out, these equations alter the behavior of $P(f)$ for small forces, but not the generic exponential decay.

6.4   Regular packings: balls in a snooker triangle

We now work out the theory that has been developed in Sec. 6.2 for small systems of crystalline (monodisperse) packings. We analytically compute $P(f)$ for the problem of 3 balls in a snooker triangle shown in Fig. 6.1, which forms a nice illustration of our approach. We then numerically sample the phase space of the 6-ball system depicted in Fig. 6.5; this system is already large enough to produce the essential features of realistic $P(f)$.

6.4.1   Three balls

The $2 \times 3 = 6$ equations of mechanical equilibrium for the 3 balls have been worked out explicitly in Eq. (6.2.4). The triangular geometry imposes an isotropic pressure, so there is only one independent stress constraint; we set the force scale by keeping $f_1 + f_2 = 2$. There are thus seven equations to determine the nine unknown forces $(f_1, \cdots, f_9)$, hence there is a two-dimensional space of solutions. For this low-dimensional system, we can construct the phase space in a very direct manner: instead of determining the vectors $\vec{v}_1$ and $\vec{v}_2$ algebraically, we define the 2D plane by 3 independent simple solutions of the problem. We take the solutions that are sketched in Fig. 6.2; these solutions are indeed independent since they independently 'switch on' the values of f_7, f_8 and f_9 respectively.

The space of solutions turns out to be the triangle depicted in Fig. 6.3a, where the three solutions are the corners of the triangle. This can be understood as follows. The first solution depicted in Fig. 6.2 has $(f_7, f_8, f_9) = (0, 0, \sqrt{3})$, and is represented by the right corner of the triangle of Fig. 6.3a. The solution on the left corner corresponds to the solution $(f_7, f_8, f_9) = (0, \sqrt{3}, 0)$; since a superposition of these two solutions is still a solution of our linear problem, the base of the triangle is a line where $f_7 = 0$. The upper corner represents the solution where f_7
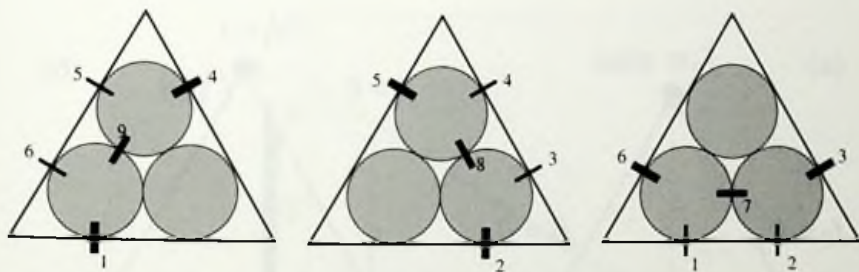
Figure 6.2: The 2D phase space of the 3-ball problem can be spanned using three simple independent solutions of the problem. The first solution has $f_1 = f_4 = 2$, $f_5 = f_6 = 1$ and $f_9 = \sqrt{3}$; the other solutions follow from rotational symmetry.

attains its maximum value of $\sqrt{3}$, so the dashed line can be seen as the projection of the f_7 axis onto this two dimensional space of solutions. This implies that the space below the triangle corresponds to a region where $f_7 < 0$, which is forbidden for repulsive particles. Applying the same argument for f_8 and f_9, one realizes that only the area inside the triangle is allowed.

How about the boundary forces f_1 to f_6? Checking the three independent solutions, one finds that $f_1 = 0$ at the left corner, $f_1 = 1$ at the upper corner, and $f_1 = 2$ at the right corner of the 'phase space triangle'. From the geometric construction in Fig. 6.3b, it is easy to find the $f_1 = 0$ line, and the projection of the f_1 axis is indicated by the arrow. Due to symmetry there are of course six such borders ($f_1 = 0$ to $f_6 = 0$), and all boundary forces are positive inside the hexagon. So indeed, the phase space of solutions for which all $f_i \geq 0$ lies within the triangle.

Just like in Chapter 2, we again find that there is a qualitative difference between the boundary forces $(f_1, \cdots, f_6)$ and the interparticle forces (f_7, f_8, f_9). We therefore have to consider $P(f_1)$ and $P(f_7)$ separately; the other force distributions follow from symmetry. Assuming a flat phase space density, the probability to find a solution between f_7 and $f_7 + \delta f_7$ is simply represented by the shaded area in Fig. 6.3a. The probability *density* for a given value of f_7 is thus the 'volume' of this phase space. This volume decreases linearly as f_7 approaches its maximum value, so that $P(f_7) \propto (\sqrt{3} - f_7)$, yielding the solid curve of Fig. 6.4. The distribution $P(f_1)$ can be found in a similar manner, and is depicted as the dotted
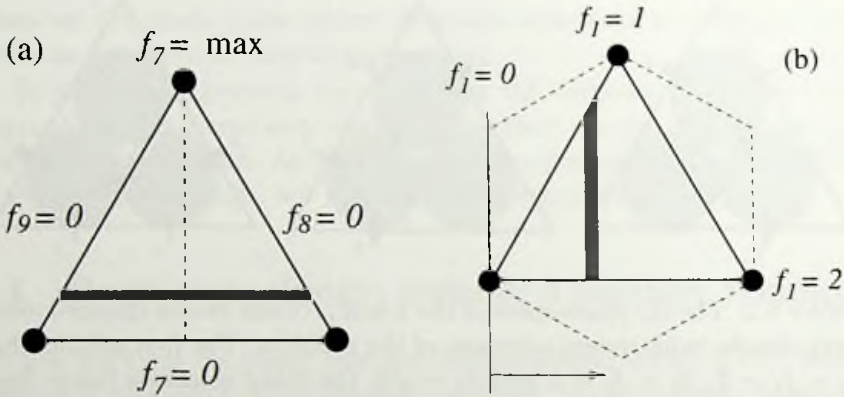
Figure 6.3: The phase space of the 3-ball problem: *(a)* the borders of the triangle are the lines where one of the interparticle forces changes sign; *(b)* the borders of the hexagon are the lines where one of the 'boundary' forces changes sign. The shaded areas represent the probability for a certain f_7 and f_1 respectively.

curve of Fig. 6.4.

This 3-ball system provides a very nice illustration of how a force distribution can be obtained by integrating over all possible configurations of the force network. Before we continue with the problem of 6 balls, let us make two important remarks. Firstly, the obvious 'uniform' solution, for which all boundary forces are unity and the interparticle forces are $\sqrt{3}/3$, is only one point in the phase space, namely the middle of the triangle. The fact that there is a (high dimensional) space of allowed force networks is presumably the underlying reason that $P(f)$ for large crystalline packings is very similar to $P(f)$ for amorphous packings: the uniform solution is only one point in this space and does not dominate the statistics. Secondly, the observed $P(f_7)$ is identical to the 'finite-size-Boltzmann' distribution of Eq. (6.3.3) with $n = 3$. In the case of 6 balls we already encounter deviations from this behavior, leading to non-exponential $P(f)$.

6.4.2   Six balls

For the system of 6 balls in a snooker triangle, there are 18 forces for which there are $2 \times 6 + 1 = 13$ equations (Fig. 6.5). The space of solutions is therefore five-dimensional, so we can no longer make a simple construction
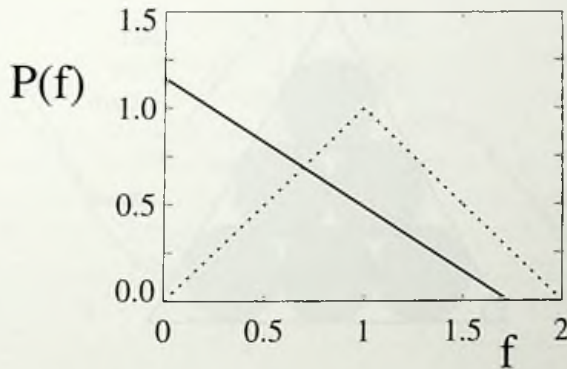
Figure 6.4: The distributions of the interparticle forces (solid line) and of the boundary forces (dotted line) for the three balls in a snooker triangle.

like we did for the 3-ball problem. Below we explain how to sample this space numerically, following the procedure explained in Sec. 6.2.3.

We first have to determine a basis $\{\vec{v}_k\}$, and to find a particular solution $\vec{f}_0$. For a regular packing it is easy to construct such a particular solution since one can always take the uniform solution; in this case, all boundary forces are unity and the interparticle forces are $\sqrt{3}/3$. We can sample all possible solutions by varying the five parameters a_k appearing in Eq. (6.2.12). To assure that the space is sampled with a uniform density, we have generated the a_k within a 5D hypercube (around $\vec{f}_0$) that contains the whole phase space volume Ω. By keeping only the solutions with all $f_i \geq 0$, we exactly follow the theory of Sec. 6.2, in particular Eq. (6.2.16), without making any approximations.

The results are shown in Fig. 6.6. The panel on the left shows the force distributions for the two types of interparticle forces (solid and dashed lines) and for the boundary forces (dotted line); in the right panel the various $P(f)$ have been rescaled such that $\langle f \rangle = 1$. The resemblance with the data from our Hertzian sphere simulations presented in Chapter 2 is truly remarkable. The interparticle force distributions shown e.g. in Fig. 2.2a are even *quantitatively* similar to those obtained for this simple six ball geometry. The main difference is that in the latter case there is a force cut-off due to the finite size of the packing. The distribution of boundary forces in Fig. 6.6 (dotted line) can be compared to the particle-wall forces distribution at the boundary of our Hertzian packings, for
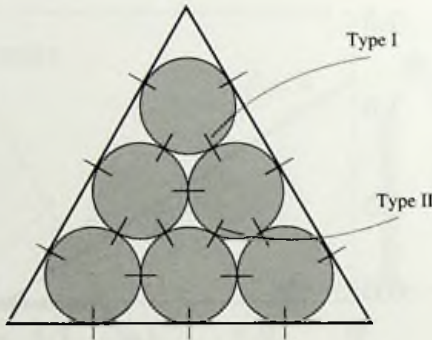
Figure 6.5: Six monodisperse frictionless spheres in a snooker triangle. This system has 18 unknown force magnitudes: nine boundary forces and nine interparticle forces. Due to symmetry, there are two types of interparticle forces, namely six that are closest to a boundary (Type I) and three close to the center (Type II).

particles that have two contacts from above ($n_c = 2$); this corresponds to $\mathcal{P}_2(w)$ from Fig. 2.6b. Again, there is almost a one-to-one correspondance between the two curves.

Finally, we have analyzed the behavior of $P(f)$ around f_{max} in the inset of Fig. 6.6, where we plotted $P(f)$ as a function of $f_{max} - f$. As a guide to the eye we have drawn the line $(f_{max} - f)^3$, which seems to be the proper scaling for large forces. This strongly suggests that indeed, $P(f)$ will decay exponentially in the thermodynamic limit where both f_{max} and the scaling exponent around f_{max} will go to infinity.

6.5   Geometric interpretation

Let us now try to understand how the shape of $P(f)$ emerges from the integration over the phase space of all possible force networks. Firstly, the behavior for large forces is now easily understood. The stress constraint limits each force to be smaller than some maximum value f_{max}, and the associated volume decreases as $(f_{max} - f)$ to some integer power that grows as a function of N. In Sec. 6.3 we have shown how this leads to an exponentially decaying force distribution in the limit that $N \rightarrow \infty$. In other words, the generic exponential tail of $P(f)$ that has been observed in a large variety of experiments, simulations and models is a
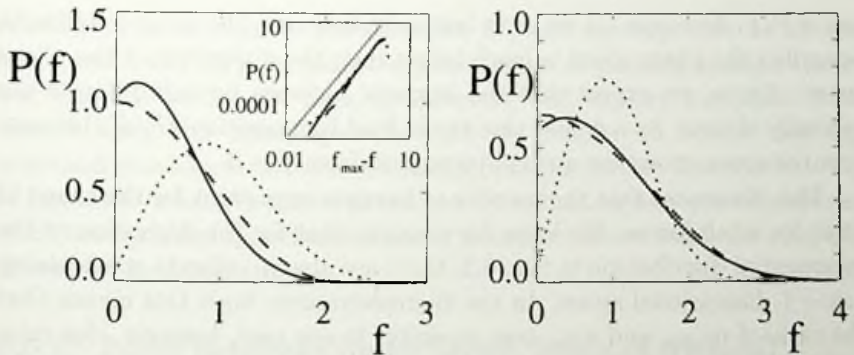
Figure 6.6: The force distributions for the Type I interparticle forces (solid line), the Type II interparticle forces (dashed line) and the boundary forces (dotted). The left panel shows $P(f)$ with the unscaled forces. In the inset we plot $P(f)$ as a function of $f_{max} - f$ on a logarithmic scale, and compare it to $(f_{max} - f)^3$ (straight line). The right panel shows the various $P(f)$ after rescaling to $\langle f \rangle = 1$.

direct consequence of the fact that in all these cases there was a stress constraint.

The more difficult part is the non-exponential behavior for small forces. The general observation is that $P(f)$ becomes suppressed relative to a pure exponential, and that typically dP/df at $f = 0$ becomes even positive. Again, we propose a purely geometric interpretation for this behavior. Let us stress that the argumentation below is handwaving and requires further investigation.

For the problem of 3 balls we have seen how each condition $f_i \geq 0$ divides the phase space into two parts: allowed and not allowed regions. Together, all subspaces where $f_i = 0$ constitute the borders of the allowed phase space. In general, this space can thus be regarded as the interior of some sort of a 'hyperpolygone', whose *facets* are given by the conditions $f_i = 0$. Ignoring the stress constraints and the fact that boundary forces can play a different role, we have a $(z/2 - d)N$ dimensional hyperpolygone with $zN/2$ facets. To understand how the dimensionality n_{dim} and the number of facets n_{facets} relates to $P(f)$ for small force, we provide the following intuitive picture. For the case of 3 balls, the allowed phase space was a triangle where the corners between the bounding edges are acute. If we move away from a $f = 0$ edge, the available phase space volume and

hence $P(f)$ decreases. If we go to larger N, however, the number of facets bounding the phase space is much larger then the dimension of the phase space. Hence, we expect that the 'corners' between bounding facets are typically obtuse. As a result, this would lead to a positive dP/df, because now the space grows for a small increment from $f = 0$.

This illustrates that the number of facets is important for the shape of $P(f)$ for small forces. We know for example that for the derivation of the exponential distribution in Sec. 6.3, there are always n facets constraining a $n - 1$ dimensional space. In the thermodynamic limit this means that the ratio of n_{facets} and n_{dim} goes to unity. In our case, however, this ratio will always be larger than unity, namely $z/(z - 2d)$. For example, for the 2D hexagonal packing this ratio will be 3. Although it is not a priori clear why this ratio should be the relevant parameter, it *does* provide a qualitative explanation why the observed dP/df at $f = 0$ is always larger than for an exponential distribution: the larger the number of facets for a given n_{dim}, the larger dP/df at $f = 0$. So apparently, the equations of mechanical stability change the behavior for small forces away from a purely exponential distribution, without affecting exponential decay for large forces.

6.6   Summary and outlook

In this chapter we have explored the phase space of all possible force realizations that lead to mechanical equilibrium for a given packing geometry. Under the assumption that the magnitude of the interparticle forces are decoupled from the particle positions, we have mathematically constructed this space of force networks in Sec. 6.2. We then showed in Sec. 6.4 that the assumption that all allowed force configurations are equally probable is sufficient to reproduce realistic force distributions $P(f)$, even for small regular packings. This work also reveals how the shape of $P(f)$ comes about. The generic exponential tail originates from fixing the overall force scale in the system: by applying some external pressure, one constrains the sum of all forces just like the total energy in the microcanonical ensemble is fixed. Imposing the equations of mechanical equilibrium leads to the non-exponential behavior for small forces, but these equations do not affect the exponential tail of the force distribution.

The ideas presented in this chapter are very much in the spirit of Edwards ensembles, in which all packing geometries of a given density are

postulated to be equally probable [80, 81]. In our approach we do not touch upon the very complicated phase space of packing configurations, but instead, we fix the packing geometry and explore the *linear* force space. Since this phase space is relatively simple, we believe that our approach provides an attractive starting point for further theoretical study of force networks. We close this chapter by indicating how one can address some fundamental questions on static granular matter using the concepts developed in this chapter.

6.6.1   Force networks under shear: angle of friction?

Static granular matter will fail when subjected to large enough shear forces. According to the Mohr-Coulomb theory granular matter has an internal 'angle of friction' very much like the friction coefficient in Coulomb's law of friction between two solid bodies [31]. A typical laboratory experiment to measure this internal angle of friction is a so-called biaxial test, in which a system is compressed anisotropically. One thus increases the difference in normal stress $\sigma_{xx} - \sigma_{yy} \neq 0$, and measures when the material fails.

As can be seen from Eq. (6.2.8), we can easily perform this test within our matrix formulation by just varying the values of F_{xx} and/or F_{yy}. Preliminary results for systems of 1024 particles that have been sampled by a Monte Carlo scheme indicate that there is a well-defined value of $\sigma_{xx} - \sigma_{yy}$, above which solutions with strictly repulsive forces no longer exist. This suggests that the phase space volume Ω as defined in Eq. (6.2.15) vanishes at some threshold value of $\sigma_{xx} - \sigma_{yy}$, providing a prediction *from microscopics* for the internal angle of friction. We should note, however, that in real biaxial experiments there will be microscopic rearrangements before the material fails. These are not within our model since we keep the packing geometry fixed.

6.6.2   Random matrices and including thermal fluctuations

The first dN rows of the matrix $\mathcal{A}$ that defines our phase space consist of many zeros, except for a few elements per row that lie between -1 and $+1$. Such a matrix has some features of a random matrix, but it implicitly contains the entire spatial structure of the system. By comparing such a packing matrix $\mathcal{A}$ with a true *random matrix*, which contains no spatial structure, we can address a very important question: does $P(f)$ have the

same shape if we throw away all spatial information? In other words, are spatial aspects of the force network important for the large fluctuations?

Finally, let us try to make a connection with the jamming transition discussed in Chapter 1, by considering a force network with small thermal fluctuations. At $T = 0$, the vector $\vec{b}$ on the right hand side of Eq. 6.2.10 has only zeros, except for the stress constraints. For small $T \ll T_g$, the particles will not be stationary but instead experience small accelerations, allowing the elements of $\vec{b}$ to fluctuate around zero. This will effectively 'weaken' the constraints, since mechanical equilibrium has to be obeyed only approximately. Within the interpretation that constraints alter $P(f)$ away from a purely exponential distribution for small forces, we would indeed expect a trend as observed in Fig. 1.8 upon a temperature increase.

Our preliminary results are very promising, and make us hopeful that this approach can be turned into a new statistical physical theory for granular packings, that is able to address many of the fundamental issues raised recently in the context of jamming.

Bibliography

[1] *The Physics of Blown Sand and Desert Dunes*, by R. A. Bagnold (Methuen, London 1941).

[2] H. M. Jaeger, S. R. Nagel and R. P. Behringer, Rev. Mod. Phys. **68**, 1259 (1996).

[3] P. G. de Gennes, Rev. Mod. Phys. **71**, 374 (1999).

[4] L. P. Kadanoff, Rev. Mod. Phys. **71**, 435 (1999).

[5] *Sand, Powders and Grains*, by J. Duran (Springer-Verlag, New York 2002).

[6] T. S. Komatsu, S. Inagaki, N. Nakagawa and S. Nasuno, Phys. Rev. Lett. **86**, 1757 (2001).

[7] *Sliding Friction*, by B. N. J. Persson (Springer-Verlag, Berlin 2000), 2nd ed.

[8] *Contact Mechanics*, by K. L. Johnson (Cambridge University Press, Cambridge, England 1985).

[9] P. Dantu, Ann. Ponts Chaussees **4**, 144 (1967).

[10] L. Vanel, D. Howell, D. Clark, R. P. Behringer and E. Clement, Phys. Rev. E **60**, R5040 (1999).

[11] J. Geng, G. Reydellet, E. Clement and R. P. Behringer, cond-mat/0211031, to appear in Physica D.

[12] O. Reynolds, Phil. Mag. Ser 5 **50**, 469 (1885).

[13] C. T. Veje, D. W. Howell and R. P. Behringer, Phys. Rev. E **59** 739 (1999).

[14] D. Howell, R. P. Behringer and C. Veje, Phys. Rev. Lett. **82** 5241 (1999).

[15] D. M. Mueth, G. F. Debregeas, G. S. Karczmar, P. J. Eng, S. R. Nagel, H. M. Jaeger, Nature **406**, 385 (2000).

[16] W. Losert, L. Bocquet, T. C. Lubensky and J. P. Gollub, Phys. Rev. Lett. **85** 1428 (2000).

[17] D. Fenistein and M. van Hecke, in preparation.

[18] The images were made available by D. Fenistein and M. van Hecke.

[19] W. Losert and G. Kwon, Advances in Complex Systems **4**, 369 (2001).

[20] C. H. Liu, S. R. Nagel, D. A. Schecter, S. N. Coppersmith, S. Majumdar, O. Narayan and T. A. Witten, Science **269**, 513 (1995).

[21] D. M. Mueth, H. M. Jaeger and S. R. Nagel, Phys. Rev. E **57**, 3164 (1998).

[22] D. L. Blair, N. W. Mueggenburg, A. H. Marshall, H. M. Jaeger and S. R. Nagel, Phys. Rev. E **63**, 041304 (2001).

[23] G. Løvoll, K. J. Måløy and E. G. Flekkøy, Phys. Rev. E **60**, 5872 (1999).

[24] T. C. Halsey and D. Ertas, Phys. Rev. Lett. **83**, 5007 (1999).

[25] C. F. Moukarzel, Phys. Rev. Lett. **81**, 1634 (1998).

[26] A. V. Tkachenko and T. A. Witten, Phys. Rev. E **60**, 687 (1999).

[27] H. A. Makse, D. L. Johnson, L. M. Schwartz, Phys. Rev. Lett. **84**, 4160 (2000).

[28] L. E. Silbert, D. Ertas, G. S. Grest, T. C. Halsey and D. Levine, Phys. Rev. E **65**, 031304 (2002).

[29] J. N. Roux, Phys. Rev. E **61**, 6802 (2002).

[30] S. N. Coppersmith, C. H. Liu, S. Majumdar, O. Narayan and T. A. Witten, Phys. Rev. E **53**, 4673 (1996).

[31] *Statics and Kinematics of Granular Materials*, by R. M. Nedderman (Cambridge University Press, Cambridge, England 1992).

[32] A. Daerr and S. Douady, Nature **399**, 241 (1999).

[33] P. Claudin, J. P. Bouchaud, M. E. Cates and J. P. Wittmer, Phys Rev. E **57**, 4441 (1998).

[34] J. P. Bouchaud, cond-mat/0211196, to appear in Proceedings of the 2002 Les Houches Summer School on *Slow Relaxations and Nonequilibrium Dynamics in Condensed Matter.*

[35] S. B. Savage, in *Physics of Dry Granular Media*, edited by H. J. Herrmann, J. P. Hovi and S. Luding, NATO ASI (Kluwer, Dordrecht, the Netherlands 1998).

[36] F. Cantelaube, A. K. Didwania and J. D. Goddard, in *Physics of Dry Granular Media*, edited by H. J. Herrmann, J. P. Hovi and S. Luding, NATO ASI (Kluwer, Dordrecht, the Netherlands 1998).

[37] C. Goldenberg and I. Goldhirsch, Phys. Rev. Lett. **89**, 084302 (2002).

[38] A. J. Liu and S. R. Nagel, Nature **396**, 21 (1998).

[39] C. S. O'Hern, S. A. Langer, A. J. Liu and S. R. Nagel, Phys. Rev. Lett. **86**, 111 (2002).

[40] M. E. Cates, J. P. Wittmer, J. P. Bouchaud and P. Claudin, Phys. Rev. Lett. **81**, 1841 (1998).

[41] L. E. Silbert, D. Ertas, G. S. Grest, T. C. Halsey and D. Levine, Phys. Rev. E **65**, 051307 (2002).

[42] W. Kob and H. C. Andersen, Phys. Rev. E **52**, 4134 (1995).

[43] J. P. Bouchaud, P. Claudin, D. Levine and M. Otto, Eur. Phys. J. E **4**, 451 (2001).

[44] J. E. S. Socolar, D. G. Schaeffer and P. Claudin, Eur. Phys. J. E **7**, 353 (2002).

[45] F. Radjai, M. Jean, J. J. Moreau and S. Roux, Phys. Rev. Lett. **77**, 274 (1996).

[46] S. Luding, Phys. Rev. E **55**, 4720 (1997).

[47] F. Radjai, D. E. Wolf, M. Jean and J. J. Moreau, Phys. Rev. Lett. **80**, 61 (1998).

[48] A. V. Tkachenko and T. A. Witten, Phys. Rev. E **62**, 2510 (2000).

[49] S. J. Antony, Phys. Rev. E **63**, 011302 (2000).

[50] C. S. O'Hern, S. A. Langer, A. J. Liu and S. R. Nagel, Phys. Rev. Lett. **88**, 075507 (2002).

[51] G. Reydellet and E. Clement, Phys. Rev. Lett. **86**, 3308 (2001).

[52] J. Geng, D. Howell, E. Longhi, R. P. Behringer, G. Reydellet, L. Vanel, E. Clement and S. Luding, Phys. Rev. Lett **87**, 035506 (2001).

[53] N. W. Mueggenburg, H. M. Jaeger and S. R. Nagel, cond-mat/0204533.

[54] D. A. Head, A. V. Tkachenko and T. A. Witten, Eur. Phys. J. E **6**, 99 (2001).

[55] P. K. Haff, J. Fluid. Mech. **134**, 401 (1983).

[56] I. S. Aranson, L. S. Tsimring, Phys. Rev. E **64**, 020301 (2001).

[57] Y. Forterre and O. Pouliquen, J. Fluid Mech. **467**, 361 (2002).

[58] L. Bocquet, W. Losert, D. Schalk, T. C. Lubensky and J. P. Gollub, Phys. Rev. E **65**, 011307 (2002).

[59] E. R. Nowak, J. B. Knight, E. Ben-Naim, H. M. Jaeger and S. R. Nagel, Phys. Rev. E **57**, 1971 (1998).

[60] G. D'Anna, G. Gremaud, Nature **413**, 407 (2001).

[61] C. Claudin, J-P. Bouchaud, Phys. Rev. Let **78**, 231 (1997).

[62] M. Nicodemi, Phys. Rev. Let **80**, 1340 (1998).

[63] J. E. S. Socolar, Phys. Rev. E **57**, 3204 (1998).

[64] M. L. Nguyen and S. N. Coppersmith, Phys. Rev. E **59**, 5870 (1999).

[65] O. Narayan, Phys. Rev. E **63**, 010301 (2000).

[66] J. M. Erikson, N. W. Mueggenburg, H. M. Jaeger and S. R. Nagel, Phys. Rev. E **66**, 040301 (2002).

[67] L. E. Silbert, G. S. Grest and J. W. Landry, Phys. Rev. E **66**, 061303 (2002).

[68] *Quantum Field Theory and Critical Phenomena*, by J. Zinn-Justin, (Clarendon, Oxford 1990), p. 214 [Eq. (9.39)].

[69] R. Rajesh and S. N. Majumdar, Phys. Rev. E **62**, 3186 (2000).

[70] M. Lewandowska, H. Mathur, and Y.K. Yu, Phys. Rev. E **64**, 026107 (2001).

[71] F. Zielen and A. Schadschneider, J. Stat. Phys. **106**, 173 (2002).

[72] *Solid State Physics*, by N. W. Ashcroft and N. D. Mermin, (Saunders College, Philadephia 1976), p. 73 [Fig. 4.13].

[73] T. Ligget, *Interacting Particle Systems: Contact, Voter and Exclusion Processes*, (Springer, Berlin 1999).

[74] B. Derrida, M. R. Evans, V. Hakim and V. Pasquier, J. Phys. A **26**, 1493 (1993).

[75] J. Krug and J. Garcia, J. Stat. Phys. **99**, 31 (2000).

[76] R. Rajesh and S. N. Majumdar, J. Stat. Phys. **99**, 943 (2000).

[77] K. Nagel and M. Schreckenberg, J. Phys. I **2**, 2221 (1992).

[78] *Handbook of Mathematical Functions With Formulas, Graphs, and Mathematical Tables*, edited by M. Abramowitz and I. A. Stegun, (Dover, New York 1965), p. 504 [Eq. (13.1.2)] and p. 508 [Eq. (13.5.1)].

[79] I. Goldhirsch and C. Goldenberg, Eur. Phys. J. E **9**, 245 (2002).

[80] S. F. Edwards and R. B. S. Oakeshott, Physica A **157**, 1080 (1989).

[81] H. A. Makse and J. Kurchan, Nature **415**, 614 (2002).

Samenvatting

Dit proefschrift gaat over het gedrag van *granulaire media*. Dit zijn systemen die bestaan uit een grote hoeveelheid korrels (grains), zoals bijvoorbeeld zand, suiker, een bak spijkers of de ijsdeeltjes in de ringen van Saturnus.

Een veelgestelde vraag is waarom een natuurkundige überhaupt geïnteresseerd is in deze systemen. Het antwoord hierop is dat de natuurkunde het gedrag probeert te begrijpen van de dingen die in de 'natuur' voorkomen, en dus ook deze granulaire materialen. En deze systemen blijken onverwacht rijke fenomenen in zich te herbergen, die in de meeste gevallen slecht of totaal niet zijn begrepen. Want hoewel de interactie tussen twee aangrenzende korrels vaak nog niet zo ingewikkeld is, is het een buitengewoon lastige opgave om het *collectieve gedrag* van alle deeltjes samen te begrijpen. Het schoolvoorbeeld van dergelijk collectief gedrag zijn lawines. Delen van een zandhoop worden instabiel wat leidt tot de beweging van een groeiend aantal korrels, die even later weer tot rust komen. Andere bekende voorbeelden van complexe granulaire systemen zijn de zich steeds verplaatsende zandduinen in de Sahara of het stromen van graan in een silo.

De traditionele weg om vanaf het niveau van individuele deeltjes het collectieve gedrag te begrijpen is via statistiek: de grote hoeveelheid deeltjes nodigt uit om het gemiddelde gedrag van deze deeltjes te onderzoeken. Het is langs deze weg dat pioniers als Ludwig Boltzmann en Josiah Willard Gibbs aan het eind van de 19e eeuw de basis hebben gelegd voor de *statistische mechanica*. Zij ontwikkelden een zeer krachtig formalisme waarmee macroscopische eigenschappen van gassen, vloeistoffen en vaste stoffen kunnen worden afgeleid van de microscopische wetten voor de atomen en moleculen waaruit deze zijn opgebouwd. In deze theorie, die geldt voor systemen in *thermodynamisch evenwicht*, speelt de relatie tussen energie en temperatuur een cruciale rol. Als bijvoorbeeld een gas in

een gesloten ruimte wordt verhit neemt de gemiddelde energie van de gas-moleculen toe, wat leidt tot een hogere druk. Of wanneer een blok metaal wordt verhit gaan de atomen in het metaal heftiger trillen rondom hun kristalposities, waardoor het blok uitzet. De thermische energie E en temperatuur T zijn met elkaar verbonden via de constante van Boltzmann, $k_B = 1.38\,10^{-23}$ Joule per Kelvin. Zo hebben de moleculen in een ideaal gas een gemiddelde energie $E = \frac{3}{2}k_B T$, wat bij kamertemperatuur (300 Kelvin) neerkomt op $6.2\,10^{-21}$ Joule. Voor een zuurstofmolecuul in onze atmosfeer is deze luttele hoeveelheid energie voldoende voor een snelheid van enkele honderden meters per seconde.

Deze koppeling van thermische energie en de 'vrijheidsgraden' van de deeltjes vormt de sleutel tot het succes van de thermodynamica. De benodigde tijd voor een macroscopische meting is enorm groot ten opzichte van de tijdschaal waarop de moleculaire processen zich afspelen. Hierdoor kan het systeem een onvoorstelbare hoeveelheid microscopische toestanden doorlopen tijdens elke meting, en zal het gemiddelde gedrag steeds hetzelfde zijn. Het systeem is dan *in thermodynamisch evenwicht*.

Laten we terugkeren naar granulaire materialen, en laten we de korrels nu beschouwen als de 'moleculen' waaruit een granulair systeem is opgebouwd. De minimaal benodigde energie om een korrel over zijn buurman te tillen is van de orde mgd, waarbij m en d de massa respectievelijk de diameter van de korrels zijn en $g = 9.8\,\text{m/s}^2$ is de zwaartekrachtsversnelling. Zelfs voor de kleinste zandkorrels is deze benodigde energie dusdanig groot dat de thermische energie nooit genoeg zou kunnen zijn om de korrels in beweging te zetten; thermische energie wordt pas van belang wanneer de deeltjes kleiner zijn dan ongeveer een tiende van de dikte van een haar. Hierdoor zijn granulaire media altijd *ver-uit-thermodynamisch-evenwicht* en zijn de klassieke statistische methoden niet meer toepasbaar. Natuurlijk kan men de korrels in beweging krijgen door 'met de hand' energie toe te voegen aan het systeem. Bijvoorbeeld door het schudden van een bak met korrels creëer je een zogenaamd granulair gas. Echter, ook deze systemen zijn ver-uit-evenwicht omdat er steeds energie verloren gaat tijdens de niet perfect elastische botsingen tussen de korrels.

Het is duidelijk dat er voor de beschrijving van granulaire media nieuwe theoretische methoden nodig zijn. In dit proefschrift wordt hieraan een bijdrage geleverd door middel van een studie naar de krachtenverdelingen in statische granulaire media. Deze krachten organiseren zich in complexe *kracht-netwerken*, zoals te zien is in de experimenten met foto-

elastische schijven – zie Figuur 1.2 in Hoofdstuk 1. Het karakteriseren en begrijpen van deze structuren is het voornaamste doel van ons onderzoek. Daarnaast hopen we middels deze studie naar de 'vaste fase' iets te leren over stromingsgedrag. Bij langzame stromingen zijn de deeltjes nog steeds dicht opeengepakt en spelen kracht-netwerken een belangrijke rol, zoals duidelijk blijkt uit enkele experimenten beschreven in Hoofdstuk 1.

In Hoofdstuk 2 bestuderen we de statistiek van kracht-netwerken met behulp van computersimulaties van granulaire stapelingen. Dergelijke simulaties vormen een belangrijke aanvulling op echte experimenten omdat men in experimenten alleen de krachten *op de bodem* van een stapeling kan meten en niet binnen in het systeem. We tonen aan dat de kansverdeling voor een kracht w op de wand, aangeduid met $\mathcal{P}(w)$, erg gevoelig is voor de lokale geometrie van de stapeling. Hierdoor zal in het algemeen de uitkomst van een meting aan de wand verschillen van de kansverdeling voor een kracht f tussen twee deeltjes in de stapeling, aangeduid met $P(f)$. We laten via een 'geometrische interpretatie' zien hoe de verdelingen $P(f)$ en $\mathcal{P}(w)$ aan elkaar gerelateerd zijn. Met dit inzicht destilleren we vervolgens informatie over het binnenste van de stapeling uit recente experimentele data voor zachte rubber ballen.

De Hoofdstukken 3 en 4 gaan over het zogenaamde q-model. In dit stochastische model, gedefinieerd in Sectie 1.4.4, wordt aangenomen dat de deeltjes op een regelmatige manier gestapeld zijn. Het totale gewicht dat van boven op een deeltje duwt wordt steeds op *willekeurige* wijze verdeeld over de onderlingende deeltjes. In dit modelsysteem is het mogelijk om de statistische verdeling van de gewichten $\mathcal{P}(w)$ exact te berekenen en, net als in de experimenten, blijkt dat de kans op een groot gewicht exponentieel afneemt. In Hoofdstuk 3 onderzoeken we op welke wijze de details van deze statistiek afhangen van *hoe* de gewichten precies over de beneden-buren worden verdeeld. In het bijzonder laten we zien dat de gewichten ongewone correlaties vertonen die afvallen met een machtwet van de afstand tussen de deeltjes.

In de bovenste laag van het q-model zijn alle gewichten aan elkaar gelijk. In Hoofdstuk 4 laten we zien dat de gewichtsfluctuaties op een langzame manier opbouwen als functie van afstand tot deze bovenste laag. Deze langzame relaxatie, veroorzaakt door een diffusie-proces in de correlatie-ruimte, vinden we echter niet terug in de simulaties van meer realistische stapelingen in Hoofdstuk 2. Deze discrepantie geeft aan dat de ruimtelijke propagatie van krachten niet goed door het q-model wordt beschreven.

Hoofdstuk 5 is niet direct gerelateerd aan granulaire media, maar beschrijft een studie naar het zogenaamde 'Asymmetric Random Average Process'. Dit is een model van interacterende deeltjes die bewegen op een één-dimensionale lijn. Meer ingewikkelde versies van dergelijke modellen worden bijvoorbeeld gebruikt bij het beschrijven en voorspellen van verkeersstromingen. Door ons te beperken tot eenvoudige regels voor de bewegingen van de deeltjes is het model analytisch op te lossen, waarbij we gebruik maken van enkele resultaten van het q-model. Zo leiden we de kansverdeling af voor de afstand tussen twee naburige deeltjes en berekenen we de correlaties tussen deze afstanden.

In Hoofdstuk 6 komen we terug op het probleem van kracht-netwerken in granulaire media. We presenteren de eerste resultaten van een nieuw theoretisch idee dat is ontstaan tijdens het schrijven van dit proefschrift. Het uitgangspunt is dat de deeltjes in de meeste gevallen erg hard zijn. Hierdoor kan met een kleine deformatie van de deeltjes een totaal andere kracht bereikt worden. Dit houdt in dat zelfs wanneer alle *posities* van de deeltjes bekend zijn, de *krachten* afhangen van onbekende microscopische details. De aanname die vervolgens gemaakt wordt is dat wanneer all posities van de deeltjes zijn gespecificeerd, *alle mogelijke kracht-netwerken die mechanisch stabiel zijn een even grote waarschijnlijkheid hebben om voor te komen*. Met deze aanname vinden we verbazingwekkend realistische krachtenverdelingen, al voor een klein systeem van 6 ballen in een 'snooker-driehoek' – zie Fig. 6.5. Deze nieuwe aanpak biedt vooral een nieuw theoretisch perspectief op meer complexe problemen van granulaire media en op een recent voorstel van 'jamming' in granulaire media, schuim, glazen etc. In het bijzonder wijzen voorlopige resultaten op een nieuwe interpretatie van het instabiel worden van een te steile zandhelling.

Publications

- J. H. Snoeijer and J. M. J. van Leeuwen, *Force correlations in the q-model for general q-distributions*, Phys. Rev. E **65**, 051306 (2002).

- J. H. Snoeijer and J. M. J. van Leeuwen, *Force relaxation in the q-model for granular media*, J. Stat. Phys. **109**, 449 (2002).

- J. H. Snoeijer, M. van Hecke, E. Somfai and W. van Saarloos, *Force and weight distributions in granular media: Effects of contact geometry*, Phys. Rev. E **67**, 030302 (2003).

- C. B. Holmes, J. H. Snoeijer and Th. Voigtmann, *Dynamic transitions in thermal and athermal systems*, to appear in Proceedings of the 2002 Les Houches Summer School on *Slow Relaxations and Nonequilibrium Dynamics in Condensed Matter*.

- J. H. Snoeijer, M. van Hecke, E. Somfai and W. van Saarloos, *Relation between packing geometry and statistics of force networks in granular media*, submitted to Phys. Rev. E.

- G. Brocks, J. H. Snoeijer, P. J. Kelly, H. J. W. Zandvliet and B. Poelsema, *The difference between Si and Ge(001) surfaces in the initial stages of growth*, submitted to Phys. Rev. B.

- J. H. Snoeijer, T. J. H. Vlugt, M. van Hecke and W. van Saarloos, *Ensemble of force networks: a new approach to (quasi)static granular matter*, in preparation.

Curriculum Vitae

Op 4 juli 1975 ben ik geboren te Kampen. In deze stad heb ik mijn middelbare schooltijd doorgebracht op het Johannes Calvijn Lyceum, tegenwoordig het Ichthus College. Op deze school heb ik in 1993 mijn VWO diploma behaald.

Vervolgens ben ik Technische Natuurkunde gaan studeren aan de Universiteit Twente te Enschede. Halverwege mijn studie heb ik een half jaar gestudeerd aan de Université Pierre et Marie Curie in Parijs in het kader van een Erasmus uitwisselingsprogramma. Voor mijn afstudeeronderzoek heb ik in de groep van Prof. dr. P. J. Kelly gewerkt aan de adsorptie van silicium atomen op het germanium(100) oppervlak. Met een scriptie over dit onderzoek heb ik in 1999 mijn studie afgerond. Verder heb ik in deze periode diverse onderdelen van de Lerarenopleiding gevolgd.

In 2000 ben ik in dienst getreden bij de Stichtig voor Fundamenteel Onderzoek der Materie (FOM) om als promovendus te werken aan de Universiteit Leiden. Onder begeleiding van Prof. dr. ir. W. van Saarloos en dr. M. L. van Hecke deed ik theoretisch onderzoek naar de eigenschappen van granulaire materialen. Tijdens het onderzoek onstond er een intensieve samenwerking met Prof. dr. J. M. J. van Leeuwen, wat zich weerspiegelt in het feit dat hij co-promotor is. De resultaten van het onderzoek zijn verzameld in dit proefschrift.

Tijdens mijn aanstelling heb ik mijn werk gepresenteerd in voordrachten gegeven te Delft, Enschede, Leiden, Lunteren, Nijmegen, Parijs, Les Houches en Peyresq (Frankrijk). Daarnaast heb ik zomerscholen en conferenties bijgewoond in Altenberg, Bayreuth (Duitsland) en Capri (Italië) en bezocht ik diverse instituten in Parijs. Tevens heb ik tijdens mijn promotie werkcolleges verzorgd bij de vakken Statistische Fysica I en Klassieke Mechanica I en II.

Acknowledgements

Stellingen

Behorende bij het proefschrift
"STATISTICS OF FORCE NETWORKS IN GRANULAR MEDIA"
door Jacobus Hendrikus Snoeijer

I. De statistische verdeling van krachten op de wand van een container gevuld met granulaire materie, welke wordt gemeten in experimenten, hangt sterk af van de lokale geometrie van de stapeling en kan significant verschillen van de kansverdeling van de kracht tussen twee deeltjes.

Hoofdstuk 2, dit proefschrift.

II. De aanname dat voor een stapeling van gegeven geometrie en druk alle mechanisch stabiele kracht-netwerken een even grote waarschijnlijkheid hebben om voor te komen, leidt tot een realistische statistiek van de krachten.

Hoofdstuk 6, dit proefschrift.

III. Dat de door het q-model voorspelde langzame algebraïsche relaxatie van de gewichtsfluctuaties niet wordt gevonden in simulaties van meer realistische stapelingen, is een gevolg van de niet-fysische propagatie van de gewichten in dit model.

Hoofdstuk 2 en 4, dit proefschrift.

IV. In het q-model leiden alle q-distributies, behoudens een één-parameter familie, tot stationaire oplossingen waarbij de gewichten correlaties vertonen die afnemen volgens een machtwet van de afstand tussen de gewichten.

Hoofdstuk 3, dit proefschrift.

V. Het is opmerkelijk dat onderzoekers van granulaire materialen al jaren werken met het begrip 'kracht-ketens' (force chains) zonder een wetenschappelijke definitie van dit intuïtieve concept te geven.

VI. Omdat een oplossing van maizena kan worden gesolidificeerd door het te deformeren, bijvoorbeeld door snel te roeren met een lepel, zijn deze colloïdale oplossingen niet te beschrijven met het 'jamming' fase diagram van Liu en Nagel.

A. J. Liu and S. R. Nagel, Nature **396**, *21 (1998).*

VII. Voor een ensemble van positieve x_i waarvoor geldt dat $\sum_{i=1}^{n} x_i = E$, volgt het opmerkelijke resultaat dat het opleggen van extra beperkingen van het type $\sum_{i=1}^{n} \alpha_{ij} x_i = 0$ geen enkele invloed heeft op de verdeling van de x_i wanneer de α_{ij} volgens een Lorentziaanse distributie zijn verdeeld.

VIII. De voor epitaxiale groei van silicium belangrijke 'verdunde dimeer-rijen' hebben op het germanium(100) oppervlak een andere oriëntatie en bindingsenergie dan op het silicium(100) oppervlak.

J. H. Snoeijer, 'Adsorption of Si on thet Ge(100) surface', doctoraalscriptie,
Universiteit Twente.

IX. De introductie van de Grafische Rekenmachine in het voortgezet onderwijs is een schoolvoorbeeld van slecht integratiebeleid.

X. De recidive van de twee supermarktmedewerkers die met geweld een winkeldief aanhielden maakt op pijnlijke wijze duidelijk dat de Nederlandse rechtsstaat geen baat heeft bij individuele acties zoals ondernomen door Prins Bernhard.

Jacobus Hendrikus Snoeijer
Leiden, 4 september 2003.